THESIS FOR THE DEGREE OF DOCTOR OF PHILOSOPHY IN CHEMISTRY

Hydrolytic Synthesis and Physicochemical Properties of TiO_2 Nanoparticles:
Fundamentals and Applications

Jenny Perez Holmberg

UNIVERSITY OF GOTHENBURG

Department of Chemistry and Molecular Biology
University of Gothenburg
Gothenburg, Sweden
2012

Hydrolytic Synthesis and Physicochemical Properties of TiO_2 Nanoparticles:
Fundamentals and Applications

Department of Chemistry and Molecular Biology
University of Gothenburg
412 96 Göteborg
Sweden

ISBN 978-91-628-8421-5
E-publication: http://hdl.handle.net/2077/28255

Printed by Chalmers Reproservice

Cover illustration:
Round-bottom reaction flask containing (clockwise from top): oscillatory patterns in measured intensity from dynamic light scattering; binary-sphere model of TiO_2 nanoparticle and aggregate; x-ray diffraction pattern of anatase/brookite TiO_2; a positively-charged hydroxylated oxide surface.

I take this journey with you, so that we may find greatness in the smallest of things.

Abstract

Titanium dioxide (TiO_2) nanoparticles were synthesized via the hydrolysis of $TiCl_4$ in order to produce clean, surfactant-free oxide surfaces. By controlling the synthesis and aging conditions, stable particles with well-defined size distributions were obtained. The particles were characterized using dynamic light scattering (DLS), electrospray-scanning mobility particle sizer (ES-SMPS), transmission electron microscopy (TEM), and X-ray diffraction (XRD) in order to gain information about the size, morphology and crystalline structure of the material. Dialysis and storage of the particles at 0°C, 5°C and room temperature gave rise to average particle sizes of around 8, 10, and 18 nm after the first 3 weeks of aging. The sizes obtained from DLS and ES-SMPS were generally in good agreement. Analysis by TEM and XRD shows that the synthesis products are composed of primary particles, about 4 nm in size, predominantly of anatase structure. A small amount of brookite (<10%) is produced. Thermodynamic calculations and experimental data reveal that the formation of the oxide particle proceeds from the condensation of titanium complexes, the first hydrolysis products, from solution. At low pH, a repeated condensation/dissolution process occurs, until an amorphous Ti-oxyhydroxide is formed, which eventually becomes crystalline TiO_2.

Experimental results from ES-SMPS and DLS indicate that the particles grow to their average measured size by the formation of stable aggregates. The effects of polydispersity on the collective diffusion detected by DLS were examined in detail, and a binary sphere model was proposed, to explain the nonlinear concentration dependence of the diffusion coefficient. The interactions between small particles and larger porous aggregates give rise to nonlinearity in transport behaviour at low volume fractions. A closer look at the surface charging of the particles was done by theoretical calculations and experiments, with indications of size-dependent behaviour.

The influence of the TiO_2 nanoparticle properties on selected applications was illustrated, using the characteristics of the porous nanoparticle surface on Ti dental implants and the interactions of free TiO_2 nanoparticles with Ca^{2+}-rich lipid bilayers. The findings of these studies validate that the direct exposure of the oxide surface to the surrounding electrolyte is significant in terms of understanding interfacial processes from the biological perspective.

Keywords: *Titanium dioxide, nanoparticles, synthesis, hydrolysis, $TiCl_4$, anatase, brookite, DLS, ES-SMPS, XRD, collective diffusion, interfacial processes.*

List of Publications

This thesis is based on the work presented in the following papers. The papers will be referred to by their Roman numerals in the text.

I. Synthesis, characterization and particle size distribution of TiO_2 colloidal nanoparticles
Z. Abbas, J. Perez Holmberg, A.-K. Hellström, M. Hagström, J. Bergenholtz, M. Hassellöv, E. Ahlberg
Colloids and Surfaces A: Physicochem. Eng. Aspects, **2011**, 384, 254-261

II. Nonlinear Concentration Dependence of the Collective Diffusion Coefficient of TiO_2 Nanoparticle Dispersions
J. Perez Holmberg, Z. Abbas, E. Ahlberg, M. Hassellöv, J. Bergenholtz
J. Phys. Chem. C, **2011**, 115, 13609-13616

III. Near room temperature synthesis of monodisperse TiO2 nanoparticles – Growth mechanism
J. Perez Holmberg, A.-C. Johnsson, J. Bergenholtz, Z. Abbas, E. Ahlberg
Submitted 2012-04

IV. Surface Charge and Interfacial Potential of TiO_2 Nanoparticles: Theoretical and Experimental Investigations
J. Perez Holmberg, E. Ahlberg, J. Bergenholtz, M. Hassellöv, Z. Abbas
Manuscript

V. Electronic properties of TiO_2 nanoparticle films and the effect on bioactivity
J. Löberg, J. Perez Holmberg, I. Mattisson, A. Arvidsson, E. Ahlberg
Manuscript

VI. TiO_2 nanoparticle induced damage in lipid membranes
F. Zhao, J. Perez Holmberg, R. Frost, Z. Abbas, B. Kasemo, M. Hassellöv, S. Svedhem
Submitted 2012-03

Statement of Contribution

This list provides the details of the contributions by J. Perez Holmberg to each of the publications.

I. Made developments on the experimental design; performed almost all the experimental work; collaborated with Dr. S. Gustafsson on the TEM imaging; major contributor to the data evaluation and writing.

II. Designed the experiments with Dr. J. Bergenholtz; performed all the experimental work; ran calculations on the binary-sphere model using pre-programmed code by Dr. J Bergenholtz; major contributor to the data evaluation and writing; lead author with support from co-authors.

III. Designed the experiments with Prof. E. Ahlberg and Dr. A.-C. Johnsson; performed the experimental work in collaboration with Dr. A.-C. Johnsson; major contributor to the data evaluation and writing; lead author with support from co-authors.

IV. Performed the light scattering experiments; participation in the data evaluation and discussion; lead author with major support from co-authors.

V. Provided the TiO_2 nanoparticles used in the experiments; performed size measurements using dynamic light scattering; participation in the data evaluation.

VI. Provided the TiO_2 nanoparticles used in the experiments; contributed to writing the experimental part of the article.

Table of contents

Abstract v

Chapter 1: Introduction 1

Chapter 2: Survey of Methods 3
2.1 Dynamic Light Scattering 3
2.1.1 Light scattering, diffusion, and hydrodynamic size 3
2.1.2 Laser Doppler Velocimetry, electrophoretic mobility, and zeta potential 5
2.2 Electrospray – Scanning Mobility Particle Sizer 7
2.2.1 Electrospray: the transfer from liquid to gaseous suspension medium 7
2.2.2 Differential mobility analyzer: aerodynamic size differentiation 8
2.2.3 Condensation Particle Counter: number-based size distribution 10
2.3 X-ray Diffraction 11
2.4 Transmission electron microscopy 14

Chapter 3: Synthesis and Characterization of TiO_2 15
3.1 Synthesis of TiO_2 from $TiCl_4$ 15
3.1.1 Examples from literature 15
3.1.2 TiO_2 nanoparticles from the controlled hydrolysis of $TiCl_4$ 16
3.2 Characterization of TiO_2 nanoparticles 18
3.2.1 Crystalline structure 18
3.2.2 Particle size determination 21
3.2.2.1 The Scherrer crystallite size 21
3.2.2.2 Transmission electron microscopy 22
3.2.2.3 Dynamic light scattering 22
3.2.2.4 Electrospray-Scanning Mobility Particle Sizer 23
3.3.4 Comparison between sizing methods 24
3.4 Commentary on TiO_2 synthesis and characterization 25

Chapter 4: TiO_2 Nanoparticles from Hydrolysis 27
4.1 Hydrolysis of $TiCl_4$ 27
4.1.1 Hydrolysis in the precursor solution 27
4.1.2 Complexation and precipitation during dialysis 28
4.2 Experimental results 30
4.2.1 Measurements with ES-SMPS 30
4.2.2 Measurements with DLS 32
4.3 Formation of TiO_2 34
4.4 Commentary on experimental design 35

Chapter 5: The Diffusion of Polydisperse TiO_2 Suspensions 37
5.1 Dynamic Light Scattering and the Diffusion Coefficient 37
5.1.1 Scattering Theory 38
5.1.2 Experiments on TiO_2: multi-angle light scattering 40
5.2 The occurrence of nonlinear behaviour in colloidal systems 42
5.3 Binary Sphere model 43
5.4 Implications of the findings 47

Chapter 6: Surface Charge and Interfacial Potential 49
6.1 Surface charge on TiO_2 49
6.1.1 Surface complexation in aqueous medium 49
6.1.2 Zeta potential 50
6.2 Corrected Debye-Hückel Theory of Surface Complexation 51
6.3 Surface charging on anatase nanoparticles based on theory 52
6.4 Interfacial potential from light scattering experiments 53

Chapter 7: Applications and Implications 55
7.1 Surface interactions: electronic properties of TiO_2 nanoparticle films 55
7.1.1 Surface characterization 55
7.1.2 Electrochemical characterization 57
7.1.2.1 Cyclic voltammetry 58
7.1.2.2 Electrochemical Impedance Spectroscopy 60
7.1.3 Simulated body fluid (SBF) tests 61
7.1.3 Commentary on nanoparticle film structure and dental implant applications 62
7.2. Free particle effects: TiO_2 nanoparticles and lipid membranes 63

Chapter 8: Conclusions and Outlook 67
8.1 Conclusions 67
8.2 Outlook 68

Acknowledgements 70

References 72

List of Abbreviations

AFM	Atomic force microscopy
CDH-SC	Corrected Debye-Hückel theory of surface complexation
CPC	Condensation particle counter
DLS	Dynamic light scattering
DMA	Differential mobility analyzer
DOS	Density of states
EDX	Energy-dispersive x-ray spectroscopy
EIS	Electrochemical impedance spectroscopy
ELS	Electrophoretic light scattering
ES-SMPS	Electrospray-Scanning mobility particle sizer
LDV	Laser Doppler velocimetry
POEPC	1-palmitoyl-2-oleoyl-sn-glycero-3-ethylphosphocholine
POPC	1-palmitoyl-2-oleoyl-sn-glycero-3-phosphocholine
POPG	1-palmitoyl-2-oleoyl-sn-glycero-3-phospho-(1'-rac-glycerol)
QCM-D	Quartz crystal microbalance with dissipation monitoring
QELS	Quasi-elastic light scattering
SBF	Simulated body fluid
SEM	Scanning electron microscopy
TiO_2	Titanium dioxide
$TiCl_4$	Titanium tetrachloride
TRIS	tris(hydroxymethyl)aminomethane
XRD	X-ray diffraction

Short list of symbols

Below is a list of symbols that are used in different contexts, depending on the chapter.

D	diffusion coefficient (DLS), Chap. 2, 5 particle diameter (CDH-SC), Chap. 6 dissipation factor (QCM-D), Chap. 7
d	separation distance between crystal planes (XRD), Chap. 2 counter ion size (CDH-SC), Chap. 6
E	magnitude of the electric field (LDV), Chap. 2 voltage (EIS), Chap. 7
f	friction coefficient (DLS), Chap. 2 resonant frequency (QCM-D), Chap. 7
q	magnitude of the scattering vector (DLS, LDV) Chap. 2,5 particle charge (ES-SMPS) Chap. 2
κ	Debye decay parameter (DLS, CDH-SC), Chap. 2, 5, 6 electrical conductivity (ES-SMPS), Chap. 2, 4
θ	scattering angle (DLS), Chap. 2, 3, 5 Bragg angle (XRD), Chap. 2, 3

Chapter 1: Introduction

In which we are introduced to TiO_2 and we explore the purpose of this research work

When William Gregor examined the black mineral ilmenite in the sands of the river Helford in 1791,[1] he was not aware of the far-reaching impacts of his discovery. Over the next centuries, that mineral became a source of materials used in objects as diverse as flying machines, artificial implants, works of art, and self-cleaning surfaces. If the good vicar was a golfer, he would indeed be pleased to know that the metal extracted from this ore would eventually be used in golf clubs just more than a century later.

The removal of iron and other impurities from ilmenite ($FeTiO_3$) resulted in the tensile, lightweight metal Titanium, named after the Titans in Greek mythology. The metal proved worthy of its name, as Ti alloys find valuable uses in the transport and medical industry. Furthermore, ilmenite is a natural source of titanium dioxide (TiO_2), also called titania. The high refractive index of TiO_2 accounts for its ubiquity as a white pigment found in paint, plastic, paper and food.[2] The optical properties of TiO_2, in conjunction with its electrical properties as a semiconductor, have broadened the possibilities for its use, especially in recent years. Of particular interest are the enhanced properties of TiO_2 as the size of the material decreases and enters the colloidal domain.

Titanium dioxide nanoparticles are employed in a wide range of applications. Important application areas include photocatalysis,[3, 4] water purification,[5] solar energy conversion,[6] sensors,[7] and optoelectronics.[8] The capability to utilize TiO_2 for these purposes arises from the enhanced reactivity of nanoparticulate TiO_2 compared to that of the bulk material. In the specific case of photocatalysis, the photocatalytic activity of TiO_2 has been reported to depend on the size of the particles.[9] Surface charging theory has shown that a considerable increase in surface charge density occurs when particles reach sub-10 nm sizes.[10] The changes in the optical and electronic properties are due to both quantum size effects and the progressively important role of the surface in controlling the overall energy of the particles.[11, 12] Given that the number of atoms at the surface increases with decreasing particle size, it is reasonable to expect that surface reactions are reinforced and become more significant. It follows that particle morphology and surface defects influence the type and extent of processes that occur on the nanoparticle surface. Compared to large particles and flat surfaces, nanoparticles can have under-coordinated corner defects. Such features affect how ligands bind to the surface and give rise to size-dependent coordination states of surface Ti atoms.[13, 14] The presence of dopants and impurities on the nanoparticle surface bring about effects on the electrical conductivity of the material.[15]

Surface impurities on TiO_2 nanoparticles often occur as a result of the synthetic process, and organic species on the TiO_2 surface are acquired from various sources. The use of titanium alkoxides as synthesis precursors,[16-20] as well as the use of acetic acid,[17] alcohol,[21] oils,[22] and other organic solvents[16, 21] as reaction media are examples of such sources. Post-synthetic steric stabilisation of nanoparticles through the use of ionic surfactants, such as sodium dodecyl sulphate,[23] also introduce extraneous material which may interfere with the accurate observation of the processes occurring at the oxide-water interface. In the interest of studying

interfacial phenomena on TiO_2 nanoparticles, a surfactant-free hydrolytic synthesis proves to be advantageous.

This research project investigates the physicochemical properties of TiO_2 nanoparticles produced by hydrolytic synthesis. The synthesis protocol has been developed towards the production of TiO_2 of well-defined particle sizes for the purpose of studying the size dependence of surface properties. Extensive characterization of the synthesis product was conducted in order to determine size, morphology and crystalline structure. These material characteristics are related to the behaviour and stability of TiO_2 colloidal suspensions, and can be used to explain certain interfacial phenomena, such as surface charging. A detailed view of two sizing methods, dynamic light scattering (DLS) and electrospray-scanning mobility particle sizing (ES-SMPS), is also presented in order to better understand the kind of information that is obtained from these techniques. Lastly, the implications of the physicochemical properties of TiO_2 nanoparticles are explored from an applications perspective. The electronic properties of TiO_2 nanoparticle films on Ti-implant surfaces and the interaction of TiO_2 nanoparticles with lipid membranes are presented as examples.

The fundamental knowledge gained from these investigations contributes significantly to the understanding of nanometer-sized colloidal TiO_2. Size-dependent properties are key factors to consider in materials design. Surface charging and other interfacial phenomena can be used to explain certain aspects of TiO_2 reactivity from the environmental and physiological perspective. The synthesis and characterization protocols are also of interest from the methods development perspective and can prove to be useful even in the study of other oxides and nanomaterials.

This written work commences with a presentation of the main characterization techniques used in the research, in order to give the reader a basic idea of the capabilities and limitations of the methods. Then the following chapters will each be focused on discussing the key aspects and results in the publications and manuscripts that have been written during the course of this project. Finally, the conclusions based on the findings are enumerated and recommendations for future research work are presented.

Chapter 2: Survey of Methods

In which the tools that are used to characterise TiO_2 nanoparticles are presented

A poem from the 19th century tells of an old Indian tale about three blind men from Hindustan who encounter an elephant for the first time[24]. The elephant proved to be an enigma for the men, who each took their turn in describing the massive creature, based on the specific part that they touched. This led to a vivid argument among the men, but as it turned out, they were all partly in the right. In order to fully understand the features of the elephant, it is necessary for the men to combine their limited perspective, in order to achieve a more complete image of the creature.

The measurement scales may be different, but the same principle is applied in the characterization of nanomaterials. For this project, a number of methods were employed in the analysis of synthesized TiO_2 nanoparticles. They were selected in order to obtain information on the size, morphology and crystalline structure of the particles.

2.1 Dynamic Light Scattering

Dynamic light scattering (DLS) makes use of spectral analysis in order to observe dynamical properties which characterize colloidal dispersions of particles. It is a commonly used technique for the determination of particle size in the sub-micron range. An intensity-based hydrodynamic size is calculated from a measured collective diffusion coefficient.

2.1.1 Light scattering, diffusion, and hydrodynamic size

When light, an oscillating electromagnetic field, interacts with matter, the result is the scattering of secondary electromagnetic radiation in all directions. The scattering of light is detectable when the system in focus is inhomogeneous. Particles in colloidal suspension scatter light due to the difference between the refractive index of the particle material and that of the surrounding solvent. Upon contact with the particles, the irradiated light becomes phase-shifted. This is due to the distance between particles, which cause the light waves to travel different path lengths to the detector placed at an angle θ. Figure 1 schematically shows the typical components for dynamic light scattering (DLS) measurements for a scattering angle of 90°. The type of scattering that is considered in DLS is elastic scattering; only the phase shift of scattered light is taken into account, and any absorption by the particles is neglected. Hence, the method is termed as quasi-elastic light scattering (QELS).[25]

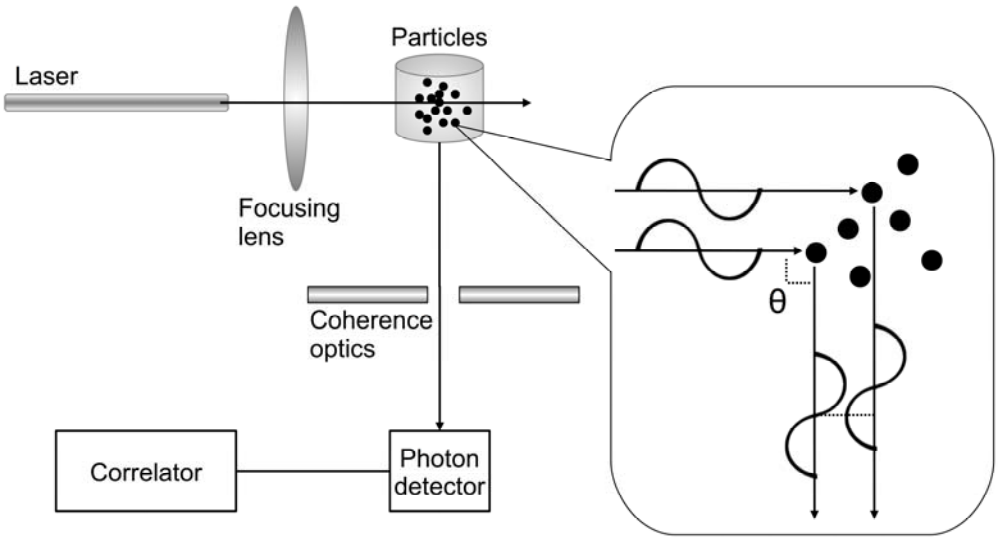

Figure 1. Overview of typical instrumental components in dynamic light scattering for a scattering angle, θ = 90°. The inset demonstrates how the light becomes phase-shifted due to contact with the suspended particles (*figure based on reference* [26]).

The phase shift brings about constructive and destructive interferences, the extent of which is dependent on the relative positions of the particles, which change due to Brownian motion and diffusion. Continuous collisions with solvent molecules impart momentum to the particles and bring about random patterns of displacement[27]. Aside from this Brownian motion, the particles are also subject to translational diffusion. Consequently, a time-dependent fluctuation of light intensity is observed. The temporal variations in the intensity of scattered light are represented using an intensity autocorrelation function (IACF), defined as:

$$g^{(2)}(t) = \frac{\langle I(0)\, I(t)\rangle}{\langle I(0)\rangle^2} \qquad [1]$$

where the brackets denote an average over time. For longer time periods, at which the particles have diffused such that their positions no longer depend on the original position at $t = 0$, the intensities are totally uncorrelated and $g^{(2)}(t)$ is approximately equal to 1.

For real polydisperse systems, the Brownian motion is characterized by a distribution of diffusion coefficients. The z-average diffusion coefficient can be extracted from a cumulant analysis of $g^{(2)}(t)$, defined in this case as

$$g^{(2)}(t) \approx 1 + e^{2\left(-\Gamma t + \frac{\mu_2 t^2}{2} + \frac{\mu_3 t^3}{6} + \ldots\right)} \qquad [2]$$

where Γ is the first cumulant and μ_i are higher-order cumulants.[28, 29] The first cumulant $\Gamma = q^2 D_z$ is also known as the decay rate of the intensity autocorrelation function, containing the z-average diffusion coefficient D_z, and the magnitude of the scattering vector, q. The width of the size distribution can be estimated as μ_2/Γ^2 and can be regarded as a measure of

the degree of polydispersity.[30] For spherical particles, a simplification of the IACF is assumed to be:

$$g^{(2)}(t) \approx 1 + e^{-2q^2Dt} \qquad [3]$$

where the collective diffusion coefficient D is related to a hydrodynamic radius, r_H by the Stokes-Einstein formula:

$$D = \frac{k_B T}{6\pi\eta r_H} = \frac{k_B T}{f} \qquad [4]$$

where k_B is the Boltzmann constant, T is the absolute temperature of the suspension, and η is the viscosity of the solvent. The denominator in this expression is collectively taken as the friction coefficient, f. [27]

As the decay rate Γ is inversely proportional to the particle size, it follows that there are different decay rates which are, correspondingly, inversely proportional to the different particle sizes described in the IACF. Thus, the IACF can be re-written as a distribution of relaxation rates

$$g^{(2)}(t) \approx 1 + \left(\int_0^\infty G(\Gamma) e^{-\Gamma t} d\Gamma \right)^2 \qquad [5]$$

which can be used to construct an intensity-based particle size distribution, using inverse Laplace techniques. Various algorithms can be used to fit an intensity-based size distribution to this transformed data, among them are the non-negatively constrained least-squares methods (NNLS)[25] and the CONTIN algorithm, which is a regularization method developed by Provencher.[31] The default algorithm used in the Malvern instrumentation for fairly monodisperse suspensions is based on NNLS. For polydispersities of at least 20% of the average size, the CONTIN algorithm is recommended.

2.1.2 Laser Doppler Velocimetry, electrophoretic mobility, and zeta potential

A charged particle in suspension, when subjected to an external electric field, migrates towards the pole of opposite polarity at a characteristic drift velocity, v_d. This rate is proportional to the magnitude of the electric field, E, such that

$$v_d = \mu E \qquad [6]$$

where the constant of proportionality, μ, is the electrophoretic mobility[32]. Laser Doppler velocimetry (LDV) is a spectroscopic technique used to study the electrophoretic mobility and diffusional properties of colloidal particles by the analysis of quasi-elastically scattered light. It is also known as electrophoretic light scattering (ELS). This method measures the instantaneous velocity of particles as a Doppler shift in the spectrum of scattered light.[33] Optical heterodyne detection is applied to electrophoretic light scattering in order to

incorporate this frequency shift under an applied electric field.[34] Considering only translational diffusion, the second-order correlation function is defined under electrophoretic conditions as:[33, 35]

$$g^2_{(K,\tau)} = NE_s^2 \exp(-i\omega_0\tau)\exp(-iqv_D\tau)\exp(-D^t q^2\tau) \qquad [7]$$

In the above equation, N represents the number of independent spherical scatterers in the scattering volume, E_s is the amplitude factor of the scattered electric field, and D^t is the translational diffusion coefficient. The parameter $q = 4\pi(n/\lambda_0)\sin(\theta/2)$ is the magnitude of the scattering vector, which includes the refractive index of the solution (n), the wavelength of incident radiation (λ_0), and the scattering angle (θ). The drift velocity in this case is the Doppler velocity, v_D, while ω_o and ω are the incident and shifted frequencies, respectively. The Doppler shift in frequency, $\Delta\omega$, is related to the electrophoretic mobility, μ, by the equation[33]

$$\Delta\omega = qv_d = \mu E_s q \qquad [8]$$

Electrophoretic mobility is proportional to the zeta potential, ζ, which is the electrical potential at the surface of shear, located at some distance from the surface of the charged particle. The surface of shear corresponds to the layer of liquid which moves at the same velocity with the particle. The general expression for zeta potential is Henry's equation[27, 36]

$$\mu = \frac{2}{3}\frac{\varepsilon_r\varepsilon_0\zeta}{\eta}f(\kappa a) \qquad [9]$$

where ε_r and ε_0 are, respectively, the relative and vacuum permittivity and η is the viscosity of the solvent. The value of $f(\kappa a)$ derives from Henry's function, which incorporates the Debye length $(1/\kappa)$ and the particle radius (a). The Debye length, which denotes the scale at which particle charge screening occurs, depends on the ionic solution. Thus, zeta potential can vary, depending on the electrolyte environment. These factors are presented in detail in Chapter 6, which discusses nanoparticle surface charging.

Essentially the same instrumentation is used in electrophoretic light scattering as with DLS, but with some modifications. The sample cell in this case has two parallel plate electrodes between which the electric field is passed. Aside from the main laser beam, a second laser beam, called the reference beam, is used. This reference beam is not Doppler shifted and the scattered light is compared with this light source. This approach is an example of heterodyne detection of light, which is used for very small frequency shifts.[37] In order to achieve spectral resolution for this type of detection, small scattering angles are optimal. The electrophoretic mobility measurements conducted on the instrument used in this study (Malvern Zetasizer Nano ZS) detects μ at a scattering angle, $\theta = 12.8^\circ$.

2.2 Electrospray – Scanning Mobility Particle Sizer

As dynamic light scattering produces a size measurement that is heavily dependent on the hydrodynamic behaviour of particles, a complementary technique proves to be beneficial in order to have a more complete understanding of nanoparticle suspensions. Measurements using an electrospray coupled to a scanning mobility particle sizer (ES-SMPS) provide particle size distributions based on the electrodynamic mobility of particles suspended in the gas phase, and hence are not influenced to the same extent by solvent effects. The process involves the transfer of particles from the liquid to a gas phase by an electrospray apparatus, particle sizing in a differential mobility analyser (DMA), and the determination of the amount of particles using a condensation particle counter (CPC). The information obtained from the different sized fractions is used to construct a number-based size distribution, from which a number-average particle size is derived. The different components of the instrumental technique are presented in Figure 2.

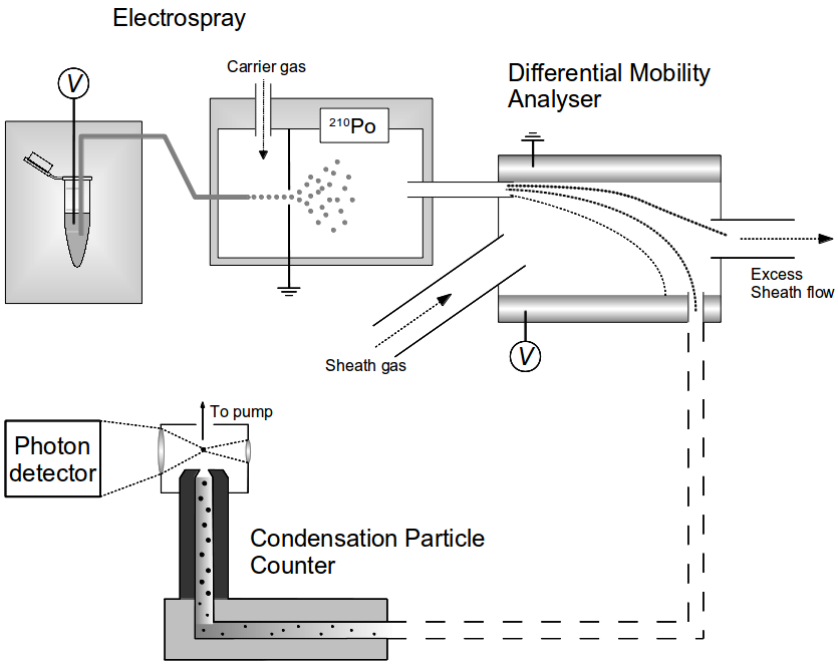

Figure 2. Simplified schematic diagram of the electrospray-scanning mobility particle sizer (ES-SMPS) used for this study. The ionization chamber of the electrospray apparatus uses ^{210}Po to neutralise excess charge built up from the spraying of sample solutions. The SMPS is comprised of a differential mobility analyser that separates particles according to their electrodynamic mobility, and a condensation particle sizer which individually counts the particles in each size fraction. *(This figure is based on references [38-40].)*

2.2.1 Electrospray: the transfer from liquid to gaseous suspension medium

The electrospray device atomizes a liquid into ultrafine aerosol droplets by the application of a potential difference between a plate and the end of the liquid-containing capillary tube. When charged with several kilovolts, the meniscus of a conducting solution forms a cone that is extended at its apex by a jet.[41] This cone-jet structure is commonly referred to as the Taylor cone.[42] The form of the cone-jet is influenced by the viscosity, resistivity, and flow rate of the liquid. In turn, the flow rate depends on the pressure inside and at the end of the capillary, as well as on the electrostatic pressure produced by the applied voltage.[43] Solutions of high

conductivities and low flow rates form jets that disintegrate into droplets that are small enough to each contain one particle.[41] This implies two prerequisites for an effective sizing of particles: a) that a monodisperse droplet size is optimised for the system being studied; and b) that the sample concentration is low enough to be able to count individual particles but sufficient to obtain the needed statistics for a reliable particle size distribution. The initial diameter, D_d, of droplets produced from a polar liquid is described as

$$D_d = G\left(\frac{Q\varepsilon\varepsilon_0}{\kappa}\right)^{1/3} \qquad [10]$$

where Q is the flow rate through the jet, ε is the electrical permittivity of the liquid, ε_o is the electrical permittivity through vacuum, κ is the electrical conductivity, and G is a factor that is influenced by viscosity.[41, 44, 45]

The droplets produced from the cone-jet often have a high positive charge. Partial neutralisation of charge is deemed necessary for a number of reasons. A high electrical charge corresponds to high electrical mobility, which can lead to deposition on the walls of the instrument and a reduced aerosol/particle throughput[41]. Furthermore, neutralisation makes it possible to produce stable, fine droplets upon evaporation[46]. In a highly charged evaporating aerosol, the repulsive electrostatic force can overcome the attractive surface tension force, leading to its rupture and the offshoot of daughter droplets, a phenomenon known as Rayleigh disintegration[47]. The electrospray instrument used for this study is equipped with a ^{210}Po-bipolar charger which ionises gas molecules in the spray chamber, with a charge opposite to that of the sprayed aerosols. Partial neutralisation is achieved via charge exchange, keeping the charge on the droplets below the Rayleigh limit.[39]

2.2.2 Differential mobility analyzer: aerodynamic size differentiation

After the suspension of particles is sprayed into individual aerosols, they are transported from the electrospray apparatus to the scanning mobility particle sizer (SMPS), which is made up of two main instrumental components: a) an electrostatic classifier containing a differential mobility analyzer (DMA); and, b) a condensation particle counter (CPC).

As the charged particles enter the electrostatic classifier, they are introduced into a stream of clean gas and move at a speed that is proportional to the applied electrical field such that $u = ZE$, where u is the average velocity of the particles, E is the electric field, and Z is the electrical mobility, defined by the formula below.

$$Z = 0.441\frac{q(kT/m)^{1/2}}{pd_p^{\,2}} \qquad [11]$$

This expression is valid for a sphere with a charge, q and diameter, d_p. For spherical particles, the electrical mobility diameter (d_m) is equal to the physical or geometric diameter (d_p)[48]. The parameters p, T and m are the pressure, absolute temperature, and molecular mass of the carrier gas, respectively. In this equation, k is the Boltzmann's constant[49].

A clean gas flow, containing polydisperse charged particles, enters the DMA (shown in Fig. 2). The analyzing region of the DMA housing of the DMA contains a high voltage center rod. The electrical field in the analyzing region attracts particles from the outer wall, causing them to drift in the direction of the center rod, while an axial air flow carries particles downward. The trajectories of the particle flow depend on the electrical mobility, *Z*. Particles with high Z deposit on the center rod upstream of the sampling slit, while those with low mobility are carried out with the main outlet flow.[49, 50] Recent design modifications on the DMA have made the device capable of size differentiating particles down to 3 nm in diameter. Aerosol losses due to Brownian diffusion have also been reduced by shortening the annular aerosol passage and maintaining a laminar and steady flow at the entrance slit.[51]

There is a narrow range of electrical mobility in which the flow trajectories allow a fraction of the injected aerosols to reach the sampling slit and be carried away with the sampling flow. This range can be altered by adjusting the operating conditions of the DMA. In order to circumvent the simultaneous transmission of particles having different mobilities through the DMA, the strength of the electric field is varied during the course of measurement. This variation is done according to the equation[52]

$$E_1(t_m) = \{V_0/r_1 \ln(r_1/r_2)\} \exp(\pm t_m/\tau) \qquad [12]$$

where $E_1(t_m)$ is the strength of the electric field at time t_m, τ is the time constant, V_o is the initial counter rod voltage, and r_1 and r_2 are the radii of the center rod and the outer cylinder, respectively. In effect, the DMA scans through a range of mobilities over time.

The probablility that particles of a certain mobility Z_p would enter the sampling flow is given by the transfer function, Ω, algebraically expressed as

$$\Omega = \left(\frac{1}{q_a}\right) \cdot \max\left\{0, \min\left(q_a, q_s, \left[1/2\left(q_a + q_s\right) - \left|2\pi Z_p \cdot \Delta\Phi + 1/2\left(q_m + q_c\right)\right|\right]\right)\right\} \qquad [13]$$

where q_a, q_c, q_s, and q_m are the aerosol, clean air, sampling, and main outlet flow rates, respectively. $\Delta\Phi$ denotes the change in the electric flux function, the value of which can be determined by integrating along a path from the entrance to the exit slits.[50] The transfer function thus defines the mobility window that is created by the scanning DMA. Assuming ideal DMA behaviour, the transfer function is expected to be of a triangular shape,[50] while for ultrafine particles ($d_p \leq 20$ nm), a bell-shaped transfer function may be obtained.[53] The real shape of the transfer function depends on the instrumental design, applied voltages, and actual flow rates in the DMA; it is influenced greatly by particle losses and trajectories.[54, 55] This shape provides important systematic information, as the area of the transfer function can be taken as a measure of diffusional loss inside the DMA.[56] Additionally, the DMA mobility resolution is defined as: $R = Z^*/\Delta Z_{fwhm}$, where Z* is the mobility at the peak of the transfer function and ΔZ_{fwhm} is the full width at half-maximum.

Deviations of the transfer function from the ideal are said to be consequences of Brownian diffusion. Particle losses in the connector tubing and inlets of the DMA decrease the area of

the transfer function. The broadening of particle trajectories inside the analyzer column brings about a corresponding increase in the width of the transfer function.[53, 55] Diffusional losses are size-dependent and can cause differences in the calculated size distributions. Therefore, the assumption of an idealized, size-independent transfer function leads to an underestimation of particle number concentrations in the ultrafine size range. Polydisperse particle size distribution measurements by DMA involve scanning a mobility distribution much wider than the transfer function of the DMA. In this case, the mobility distribution can be calculated from the ratio of the particle number concentration measured downstream of the DMA divided by the area of the transfer function. The actual particle size distribution can then be determined from measured mobility distributions using an inversion algorithm.[54]

2.2.3 Condensation Particle Counter: number-based size distribution

The condensation particle counter (CPC) is an instrument which measures the number concentration of submicron airborne particles. Consequently, the number-based size distribution of submicron aerosols can be determined by this device, when used in conjunction with a differential mobility analyser. The apparatus has the following main components: an alcohol saturator, a condenser, focusing optics, and collecting optics. The size-differentiated aerosols flow from the DMA into the saturator, which is an inclined tube containing a felt lining that is partially dipped into a butanol reservoir. The butanol-saturated aerosol then enters the condenser tube; butanol condenses on the aerosol particles, causing them to grow into a droplet size (about 10 μm) large enough to be detected by light scattering photometrics. The focusing optics provide the beam of light that is irradiated upon the condensed droplets while the collecting optics collect the light scattered at a 90° angle. This scattered light from individual droplets is converted by a photodetector into voltage pulses; each pulse is taken as representative of individual seed particles. This is referred to as the counting mode of the CPC, where the particle concentration is computed from the number of pulses counted per second and the aerosol sample flow rate.[38, 40] Statistical accuracy in the counting mode is achieved by ensuring that the particles are sampled over a sufficiently long averaging time, as well as considering the particle concentration in the sample. When particle concentration is greater than 1000 particles/cm^3, more than one particle can be simultaneously present in the viewing volume; particles can no longer be counted individually.[38]

Since the sampled aerosols enter the CPC subsequently from the DMA, the CPC-measured size distribution is dependent on the DMA transfer function, the distribution of unipolar charged particles at the DMA inlet, and the DMA transport efficiency. Due to the broadening of the transfer function for ultrafine particles, correspondingly large uncertainties in the counting efficiency can occur.[57] Diffusional and inertial losses are less significant in the CPC compared to the DMA. However, detection losses can result from insufficient droplet growth to allow optical detection. This occurs at high aerosol concentrations, where vapour depletion and latent heat release impede the droplet growth.[58]

A number of factors are incorporated into the CPC counting efficiency,[58] defined for a specific particle size as

$$\eta_{cpc}(d_p) = \eta_{sam}(d_p) \cdot \eta_{act}(d_p) \cdot \eta_{\det}(d_p) \qquad [14]$$

The factors contained in the overall CPC counting efficiency refer to the contributions of the sampling, activation, and detection efficiencies, respectively. The sampling efficiency comes from the ratio of two particle concentrations: the concentration exiting the sample capillary and that extracted from the transport flow. Activation efficiency refers to the fraction of particles exiting the sample capillary that are activated in the condenser, while detection efficiency is the fraction of activated particles that grow into droplets that are successfully detected[58]. Activation efficiency can be shifted to smaller sizes by increasing the temperature difference between the saturator and the condenser. The resulting higher supersaturation inside the condenser causes smaller aerosol particles to become activated. Combined activation and detection losses place the average 50% detection efficiency diameter of a typical ultrafine cpc (TSI-3025) at 2.42 nm. At sizes below 5 nm, the counting efficiency is influenced by disturbances of the laminar flow in the condenser tube and is dependent on the chemistry of the particle-working fluid system, as well as the particle charge states.[57-59]

2.3 X-ray Diffraction

The crystalline structure of an oxide is vital information that can be used to predict and understand other physicochemical properties. The arrangement of unit cells, defects and impurities in the structure have significant consequences on the material's activity, especially in the case of nanoparticles, where a significant proportion of atoms are located on the surface. Optical properties, such as colour, band gap and photoconductivity for example, depend greatly on crystallite size and nanostructure.

X-ray diffraction (XRD) is a spectroscopic method which has been used in the fingerprint characterization and structure determination of crystalline materials. A collimated beam of x-rays is irradiated upon the crystal, and the angles at which the beam is diffracted are measured.[60] Crystals have regularly repeating features that make them capable of diffracting radiation that has a wavelength in the range of interatomic separations, which are around 2-3 Å. The most commonly used wavelength in XRD experiments is the Cu *K*α radiation, with λ = 1.5418 Å.[61] The scan is made through a broad range of angles; each detected x-ray signal corresponding to a coherent reflection from successive planes of the crystal is recorded. An x-ray diffraction pattern, containing the diffraction angles with the corresponding signal intensities, is obtained. The diffraction pattern is specific for a particular structure and can hence be used to identify materials with high accuracy.

One approach to the analysis of x-ray diffraction is to assume that crystals are built up in planes that act as semi-transparent mirrors; some of the incident x-rays are reflected back, while the rest are transmitted and subsequently reflected by succeeding planes. There are specific conditions under which the reflected beams are coherent. Figure 3 shows the diffraction paths at two adjacent crystal planes, separated by a perpendicular distance, *d*.[61]

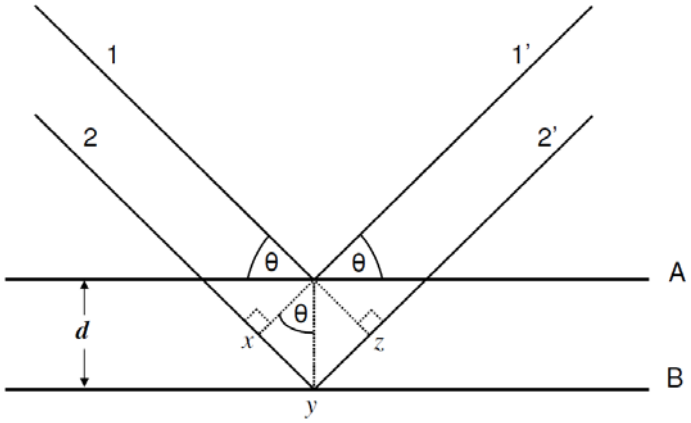

Figure 3. Diffraction paths of x-rays irradiated on crystal planes A and B, separated by distance, *d*. The Bragg angle, θ, relates to the distances *x*, *y* and *z* according to Bragg's Law (figure based on ref. [61]).

The angle of incidence is known as the Bragg angle, θ, and is related to the distances *xy* and *yz*, such that:

$$xy = yz = d \sin\theta \qquad [15]$$

$$xyz = 2d \sin\theta \qquad [16]$$

In order for the diffracted x-ray beams to be in phase, the distance *xyz* should be equal to a whole number of wavelengths: $xyz = n\lambda$. Thus, coherence in x-ray diffraction occurs in accordance with Bragg's law:

$$2d \sin\theta = n\lambda \qquad [17]$$

At angles other than θ, destructive interference occurs. Each coherent reflection corresponds to a detected x-ray signal.

Lattice planes in the unit cell of a crystal are labelled by sets of three numbers called Miller indices: *h,k,l*. These refer to the points at which the planes intercept the Cartesian coordinate axes, *x,y,z*. The interplanar distance, d, is related to the Miller indices of the planes and is dependent on the geometry of the unit cell. For example, for an orthogonal crystal with unit cell parameters, $a \neq b \neq c$, the *d*-spacing is given by:

$$\frac{1}{d^2} = \frac{h^2}{a^2} + \frac{k^2}{b^2} + \frac{l^2}{c^2} \qquad [18]$$

Brookite, one of the crystalline phases of TiO_2, is made up of orthogonal unit cells. Anatase and rutile, on the other hand, have tetragonal geometry. This type of crystal has unit cell parameters, $a = b \neq c$, and the d-spacing is thus:

$$\frac{1}{d^2} = \frac{h^2 + k^2}{a^2} + \frac{l}{c^2} \qquad [19]$$

Powder x-ray diffraction is often employed for the crystallographic analysis of TiO_2 nanoparticles. The sample is ground into a fine powder which is assumed to consist of randomly-arranged crystals. It follows from this assumption that the various lattice planes are present in all possible orientations, and that at least some of the crystals should be oriented at the Bragg angle.[62] In powder diffractometry, the sample is irradiated with a monochromatic beam of x-rays and the diffracted beams are detected by a Geiger counter or a scintillation counter that is connected to a computer. The detector, located on a movable arm, scans a range of 2θ values at a constant angular velocity. Coherent x-ray signals in the range of 2θ = 10 - 80° are usually sufficient to obtain the most essential crystallographic information.[61] The recorded signals are presented in terms of intensity and plotted against 2θ. Each crystalline phase produces a characteristic diffraction pattern which can be used as a fingerprint for identification. The two key variables in the pattern are the peak position at 2θ, taken from the d-spacing according to Bragg's law, and the peak intensity. Peak intensities can be taken as peak heights or peak areas; the most intense peak is generally assigned an intensity of 100, and the other peaks are scaled relatively. The amplitudes of the x-ray peaks from different crystallographic planes depend on the *hkl* indices, and the relative amplitudes are used to identify the different planes that are present and, subsequently, the crystalline structure of the material being analysed.[62] Fourier transformation is performed on the recorded information from x-ray spectra, in order to identify the lattice parameters (a,b,c) of the unit cell and the angles (α,β,γ) between them. Aside from the size and the shape of the unit cell, the atomic number and position of the atoms in the cell can be deduced. Anions with different atomic numbers have different scattering powers and, consequently, different diffraction intensities.[61]

X-ray diffraction is also used to obtain an estimation of the nanoparticle size based on the size of the crystallites in a powder specimen. Size is measured by XRD as the effective length in the direction of the diffraction vector, along which diffraction is coherent.[63] Crystallite size refers to the length of smallest crystallographic domain that is detectable by XRD; individual particles may contain several crystallites. It is therefore possible that the crystallite size obtained from XRD could be smaller than the sizes obtained from other characterization techniques. The basis of this determination is the inverse proportionality between the breadth of the diffraction peak and the apparent crystallite size. When monochromatic x-ray radiation hits a group of randomly-oriented crystals, the diffracted beam is broadened if the particle size is small.[64, 65] Scherrer defined peak breadth as the width at half-maximum. The crystallite size, χ, is estimated using the formula:

$$\chi = K \frac{\lambda}{b \cos\theta} \qquad [20]$$

where λ is the wavelength of the radiation; b and θ are the peak breadth and Bragg's angle, respectively, expressed in radians. The Scherrer constant, K, is a dimensionless number that is dependent on crystallite shape and crystallite size distribution.[63]

2.4 Transmission electron microscopy

Transmission electron microscopy (TEM) makes use of the scattering of electrons that pass through the sample, in order to produce an image of a surface. The scattered electrons are focused and amplified by a series of lenses and sent towards the detector[60]. Different atoms have different degrees of interaction with and absorption of electrons and it is this variation that gives rise to the image. The resolution in TEM is set in terms of the Rayleigh criterion[66], which approximates the smallest resolvable distance, δ, as

$$\delta = \frac{0.61\lambda}{\mu \sin \beta} \qquad [21]$$

where λ is the wavelength of the radiation, μ is the refractive index of the viewing medium, and β is the semi-angle of collection of the magnifying lens. This expression is simplified by approximating $\mu \sin\beta = 1$ (also called the numerical aperture). This means that the smallest resolvable distance is roughly half the wavelength of electrons, the de Broglie wavelength λ, which relates to the energy of the electrons (E, eV) and the accelerating voltage (V, kV)[60, 66]

$$\lambda = \frac{1.226}{E^{1/2}} = \frac{0.0388}{V^{1/2}} \qquad [22]$$

Electrons, being a type of ionizing radiation, produce a wide range of secondary signals from the sample. These signals are used in analytical electron microscopy, for example in X-ray energy-dispersive spectrometry (XEDS), where characteristic peaks in the X-ray spectra are used to identify and map different elements in the sample.[66]

Chapter 3: Synthesis and Characterization of TiO_2

In which we present the synthesis protocol and analyse the nanoparticle material

Historical accounts from World War II describe a chemical warfare material known as Fumigerite, a colourless liquid that reacts violently with water to produce a smoke screen that stings the eyes and throat.[67] Warships of the United States Navy dropped canisters of this chemical in the ocean in order to mask their position from bombers and Kamikaze pilots.[2, 68] This method of subterfuge was also adopted by the Japanese Army and naval landing forces, which stored the liquid in frangible smoke granades, as an infantry weapon.[69] This clear, reactive liquid is titanium tetrachloride ($TiCl_4$) which, when in contact with water, forms a white cloud of pigment (TiO_2) and hydrochloric acid.

3.1 Synthesis of TiO_2 from $TiCl_4$

What was once a last resort military measure is now one of the most important chemical routes in the production of TiO_2 nanoparticles, both at the industrial and the research laboratory scale. By controlling the reaction conditions of the hydrolysis of $TiCl_4$, nanometer sized TiO_2 of specific forms, sizes, and crystalline structures can be produced. This chapter discusses the synthesis of TiO_2 nanoparticles from $TiCl_4$ and presents the findings of Abbas, Perez Holmberg, et al.,[70] which appears as Paper I in the Appendices.

3.1.1 Examples from literature

Several possible strategies can be employed in the synthesis of TiO_2 nanoparticles from $TiCl_4$. The most common commercial route is the chloride based vapour-phase oxidation of $TiCl_4$. In this process, purified $TiCl_4$ is oxidized at high temperature (1200-1700°C), in an oxygen plasma.[71] A non-combustion alternative is the vapour-phase hydrolysis[71, 72] of $TiCl_4$ at 360-550°C. These gaseous synthetic routes produce rutile and anatase TiO_2, respectively, and are described by the chemical reactions below.

$$\overset{IV}{TiCl_4} + O_2 \xrightarrow{1200-1700^\circ C} \overset{IV}{TiO_2}(s) + 2Cl_2 \qquad [23]$$

$$\overset{IV}{TiCl_4}(g) + 2H_2O(g) \xrightarrow{360-550^\circ C} \overset{IV}{TiO_2}(s) + 4HCl(g) \qquad [24]$$

The liquid-phase hydrolysis of $TiCl_4$ at lower temperatures has been explored in several studies.[21, 73-76] Most of these synthesis protocols involve the sol-gel approach, wherein $TiCl_4$ is added to water or alcohol, or a mixture of both, at near room temperature. Subsequent condensation of the hydrolysis product results in gel formation. In some cases, the gel is precipitated from the suspension, using ammonia or another base.[75, 76] Further treatment of the gel, such as baking[21] or freeze-drying,[73] is usually employed. The resulting material is then subjected to repeated cycles of centrifugation, washing, and resuspension until the final product, usually in powder form, is considered free from organic compounds and impurities.

The sol-gel approach may be suitable for investigations that require the use of TiO_2 as thin films.[16, 77] However, for our project, it is of utmost importance that the TiO_2 surfaces be free from surfactants and impurities. Post-synthetic removal of organic material and other additives can be cumbersome and ineffective; their incomplete removal gives rise to non-negligible uncertainties in surface-related measurements. Notwithstanding the removal of additives, there is still the issue of dispersing the TiO_2 powders into a suitable suspension. More often than not, shaking and sonication are not sufficient enough to completely redisperse the TiO_2 nanoparticles to their original size, especially if significant aggregation has occurred in the drying process. Given that one of the main objectives of this PhD project is to study the size-dependence of TiO_2 surface properties, it is essential to obtain well-characterised material with known particle sizes and an acceptable level of polydispersity. Another aspect to consider is the possibility of observing physical processes, such as the particle diffusion and surface charging. The idea would be to maximise the available surface area and to study the particle-liquid interface with great precision. Hence it is beneficial that the particles are nucleated and grown directly in a simple electrolyte environment. For the reasons stated above, sol-gel synthetic methods that employ a Ti-alkoxide precursor are not explored in this study.

3.1.2 TiO_2 nanoparticles from the controlled hydrolysis of $TiCl_4$

The synthesis of nano-sized TiO_2 colloids from $TiCl_4$ was explored in earlier studies by Kormann[78] and Serpone,[79] which served as a starting point for the development of our synthesis method. The synthetic route is via the hydrolysis of $TiCl_4$, as described by the following reaction:

$$TiCl_4 + 2H_2O \rightarrow TiO_2 + 4H^+ + 4Cl^- \qquad [25]$$

The reaction of $TiCl_4$ with water is conducted under well controlled experimental conditions, placing particular emphasis on the control of temperature and ionic strength during the different stages of the synthetic process. Thus, we describe the procedure as the synthesis of TiO_2 via the controlled hydrolysis of $TiCl_4$.[70] In a typical experiment, $TiCl_4$ is kept in cold storage (-16 to -19°C) for at least 12 hours prior to its addition to de-ionised (Milli-Q) water. The receiving water is maintained at 0°C while $TiCl_4$ is added dropwise under vigorous stirring. The resulting precursor solution has a $TiCl_4$:H_2O volume ratio of 1:40 and pH < 1. The high ionic strength of this solution provides a risk for rapid aggregation of bulk TiO_2, which was observed in previous studies,[78] as well as our own early experiments. In order to obtain a more stable suspension, the Cl^- concentration was reduced and pH increased to around 2.5 by dialysis. The resulting TiO_2 suspension was then allowed to age for at least a week before further use in other experiments. Different temperatures were set for the dialysis and storage steps, with the goal of facilitating the growth of TiO_2 colloids towards a specific size range. Figure 4 schematically presents the procedure for different target sizes in detail.

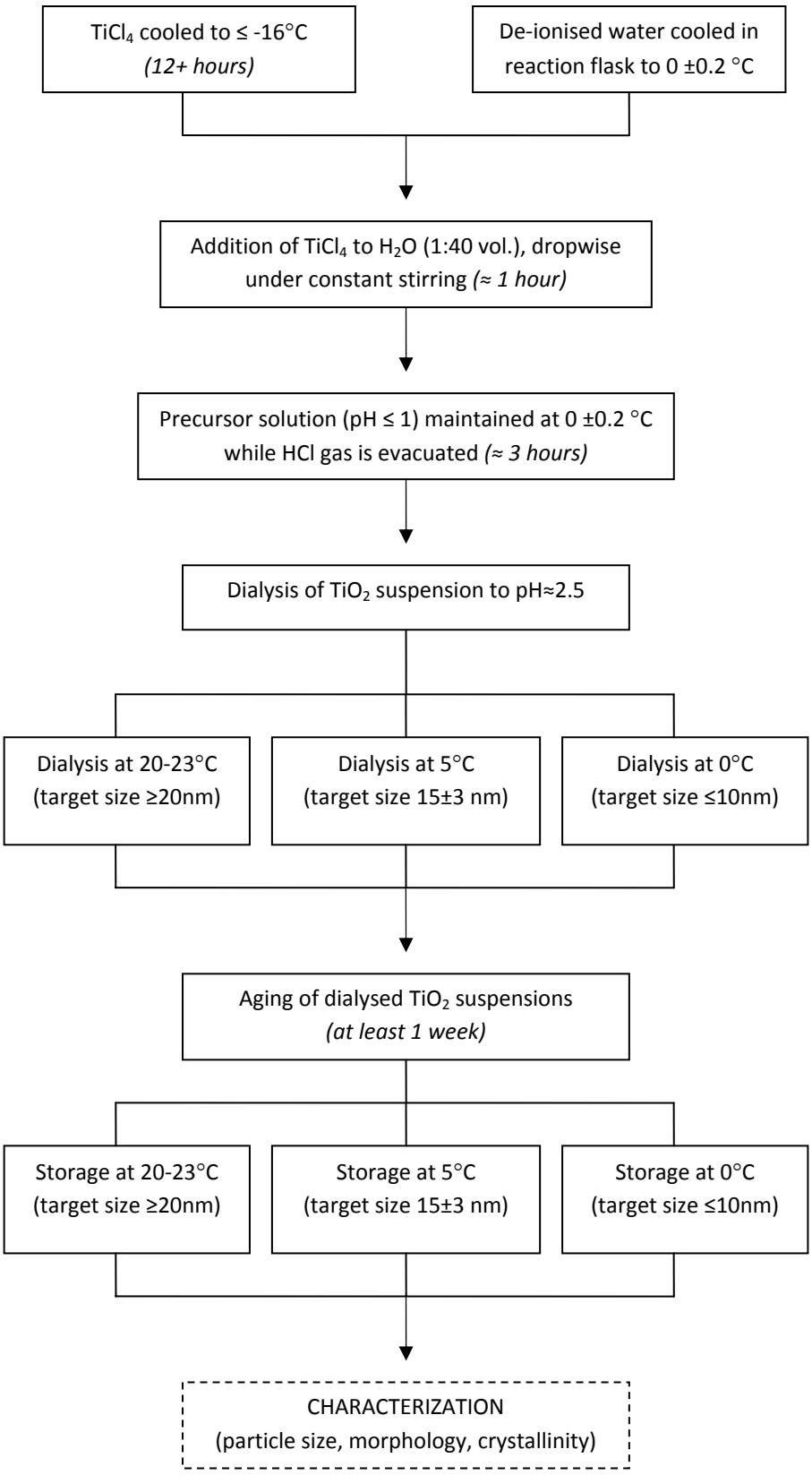

Figure 4. Schematic overview of the controlled hydrolytic synthesis of TiO_2 (Abbas *et al.* 2011)

3.2 Characterization of TiO_2 nanoparticles

3.2.1 Crystalline structure

Titanium dioxide occurs in three forms: anatase, rutile and brookite. Rutile has the highest thermodynamic stability and is thus the form most commonly found in nature.[80] Anatase and brookite transform into rutile upon heating, and the abundance of rutile rapidly increases as the temperature reaches 600°C.[21, 81] The oxygen atoms in rutile are arranged in a slightly distorted hexagonal close-packing, while a cubic-close packing applies for anatase and brookite. Half of the octahedral interstices are occupied by titanium atoms in all three structures.[1] Rutile and anatase are both tetragonal, respectively containing 6 and 12 atoms per unit cell, with anatase being the more elongated structure.[82-84] The TiO_6 octahedra are slightly distorted; the lengths of two Ti-O bonds are slightly greater than the other four. Brookite has an orthorhombic structural geometry, formed by joining together the distorted TiO_6 octahedra, sharing three edges. The Fermi level in anatase is higher than that of rutile by about 0.1 eV, resulting in different electrical and optical properties in the thin films of these polymorphs.[84] The unit cell parameters and the geometry of the three crystalline modifications are shown respectively in Table 1 and Figure 5.

Table 1. Unit cell parameters of the three crystalline phases of titanium dioxide [82, 83]

Unit cell parameter	Anatase (a = b ≠ c)	Brookite (a ≠ b ≠ c)	Rutile (a = b ≠ c)
a	3.78 Å	9.18 Å	4.59 Å
b	3.78 Å	5.45 Å	4.59 Å
c	9.51 Å	5.15 Å	2.96 Å

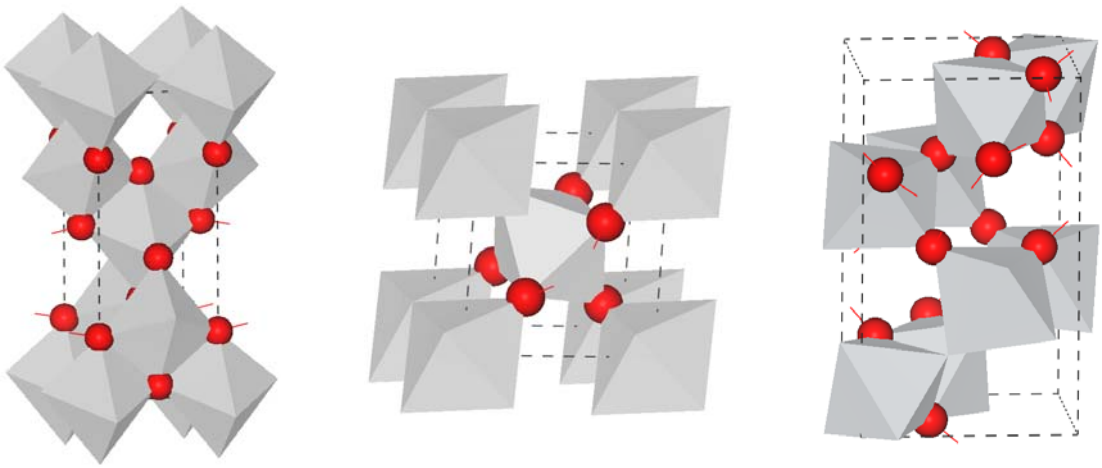

Figure 5. Unit cells of three TiO_2 polymorphs (from left): anatase, rutile, and brookite. Anatase and rutile exhibit tetragonal geometry while brookite has an orthorhombic configuration (*figures courtesy of Michael Busch*).

The crystalline structure of the TiO_2 nanoparticles was determined using grazing angle powder X-ray diffraction. The powdered samples were obtained by drying TiO_2 suspensions from different synthesis conditions for about 16 hours at 120°C, a temperature just sufficient

for the removal of the liquid solvent. The dried solids were then ground into fine white powders. The equipment used, as well as the details of the diffraction scan, are described in Paper I.[70] Figure 5 presents the diffraction patterns of TiO_2 from the three different sets of synthesis conditions described in the previous section.

The results show that anatase is the predominant phase, with the strongest peak corresponding to the (1 0 1) reflection at $2\theta = 25.3°$; all major anatase peaks up to $2\theta = 60°$ are accounted for. The presence of brookite, however, cannot be disregarded. The brookite (1 2 1) reflection at $2\theta = 30.84°$ is clearly evident. Furthermore, the (1 2 0) and (1 1 1) reflections, which often appear as a double peak at $2\theta = 25.4°$ and $25.7°$ respectively, overlap with the primary anatase peak. Thus, the contribution of brookite to the observed properties of the synthesized TiO_2 should be taken into consideration.

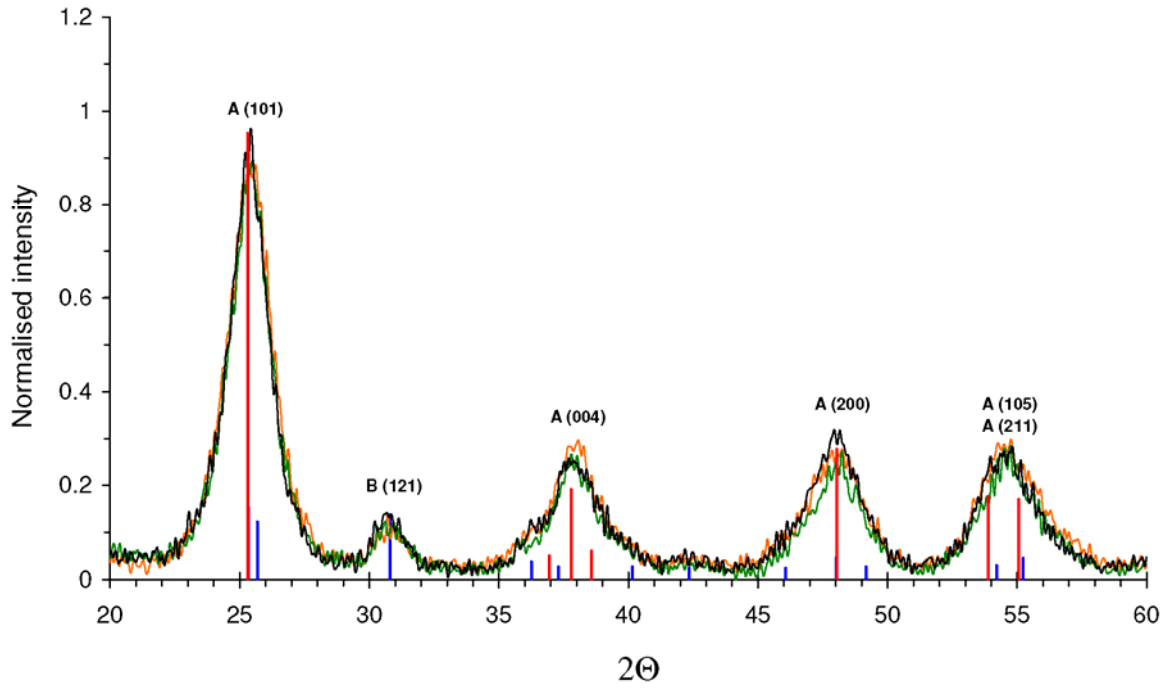

Figure 6. Results from X-ray diffraction experiments on TiO_2 nanoparticles produced by different experimental conditions. The orange, green and black XRD patterns refer to TiO_2 obtained from suspensions containing 8 nm, 10 nm, and 18 nm particles, respectively. The red and blue lines represent the crystallographic reflection planes for anatase and brookite, respectively. (Reprinted from Abbas *et al.* 2011.)

A detailed peak analysis was conducted in order to obtain the relative composition of the two phases. Gaussian fitting made it possible to deconvolute overlapping peaks and based on the calculated peak areas, the TiO_2 nanoparticles were found to be at least 92% anatase. Anatase particles with a particle size below 14 nm are found to be more stable than rutile.[85] At this size scale, the formation of anatase is energetically favourable due to the lower surface tension of this structural configuration.[80, 85, 86] Previous studies on the surface free energy of the different crystalline phases, taking into account the effects of surface stress in the nanometer scale, have evaluated phase stability with respect to temperature and particle size.[80] At sizes ≤ 11 nm, anatase is only marginally more stable than brookite.[81, 87] Rutile is the preferred orientation at particle sizes ≥ 35 nm.[80, 81, 87] The occurrence of brookite as a by-product in low-

temperature hydrolytic synthesis is by no means uncommon.[80, 88, 89] This is particularly evident when a chloride-containing reaction precursor is used, and it has been observed in previous investigations that Cl^- ions are essential in brookite formation, as it acts as an orientation template at the early stages of condensation[90] and stabilizes the structure against recrystallisation to rutile.[88]

Mild heat treatment of the hydrolytically synthesized TiO_2 suspensions demonstrates phase transformation behaviour even at relatively low temperatures. After the addition of $TiCl_4$ and prior to dialysis (pH < 1), the TiO_2 precursor solution was heated at 95°C for 2 hours in an oven at ambient pressure. The heated suspension was allowed to cool to room temperature, and subsequently dialysis was performed until pH ≈ 2.5. The product was subjected to the same drying and powder preparation as described earlier in this section. The XRD pattern for the heat-treated sample, along with that for a typical sample of synthesized TiO_2, is shown in Figure 7. The anatase peaks are sharper and more intense in the heat-treated sample, compared to those of the untreated sample. Furthermore, the brookite (1 2 1) peak disappears and a phase transition to rutile is clearly evident. Gaussian peak analysis reveals the phase composition to be 83% anatase and 16.5% rutile. Brookite cannot be directly determined by Gaussian analysis in this case, due to overlaps with the strong anatase peaks; the remainder of the (1 2 1) peak places brookite composition at around 0.5%. Jolivet *et al.*[90] investigated the thermolysis of $TiCl_4$ at 90°C in high concentrations of HCl (1-5 M) and have found that, as long as chloride ions are present in the suspension, brookite nanoparticles remain stable. When chloride was replaced with perchloric anions, the brookite transformation to rutile was complete after some hours. The chloride concentration in the precursor solution is about 200 mM, which is at least five times less than in the test solution of Jolivet *et al.* The transformation to rutile in this case is thus expected.

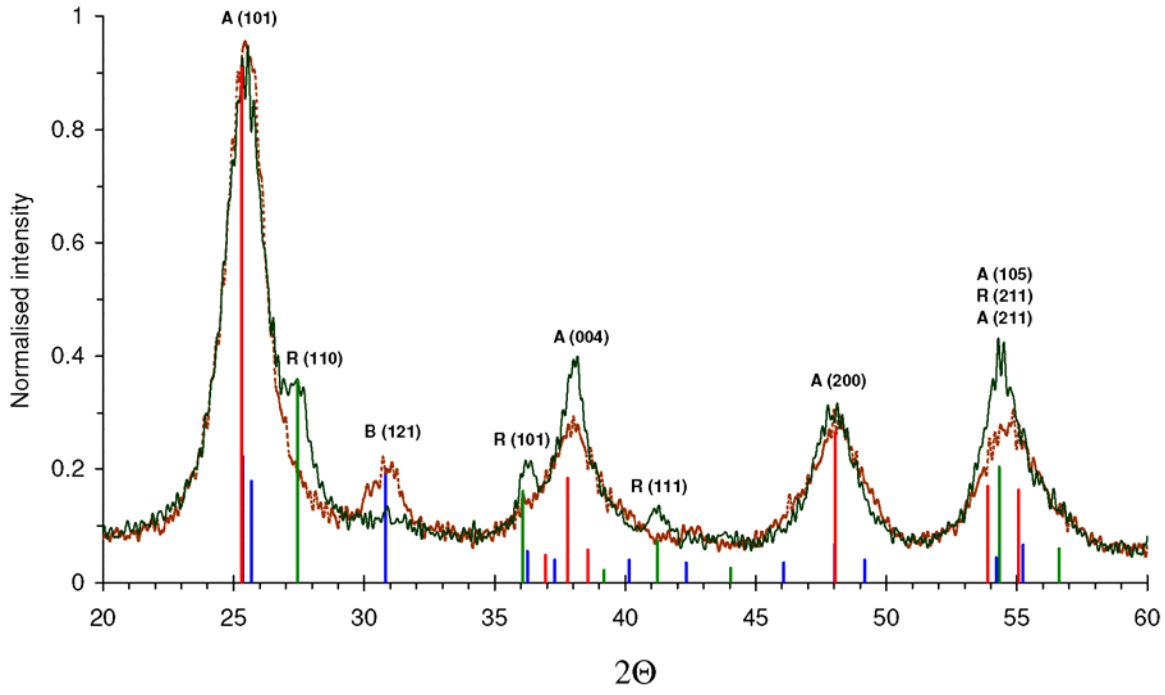

Figure 7. Phase transformation to rutile at 95°C, shown by the green XRD pattern. The dotted XRD pattern represents a sample that was not subjected to heat treatment. The red, blue and green lines represent the crystallographic reflection planes for anatase, brookite, and rutile, respectively.

3.2.2 Particle size determination

One of the most important parameters in the investigation of properties and processes in the colloidal domain is, of course, particle size. The crystallite size obtained from x-ray diffraction describes the smallest crystal domains in the structure and can be taken as indicative of primary particle size. However, there are other techniques that provide measures of size, as well as other system characteristics. The measurement approaches and the type of size information vary and some considerations have to be made regarding sample preparation and system perturbation. Nevertheless, the use of complementary sizing methods serves to strengthen the characterization of the synthesized material.

3.2.2.1 The Scherrer crystallite size

The crystallite sizes obtained from each set of synthesis conditions were calculated using the Scherrer formula, as described in Chapter 2. Prior to sample preparation, the sizes of the particles were determined using DLS and ES-SMPS. The TiO_2 nanoparticles were found to be about 8 nm, 10 nm, and 18 nm in diameter. These sizes were obtained from the dialysis and aging of suspensions at 0°C, 5°C and room temperature, respectively. The calculated Scherrer crystallite diameters are presented in Table 2 below.

Table 2. Crystallite size (anatase) from different synthesis conditions, presented in comparison with sizes obtained from DLS and ES-SMPS (Abbas *et al.* 2011).

Dialysis and aging Temperature (°C)	Scherrer crystallite diameter (nm)	DLS hydrodynamic diameter (nm)	ES-SMPS number-average diameter (nm)
0	3.9 ± 0.1	7.8 ± 0.6	8.6 ± 0.8
5	4.0 ± 0.0	10.2 ± 0.4	9.2 ± 1.6
20-23	4.2 ± 0.1	18.0 ± 0.0	18.5 ± 2.4

The remarkable feature in these results is that, regardless of synthesis conditions, the crystallite sizes obtained are similar. The Scherrer size describes the most fundamental crystal domain and as such, it can be taken as a measure of primary particle size. The particle sizes obtained by the other two characterisation methods are larger. This may be interpreted as indicative of particle growth by slow aggregation. However, other influences on the observed DLS and ES-SMPS particle sizes need to be taken into consideration. These factors are discussed in more detail in the following section and in the next chapters of this work.

Anatase, being the predominant phase, was the focus of comparison in Article 1. The calculations were based on the A (1 0 1) reflection, which is the strongest peak, and A (2 0 0), which does not have significant overlaps with the brookite peaks. However, there can be up to 8% brookite in the synthesis products, so it is worthwhile to also look at the crystallite size that is obtained from the brookite (1 2 1) peak. Table 3 presents the phase composition and crystallite sizes for anatase and brookite. For both phases, the crystallite sizes are similar, regardless of synthesis conditions.

Table 3. Percent composition and crystallite sizes of anatase and brookite from different synthesis conditions (Abbas *et al.* 2011).

Dialysis and aging Temperature (°C)	% Anatase	Anatase crystallite diameter (nm)	% Brookite	Brookite crystallite diameter (nm)
0	94.8 ± 1.3	3.9 ± 0.1	5.2 ± 1.3	7.2 ± 0.3
5	91.8 ± 0.4	4.0 ± 0.0	8.3 ± 0.4	7.1 ± 0.5
20-23	92.3 ± 0.0	4.2 ± 0.1	7.5 ± 0.0	7.3 ± 0.3

3.2.2.2 Transmission electron microscopy

An image of the TiO_2 particles synthesized and aged at 0°C is presented in Figure 8. Though the deposited oxide layer is of uneven thickness and agglomerates are visible, the TEM image indicates that the sample is composed mostly of particles that are roughly 4 nm in diameter, which corresponds to the XRD crystallite diameter, assuming an anatase structure. Distinct fringe patterns point towards a crystalline product. The average size between two rows is about 4 Å, which closely relates to the unit cell structure of anatase in two directions (see Table 1). Artefacts introduced by sample preparation, which consisted of air-drying a drop of stock TiO_2 suspension directly on the TEM grid (Cu with carbon film), make it difficult to conduct a statistical analysis of the image. Thus, other sizing methods are necessary in order to obtain statistical averages and particle size distributions that better describe the TiO_2 particle system.

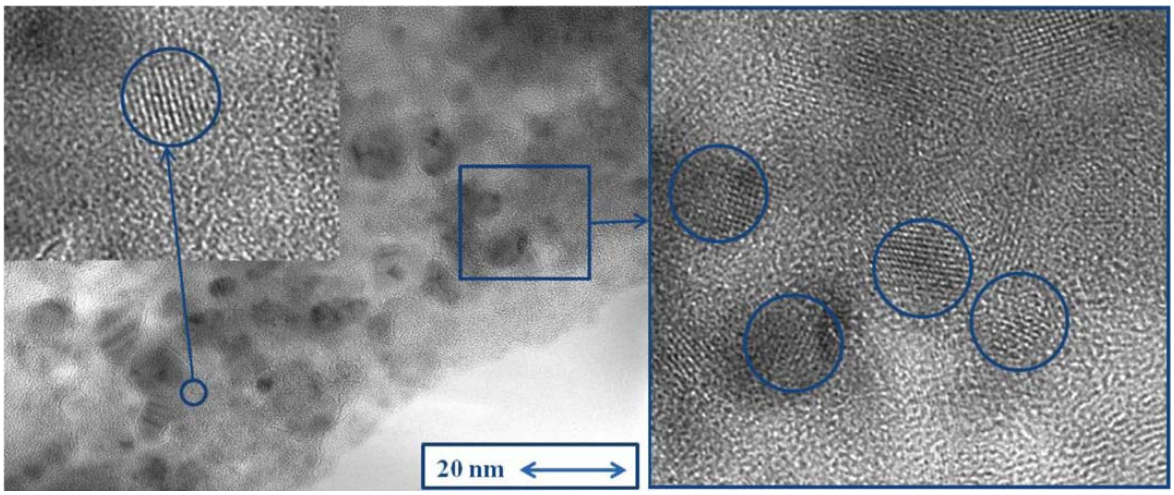

Figure 8. Transmission electron micrographs of a sample of TiO_2 particles, synthesized and aged at 0°C, showing a mix of aggregates and smaller particles. The magnified images show distinct fringe patterns that are indicative of a crystalline sample (Abbas *et al.* 2011).

3.2.2.3 Dynamic light scattering

Dynamic light scattering provides an ensemble average based on the collective diffusion coefficient of a sampled volume of particles, as discussed in Chapter 2. For particles that are small, relative to the wavelength of light (633 nm, in this case), the intensity of scattered light is proportional to the sixth power of particle size.[25] The z-average diameter obtained from DLS is thus an intensity weighted average, defined by[25, 91]

$$d_z = \frac{\sum_i n_i d_i^6}{\sum_i n_i d_i^5} \qquad [26]$$

The fluctuation of scattered light intensity due to diffusion is the observed parameter; size in this case is a derived value. The concentration of the analyte sample is important for a number of reasons. Depending on the refractive index of the material, the concentration is selected so that there is sufficient detectable light scattering, but still in the regime that does not induce multiple scattering. When taken in the context of interparticle distance, concentration is relevant as it affects the measured collective diffusion coefficient, D_M. Collective diffusion is influenced by direct interactions between charged particles, as well as by hydrodynamic interactions facilitated by the solvent. Repulsive electrostatic interactions lead to an increase in D_M with concentration; an inverse proportion is observed for attractive Van der Waals interactions.[25] A simple way of accounting for these contributions is to extrapolate D_M to infinite dilution, towards the single-particle Stokes-Einstein diffusion coefficient, D_0, which is then used to determine the hydrodynamic particle size (Eqn. 4 in Chapter 2). Figure 9 illustrates an example of this extrapolation, and the hydrodynamic diameters of samples taken from storage at 5°C and room temperature are shown to be 10.9 and 18.8 nm, respectively.

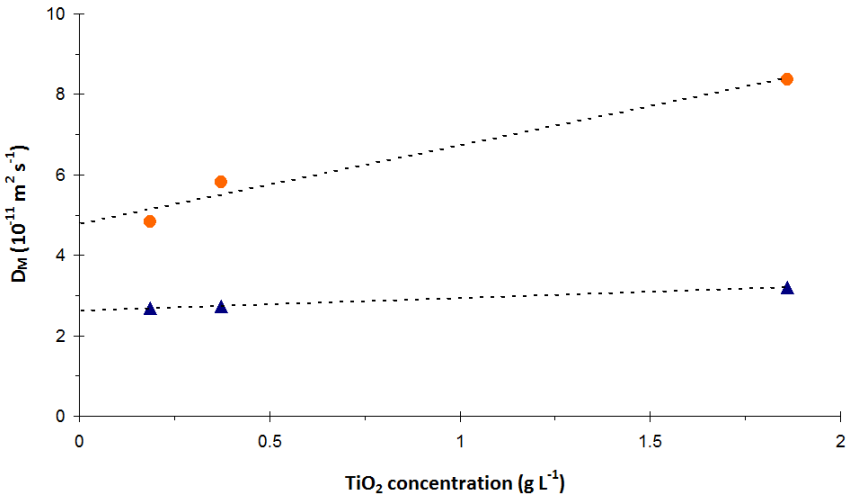

Figure 9. Extrapolation of D_0 for two TiO_2 particle sizes. The circles and triangles represent measured diffusion coefficients that produce calculated hydrodynamic diameters of 10.9 nm and 18.8 nm respectively (Abbas *et al.* 2011).

3.2.2.4 Electrospray-Scanning Mobility Particle Sizer

The differential mobility analyzer contained within the SMPS system reports size as an electrical mobility diameter, d_m. This is the diameter of a sphere with the same migration velocity in a constant electric field as the particle of interest.[92] Assuming spherical particles, d_m is equivalent to the physical diameter, d_p.[48] Different particle sizes have different mobilities through an applied electrical field, making it possible to measure different size fractions in a mixture of particle sizes. After size differentiation in the DMA, the particles are

transported to the condensation particle counter, where they are counted individually. Hence, ES-SMPS gives number-based particle size distributions. Figure 10 displays the particle size distributions obtained from three different sets of TiO_2 synthesis conditions. The number-average diameter is taken from the peak of the size distribution. Shifts in the peak and changes in the shape of the distribution over time are indicative of aggregation in the system, as in the case of the particles aged at 0°C and 5°C. At least three weeks of aging is necessary to obtain relatively stable TiO_2 suspensions.

The ES-SMPS technique has also been used to follow the particle formation and growth over the early stages of synthesis and suspension aging. These measurements are presented and discussed in detail in the next chapter.

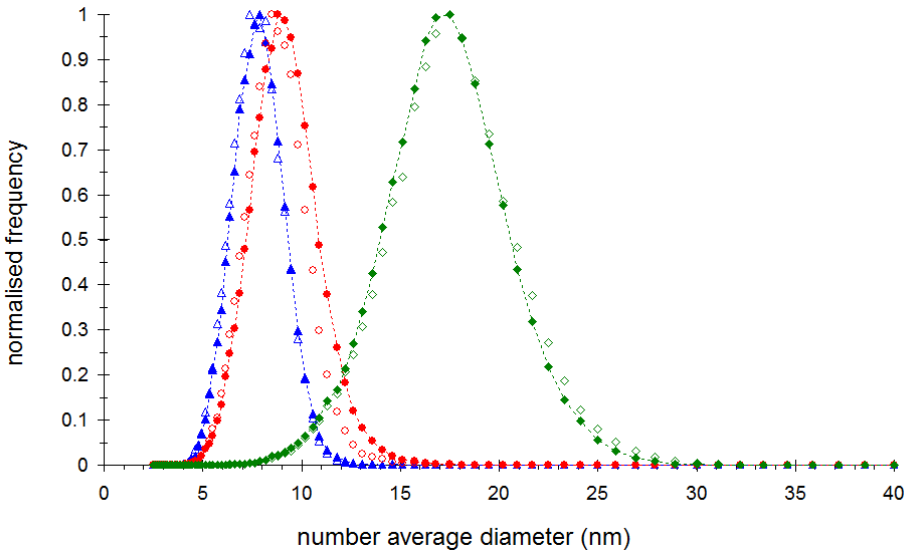

Figure 10. TiO_2 particle size distribution from ES-SMPS measurements on suspensions that were dialysed and aged at 0°C (triangles), 5°C (circles) and at room temperature (20-23°C, diamonds). The unfilled and filled symbols respectively belong to results obtained after 1 week and 3 weeks into the aging period (Abbas *et al.* 2011).

3.3.4 Comparison between sizing methods

Electron microscopy has its advantages because it provides a visual image of the particle sample and can also be used for elemental mapping. However, due to complexities in sample preparation, the full range of use has not been employed in the analysis of the synthesized TiO_2 nanoparticles. Dynamic light scattering and ES-SMPS each have their benefits and drawbacks, but the two are complementary methods that prove to give a greater understanding of the particle system, when used together. Given that two types of particle sizes are obtained, a hydrodynamic and number-average size respectively, direct comparison of results should be approached with caution. In order to avoid comparing apples with oranges, it serves well to calculate a z-average diameter from ES-SMPS size distribution data, using Equation 26 (Section 3.2.2.3). This conversion takes into account the contribution of the larger particles in the size distribution and results in an intensity-weighted size value similar to that obtained from DLS.

Some TiO_2 samples were comparatively analysed with ES-SMPS and DLS. Measurements were done on two consecutive days, in order to have as similar system conditions as possible. The results are presented in Table 4.

Table 4. Comparison of TiO_2 particle sizes obtained from DLS and ES-SMPS (Abbas et al. 2011)

Dialysis and aging temperature (°C)	Z-average hydrodynamic diameter (nm) DLS	Number-average diameter (nm) ES-SMPS	Calculated z-average diameter (nm) ES-SMPS
0	10.3 ± 0.09	7.7 ± 0.16	8.7 ± 0.02
5	10.9 ± 0.12	8.9 ± 0.18	10.5 ± 0.06
20-23	18.8 ± 0.17	17.7 ± 0.35	19.4 ± 0.01

3.4 Commentary on TiO_2 synthesis and characterization

The hydrolysis of $TiCl_4$ is an effective route for the synthesis of TiO_2 nanoparticles specifically for the study of surface phenomena. The surfactant-free product provides direct access to the oxide surface and makes it possible to accurately observe interfacial processes. By careful control of the synthesis conditions, well-defined particle sizes with a high degree of crystallinity can be obtained. The results show that primary particles of around 4 nm are created, but that the smallest stable particle size detectable from the TiO_2 suspension is around 8 nm. This indicates that particle growth in this system occurs via slow aggregation, with the formation of dimers and trimers.

A number of aspects need to be considered, with respect to the characterization techniques. Measurements on DLS are greatly influenced by factors that affect diffusion. Sample concentration and the electrolyte environment play a role in ES-SMPS, and one of the key considerations in particle detection is the formation of evaporation residues. These analysis techniques are further explored in the next two chapters, juxtaposed with investigations on the particle formation and growth mechanisms of hydrolytically synthesized TiO_2.

Chapter 4: TiO_2 Nanoparticles from Hydrolysis

In which we examine the mechanisms that lead to the formation and growth of TiO_2

In the previous chapter, the experimental protocol for the production of TiO_2 nanoparticles was presented. It is worthwhile to closely examine the mechanistic details of $TiCl_4$ hydrolysis, in order to determine the important factors that brought about the structure and size characteristics observed in the synthesis products. The processes that occur in the initial stages of synthesis, through the dialysis, and up to the first week of aging are scrutinized in an attempt to provide a complete picture of TiO_2 particle formation via hydrolysis. With these in mind, the key findings from Perez Holmberg *et al.*[93] (Paper III) are discussed in this chapter.

4.1 Hydrolysis of $TiCl_4$

Reaction 25 in Chapter 3 provides a simplified view of hydrolysis. Whereas this overall reaction does recognize the contribution of both protons and chloride counterions to the surrounding electrolyte, it neglects the dissolved Ti-species and intermediates that coexist in solution until the complete transformation of Ti^{4+} to the solid oxide. One should remember that this particular colloidal system is sensitive to perturbations in the charged solution environment; conditions are dynamic and shifting throughout the synthetic process. The relevant equilibria[94-96] in the hydrolysed precursor solution are presented in Table 5.

Table 5. Complexation and formation equilibria in the $TiCl_4$ hydrolysis solution

Reaction	Log β	Reference
$TiOH^{3+} + H_2O \leftrightarrow Ti(OH)_2^{2+} + H^+$	- 1.80	94
$TiOH^{3+} + 2H_2O \leftrightarrow Ti(OH)_3^{+} + 2H^+$	- 4.20	94
$TiOH^{3+} + 3H_2O \leftrightarrow Ti(OH)_4 + 3H^+$	- 6.30	94
$TiOH^{3+} + 2H_2O \leftrightarrow TiO(OH)_2(s) + 3H^+$	-1.30	95
$TiOH^{3+} + Cl^- \leftrightarrow TiOCl^+ + H^+$	- 1.25	96
$TiOH^{3+} + 2Cl^- \leftrightarrow TiOCl_2 + H^+$	- 1.65	96
$TiOH^{3+} + 3Cl^- \leftrightarrow TiOCl_3^- + H^+$	- 2.68	96
$TiOH^{3+} + 4Cl^- \leftrightarrow TiOCl_4^- + H^+$	- 3.75	96

4.1.1 Hydrolysis in the precursor solution

Upon the addition of $TiCl_4$ to H_2O, a drastic pH change occurs in the solution. Concentrated (99%) $TiCl_4$ is added, dropwise, in 0.5 mL increments. This means that at the first addition, the pH changes from near neutral to 1.26. The precursor solution becomes increasingly acidic until the final $TiCl_4$ addition, where pH = 0.72. As the Cl^- ionic strength increases, the formation of Ti-oxychloride complexes becomes more significant. The complex speciation can be estimated using formation constants for the Ti-oxychloride[96] and Ti-hydroxy complexes.[94, 95] Figure 10 shows the expected distribution of Ti-complexes in the precursor

solution as a function of pH. The fraction of the total Ti concentration that exists in soluble form ($C_{Ti\text{-}dissolved}$) over the acidic pH range is shown as black dots. This soluble concentration is further subdivided into the different oxychloride and hydroxy complexes. The calculations were made using the SolGasWater software.[97]

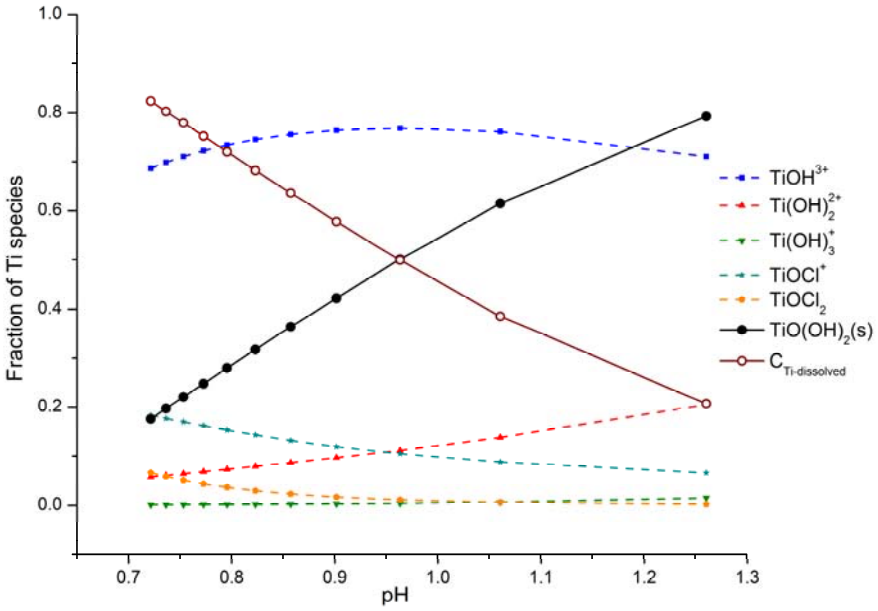

Figure 11. Distribution of Ti-complexes in the precursor solution. The dark red unfilled points depict the fraction of dissolved titanium species relative to the total concentration of titanium in solution, while the black points represent the amount of solid titanium. The distribution of titanium complexes in the dissolved portion is shown in the dashed lines (Perez Holmberg *et al.* 2012).

As seen from the $C_{Ti\text{-}dissolved}$ plot, after the first incremental $TiCl_4$ addition (pH = 1.26), only a small fraction exists in soluble form (i.e., more than 80% of the Ti ends up in a solid product). The instantaneous precipitation of titanium at pH ≥1 has been reported in the literature,[85] resulting in a quasi-amorphous solid. However, the soluble fraction of titanium increases with increasing total concentration, as the pH becomes lower with each $TiCl_4$ addition. Each additional $[H^+]$ increment brings about a shift in the complexation equilibria, resulting in the dissolution of a portion of the initially-precipitated product. When the entire 5.50 mL of $TiCl_4$ has been added, most of the titanium is in soluble form, with $TiOH^{3+}$ being the dominant hydrolysis product. Only about 30% of the soluble species in the final precursor solution are chloride complexes. According to the simulations, the solid Ti product should also be present in small amounts at pH 0.72. However, this was not detected with certainty when the precursor solution was tested experimentally.

4.1.2 Complexation and precipitation during dialysis

After the addition of $TiCl_4$, the first amorphous solid Ti species is believed to exist in the precursor solution, albeit in very small amounts, most likely as a hydrated titanium oxyhydroxide phase.[85] Particle suspensions have been observed to be stable at higher pH and lower ionic strength[70, 78, 79] than in the precursor solution, and these conditions in the suspending medium are brought about via dialysis.

As the pH is increased during dialysis, the chloride concentration correspondingly decreases, as chloride ions are continuously leached out of the dialysis solution. The system is dynamic and the equilibria are shifting, until the dialysis is terminated. This implies a changing complex speciation over time. As with the earlier simulations on the precursor solution, the complex formation constants are used to approximate the distribution of the different Ti-species and the chloride concentration was calculated from experimental pH and conductivity data. The titanium speciation in the dialysis solution is presented in Figure 12.

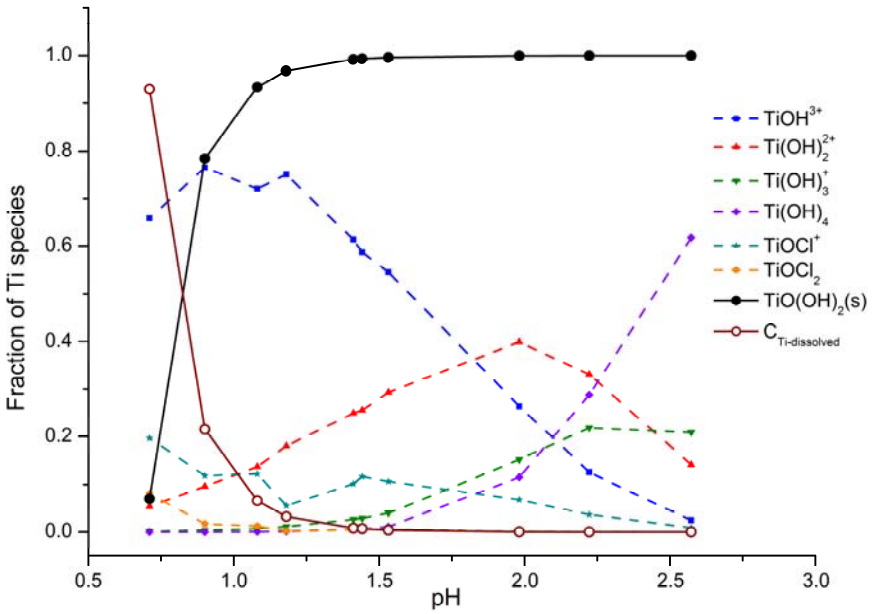

Figure 12. Distribution of titanium species during dialysis from pH 0.7 to just above pH 2.5. The black points represent the amount of solid titanium in suspension, shown relative to the total fraction of dissolved titanium species (dark red unfilled points). When pH reaches 1.5, virtually all of the titanium exists as suspended solids. The distribution of titanium complexes in the dissolved portion is shown in the dashed lines (Perez Holmberg *et al.* 2012).

The species distribution shows a rapid increase in the amount of solid material in the initial stages of dialysis. By the time the pH reaches 2, virtually all of the dissolved species, mainly hydroxyl complexes, have precipitated from the solution. The solubility of TiO_2 is very low at pH ≥2,[95] and as the system enters this pH regime, the particle growth is closely linked to the variation in electrostatic surface charge density[85] and the surface energy[86] of the particles. If the particles possess a high surface energy, the system spontaneously strives to decrease the interfacial solid-solution area by growing in size, hence minimizing the surface energy. Another way to decrease the surface energy is by adsorption, which is related to interfacial tension (γ) by Gibbs' Law:[86]

$$d\gamma = -\Gamma_i \, d\mu_i \qquad [27]$$

where Γ_i is the adsorption density of the i species under the chemical potential μ_i. In aqueous medium, protons are significant adsorbed species. Particle growth during dialysis occurs due to a combination of these two surface energy minimizing factors. By continuously changing the pH of the solution, one perturbs the adsorption equilibria (assuming a reversible adsorption), hence altering the surface energetics. Protons are continually drawn

away from the particle surface, and the particle compensates for the additional energy by growing in size.

The dialysis is indeed an important stage in the synthesis of stable particles by controlled growth. The final particle sizes have been found to be quite dependent on the frequency of water change during dialysis, especially during the first three hours. A slow dialysis, wherein the particles are suspended in a high ionic strength solution for prolonged periods of time, means that the charged particles are strongly screened by the Cl^- ions. The reduction of the electrostatic repulsion then leads to aggregation.[70] In this scenario, there is less control over particle growth and the precipitation of bulk-sized TiO_2 has been observed to occur when suspensions are left undialysed in pH ≤1.

4.2 Experimental results

Experimentally, the formation and growth of TiO_2 from the intermediate complexes produced by $TiCl_4$ hydrolysis was studied by following the changes in detected particle size during the course of synthesis. ES-SMPS and DLS were utilized for this purpose.

4.2.1 Measurements with ES-SMPS

The ES-SMPS instrumental settings were optimized prior to the analysis of the Ti colloidal system. In order for accurate measurements to be made, a number of influential factors need to be taken into account: the size of the aerosol droplets formed by the electrospray (d_d), the sample flow rate (Q_L), the solution conductivity (κ), and the presence of non-volatile species other than the particles being studied. These factors are related to the occurrence of evaporation residues as a by-product of the electrospray process and scale with the droplet size by[41, 98]

$$d_d \propto \left(\frac{Q_L \varepsilon \varepsilon_0}{\kappa} \right)^{1/3} \qquad [28]$$

$$d_d \propto \frac{1}{c^{1/3}} d_m \qquad [29]$$

where c is the concentration of the non-volatile species, ε is the solution dielectric constant and ε_0 is the vacuum permittivity. Equations 28 and 29 apply at constant concentration and constant flow rate.

Different flow rates were tested at a fixed concentration to optimize operating parameters in order to distinguish between evaporation residues and particulate matter. The tests were done on two systems: a suspension of SiO_2 nanoparticles in sucrose, and a sample of aged TiO_2 nanoparticles in a $FeCl_3$/HCl solution. The results of these tests are shown in Figure 13. Sucrose has been used to test electrospray conditions in previous studies,[98] and the wide difference in size between the sucrose residues and the SiO_2 particles makes it easy to distinguish their respective peak characteristics. Regardless of the presence of SiO_2 particles, the sucrose peak follows $(Q_L)^{1/3}$ dependence. Aside from the change in the sucrose peak position, the peak breadth also increases. In contrast, the SiO_2 peak does not shift position; it

only increases in height correspondingly to the increase in the amount of particles introduced by the higher sample flow rate. The next step was then to try and analyse the $TiO_2/FeCl_3/HCl$ system in terms of these distinguishing characteristics.

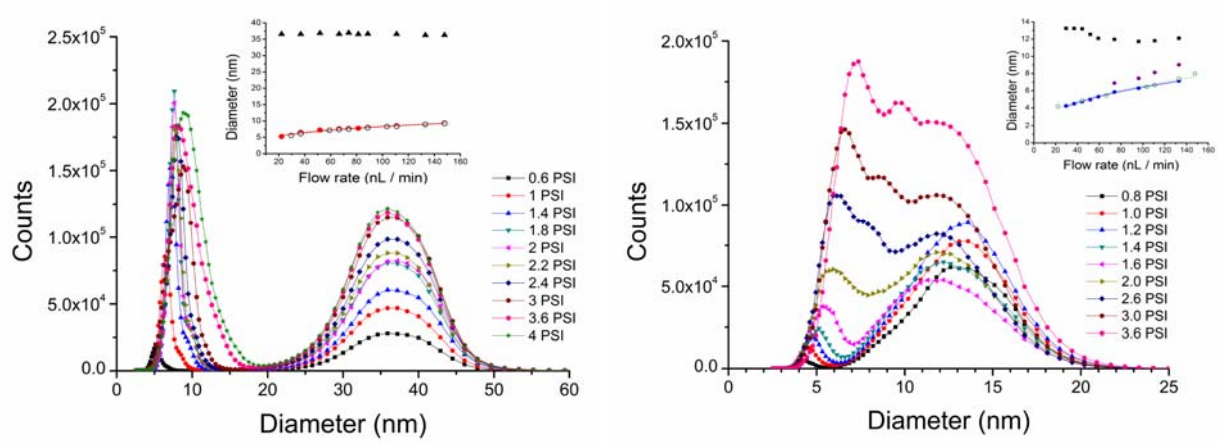

Figure 13. Differentiation of particles from evaporation residues at different sample flow rates (the capillary pressure drop of 1 PSI ≈ 37 nL/min). The inset graphs present the diameters with respect to the flow rate, the filled and unfilled circles respectively illustrating the flow rate dependence of the suspension medium with and without particles. *Left panel:* size distribution of a 0.01 v/v% sucrose/buffer solution containing 36.6±0.2 nm SiO_2 nanoparticles. *Right panel:* size distribution of a suspension of TiO_2 nanoparticles in a 0.96 mM $FeCl_3$/HCl solution at different sample flow rates (Perez Holmberg *et al.* 2012).

A couple of differences between the two particle systems have to be noted. First, due to the higher conductivity of the $FeCl_3$ solution, a smaller initial droplet size d_d is to be expected. Secondly, the viscosity of sucrose is greater than that of HCl; this may imply a different droplet formation process. These factors are taken into consideration in the evaluation of the test results.

At the lowest flow rates, the $FeCl_3$ residue peaks and the TiO_2 particle peaks are distinguishable. However, as the flow rate is increased, the peaks start to overlap due to the shift in the residue peak according to the $(Q_L)^{1/3}$ dependence. The peak position of TiO_2 is initially constant, and then when the flow rate reaches 45 nL/min, a slight drop in the measured diameter is observed, after which the size is again independent of flow rate. Corresponding to the drop in TiO_2 size is the emergence of a peak intermediate between the two main peaks. This can be taken as an indication that the TiO_2 material is composed of loosely bound aggregates of smaller primary particles, an explanation which is supported by the XRD and TEM results in Chapter 3. The intermediate peak arises from the separation of loose material from the aggregate. Furthermore, the shift in the intermediate peak with flow rate is probably due to the deposition of salt from the electrolyte on the small particle fragments. Knowing this about the behaviour of HCl-dispersed TiO_2 in the ES-SMPS system, the sample flow rate was kept below 45 nL/min for the growth monitoring experiments.

The results from the size measurements by ES-SMPS during the synthesis and the first week of aging are presented in Figure 14.

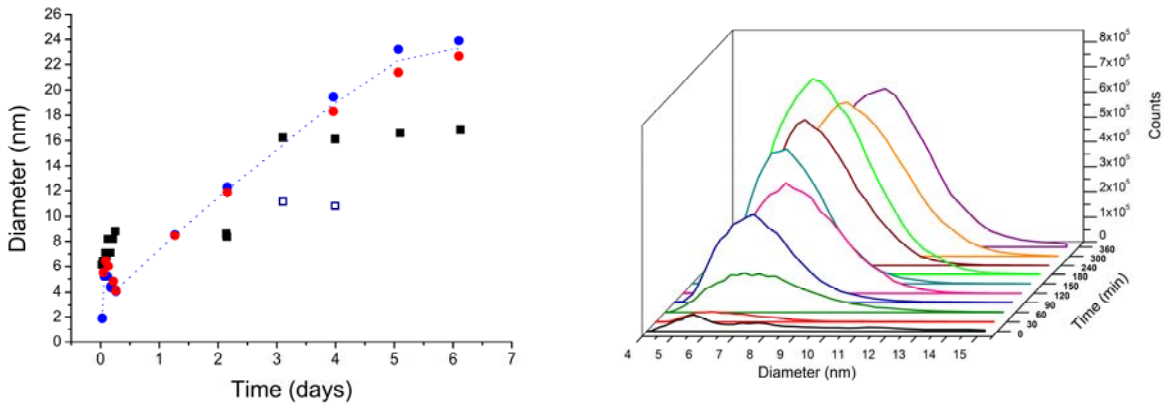

Figure 14. Size data obtained during the dialysis of TiO_2 suspensions and the first 6 days of aging. *Left panel*: Particle diameters obtained from ES-SMPS (squares) and DLS (circles) measurements. The blue and red circles represent samples taken from 2 different dialysis bags. *Right panel*: particle size distributions obtained from ES-SMPS for the precursor solution and the suspension during dialysis (Perez Holmberg *et al.* 2012).

In the precursor solution, the size distribution is not well defined and the magnitudes of the peaks are small. No reliable size data was obtained from complementary DLS measurements either (details in the next section), hence the analysis is done for the suspensions during dialysis and into the start of the aging period. After the first dialysis step, a small, but better defined peak is obtained. As the pH is increased, the distribution peaks become higher, indicative of an increase in the number of particles and consistent with the simulation in Section 4.1.2. Given the pH and conductivity conditions in the dialysis suspension (experimental data for these are found in Paper III), the expected residue size is around 10-40 nm; the peaks in the size distribution are thus due to actual TiO_2 particles. The particle diameter increased from about 6 to 9 nm during the dialysis and up to the first 2 days of aging. On days 3 to 4, the size of the particles has increased and the size distribution is bimodal. Afterwards, the diameter stays constant at about 16 nm.

A couple of method related considerations call for mention. The first is that the working detection limit of the DMA for this particular system is a minimum diameter of about 3.5 nm. This means that the nuclei formation from the initial precipitation from the Ti-complexes cannot be detected. Another consideration is the highest concentration that can be analysed by the CPC, such that the particles are counted individually (recall counting mechanism in Section 2.2.3). For this reason, the test suspensions measured with ES-SMPS were diluted to a little over 300 times from the original concentration in 10 mM (pH 2) HCl. As a complementary analysis, DLS measurements were thus conducted with the aim of monitoring the particle growth in real-time and in the actual electrolyte environment of the synthesized suspension.

4.2.2 Measurements with DLS

The DLS measurements were conducted directly on undiluted samples and the measured collective diffusion coefficient was used to calculate an apparent hydrodynamic diameter using the Stokes-Einstein relation (Eqn. 4 in Sec.2.1.1). It was not possible to reliably extract the diffusion coefficient from the intensity autocorrelation functions of the precursor solution, thus the diameters presented in Figure 14 are those obtained during dialysis and the

first 6 days of aging. Looking more closely at the particle sizes during the dialysis, it can be seen that, while the ES-SMPS size increases monotonically with time, the hydrodynamic diameter exhibit a maximum about 2 hours into the dialysis, as shown in Figure 15 below.

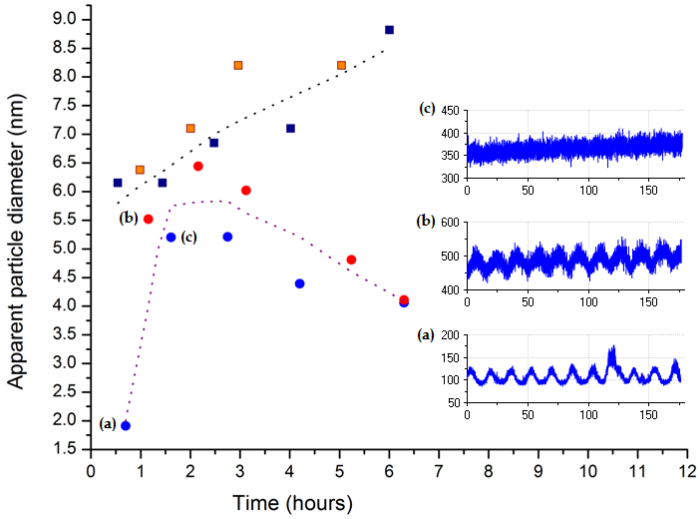

Figure 15. Particle diameters obtained from ES-SMPS (squares) and DLS (circles) during dialysis. The different coloured points depict that samples were taken from two dialysis bags. *Insets*: intensity traces as a function of time (in seconds) from which the hydrodynamic diameters were obtained, as labelled (Perez Holmberg *et al.* 2012).

The difference between the ES-SMPS and DLS sizes arises from the different concentration regimes of the samples tested by the two. Assuming a particle volume fraction based on the complete conversion of reactants yields 0.5 vol% TiO_2. For this particle concentration, if the particles are strongly interacting, the Stokes-Einstein relation may not give the best estimate of size. Another factor to consider is the effect of the solution ionic strength on the range of particle interactions. At the start of the dialysis, the ionic strength is about 200 mM, a high regime that leads to short-range interactions. About 3 hours into the dialysis, the ionic strength has been reduced to 30 mM and electrostatic repulsions become longer ranged. The effects of particle interaction on the collective diffusion coefficient yield a maximum in the DLS-determined size.[99] Considering the concentration dependence of the diffusion coefficient, the kind of DLS results obtained indicate that the nanoparticle concentration is too high in the undiluted dialyzed samples for determining a true hydrodynamic diameter.

It is interesting to note, however, that early on during the dialysis the static intensity, which generally fluctuates around a stable mean value, was found to exhibit sustained oscillations. As shown in the insets to Figure 15, the oscillations in the intensity occur with a period of about 15 seconds; superimposed on these are the much faster, small-amplitude fluctuations which serve as the basis for the measurement of the diffusion coefficient. The faster fluctuations lead to an underestimation of particle size, giving a calculated hydrodynamic diameter of only 2 nm, which is smaller than the XRD crystallite diameter of 4.2±0.1 nm.[70] Over time, the oscillations change character until the intensity signals resemble the typical fluctuations associated with the diffusion of particles. Sustained oscillations are known to occur in chemical reactions where systems are far from equilibrium.[100] Another driving factor for chemical oscillations is the solution pH,[101] which is indeed relevant in this case, as pH is increased from 0.7 to about 2.5 over a relatively short time span. The oscillatory intensity is

also said to be related to be related to precipitation reactions,[102, 103] and the oscillations detected by DLS may very well reflect the particle formation mechanism that occurs during the dialysis of the suspension.

4.3 Formation of TiO_2

The thermodynamics of formation of TiO_2 from the hydrolysis of $TiCl_4$ in the gaseous phase has been explored in earlier computational studies, using density functional theory.[71, 104] The process is described to be endothermic and the hydrolysis of $TiCl_4$ leads to the formation of the oxychloride and hydroxychloride complexes that serve as precursors to the solid phase.[71] In aqueous media, however, the reaction is much less endothermic and the energetics is different due to the larger amount of water in the system.

In non-complexing electrolytes with low solution pH, mono-nuclear complexes are formed. As shown in the speciation plots in Section 4.1, mono-nuclear hydroxy and oxychloride complexes comprise the dissolved Ti, with $TiOH^{3+}$ being the dominant complex in the precursor solution. The presence of chloride complexes in the precursor accounts for the presence of a small amount of brookite in the final synthesis product, as chloride acts as a template in the brookite formation. The presence of chloride in the coordination sphere of Ti ions orients the first steps of condensation, but the Cl^- is eventually eliminated in the oxolation reaction, where the formation of μ_3-oxo bridges between Ti octahedral results in HCl elimination and yields brookite TiO_2.[88]

The pH and pCl increases as protons and chloride ions are drawn out of the suspension by dialysis. The relationship between the measured pH and conductivity, with the assumption that H^+ and Cl^- dominate in the ionic strength, fits well with the thermodynamic prediction (Figure 8 in Paper III). This justifies the use of conductivity data to estimate chloride concentration and calculate the change in the distribution of soluble complexes and solid material formed, initially as $TiO(OH)_2$ (s). As the oxyhydroxide solid transforms into anatase, the amount of dissolved species further decreases. According to thermodynamic calculations, the growth of solid matter takes place by the incorporation of mono-nuclear complexes to existing particles, which results in a localised decrease in pH close to the solid-liquid interface as protons are released. When enough protons accumulate near the interface, the equilibrium is shifted in the opposite direction and the Ti-complexes are once again formed. Reaction 30 is a proposed description of this process.[93]

$$\left[TiO(OH)_2\right]_n + zTi(OH)_x^{(4-x)+} \underset{k_2}{\overset{k_1}{\rightleftharpoons}} \left[TiO(OH)_2\right]_{n+z} + z(4-x)H^+ \qquad [30]$$

The reversible condensation/dissolution process likely explains the oscillatory behaviour observed by DLS, with the frequency of the oscillations depending on the reaction rates. The back and forth re-equilibration proceeds until the solid to solution fraction becomes greater than 1. The oscillations are then no longer detectable and stable particles are formed. With time, the more thermodynamically stable crystalline phases are formed from the amorphous solid, further decreasing the concentration of titanium complexes. After the primary particles are formed, particle interactions facilitate growth of solid material as stable aggregates, seen in the results after about 1 week of aging.

4.4 Commentary on experimental design

Due to practical limitations, simplifications were made on the experimental design. Conductivity data gave an acceptable estimate of chloride concentration, but it still proves beneficial to experimentally determine the exact concentration of free Cl^- ions in solution. The same can be said about the determination of unprecipitated $Ti(IV)_{aq}$, by colorimetric analysis of its complexation with H_2O_2.[85, 88, 105] However, this presents a number of practical challenges, such as the inability to fully separate very small suspended particles, and the indeterminable changes to the system by sample preparation.

Chapter 5: The Diffusion of Polydisperse TiO_2 Suspensions

In which we explore the effect of particle interactions and aggregates on the collective diffusion coefficient of TiO_2 nanoparticles

The initial formation and growth of TiO_2 nanoparticles were discussed in terms of the hydrolysis and condensation mechanisms in Chapter 4. After the initially-formed titanium complexes have been precipitated into particulate matter, the next aspect for consideration would be related to the stability of the synthesized particles as the system ages. The acid-base properties of the oxide surface facilitate processes at the interface which can lead to the reconfiguration of the surface over time. Experimental findings presented in the previous chapters have shown that, in this particular system of TiO_2 particles, growth occurs by slow aggregation. One of the techniques commonly used in the study of aggregation in colloidal systems is light scattering.

Light scattering is a well-established tool in the examination of the static and dynamic properties of colloids. Model systems such as monodisperse suspensions of polystyrene spheres, silica particles, and sterically stabilised nanoparticles are often employed in the study of colloidal interactions and processes such as diffusion. As such, the information obtained from light scattering has made it possible to quantitatively understand monodisperse particle suspensions. The surfactant-free TiO_2 nanoparticles produced by hydrolytic synthesis, however, might not necessarily be considered as a model suspension. The relatively high particle charge, which provides electrostatic stabilization to the particles, implies that the effects of particle interactions are under most circumstances far from negligible. These interactions, in turn, influence the collective diffusion. The recognition of such factors is necessary in order to accurately analyse the results from light scattering measurements.

This chapter summarizes the work presented in the article, "Nonlinear Concentration Dependence of the Collective Diffusion Coefficient of TiO_2 Nanoparticle Dispersions" by Perez Holmberg *et al.*,[106] which appears as Paper II in the Appendices. Experimental results from multi-angle dynamic light scattering are shown and discussed in the context of scattering theory. A binary sphere model is also introduced as a means of understanding the behaviour of electrostatically-stabilized particles, when polydispersity affects particle interactions in the colloidal suspension.

5.1 Dynamic Light Scattering and the Diffusion Coefficient

In Chapter 2, a simple overview was presented on how particle size information is obtained from the analysis of the intensity fluctuations measured by DLS. Given that diffusion is the process being probed during DLS measurements, particle interactions and other factors that influence the collective diffusion need to be taken into account, in order to gain a full understanding of the results. Thus, it is worthwhile to explore some aspects of light scattering theory in greater detail.

5.1.1 Scattering Theory

Measured temporal variations in intensity are analysed using the intensity autocorrelation function, $g^{(2)}(q,t)$, Equation 1 in Chapter 2. A normalized, so-called field correlation function, $g^{(1)}(q,t)$, is obtained via the Siegert relation

$$g^{(2)}(q,t) = 1 + \gamma \left| g^{(1)}(q,t) \right|^2 \qquad [31]$$

where γ is an instrumental constant dependent on the geometry of detection.[107, 108] The parameter q is the modulus of the wavevector, containing the angle of detection θ and defined as: $q = 4\pi(n/\lambda_0)\sin(\theta/2)$, with n being the refractive index of the medium and λ_0 the wavelength of incident light. The normalized field correlation function is related to the normalized measured or effective structure factor[109] such that

$$g^{(1)}(q,t) = \frac{S_M(q,t)}{S_M(q)} \qquad [32]$$

where $S_M(q) = S_M(q, t \to 0)$ is the measured static structure factor.[110] Structure factors describe how positional correlations affect the scattering of incident radiation and are influenced by the interactions among particles. The structure factor differs from the form factor $\overline{f^2(q)}$, which derives from the shape, size and size distribution of the particles. In a polydisperse system, such as the TiO_2 dispersions currently being studied, interference effects embodied in the structure factor or the form factor are not readily distinguished because the interactions are coupled to size of the particles. For example, two large particles do not permit for as close an approach as two smaller particles because they come in contact with one another at larger separation distances compared to the smaller ones. As a consequence, one defines a measured or effective structure factor in analogy with a monodisperse system because the experimental analysis frequently relies on theory developed for monodisperse systems.

It proves useful to describe a polydisperse system as a discrete mixture of components. In this case, the intensity of scattered light can be expressed via partial dynamic structure factors, $S_{\alpha\beta}(q,t)$, as

$$\begin{aligned} I(q,t) &= n\overline{f^2}(q) S_M(q,t) \\ &= n \sum_{\alpha,\beta=1}^{m} (x_\alpha x_\beta)^{1/2} f_\alpha(q) f_\beta(q) S_{\alpha\beta}(q,t) \end{aligned} \qquad [33]$$

where the first equation is a product of the number density, the form factor, and the structure factor, which is of the same form as for a system of monodisperse spheres. The second equation is the actual scattering formula for a colloidal mixture; m is the number of components in the mixture, α and β denote two arbitrary species labels in the mixture, and x is the mole fraction of the specific particle type. The measured form factor of the system

$\overline{f^2}(q) = \sum_{\alpha=1}^{m} x_\alpha f_\alpha^2(q)$ can be obtained in a static scattering measurement at high dilution where $S_M(q) \approx 1$. The short-time dynamics can be extracted via a cumulant expansion, which is a way to analyze the initial decay of $g^{(1)}(q,t)$,[29] and the first cumulant Γ is seen to depend only on the measured structure factor, namely

$$\Gamma_M^{(1)}(q) = -\lim_{t\to 0} \frac{\partial}{\partial t} \ln S_M(q,t) \qquad [34]$$

As with the first cumulant in the expansion of the IACF (discussed in Chapter 2), $\Gamma_M^{(1)}$ relates to the measured diffusion coefficient. In this case, an angularly dependent short-time diffusion coefficient is defined as[111]

$$D_M(q) = \frac{\Gamma_M^{(1)}(q)}{q^2} = \frac{H_M(q)}{S_M(q)} \qquad [35]$$

where $H_M(q)$ is the so-called hydrodynamic function that, like the static structure factor, depends on particle concentration. If the hydrodynamic interactions are neglected, such that the solvent does not couple the motion of particles, $H_M(q)$ simplifies greatly. The implication of this assumption is that the concentration dependence of $D_M(q)$ is only connected to the measured structure factor. Equation 35 can then be expressed as

$$D_M(q) = \frac{1}{S_M(q)\overline{f^2}(q)} \sum_{\alpha=1}^{m} x_\alpha f_\alpha^2(q) D_\alpha^0 \qquad [36]$$

where D_α^0 is the Stokes-Einstein diffusion coefficient (Eqn. 4 in Chapter 2) for α-type spheres of radius a_α. A further simplification of the measured diffusion coefficient can be made, provided the experimental measurement is conducted at small scattering angles and/or the particle size is small, so that $q\bar{a} << 1$, where $\bar{a}$ is the mean radius. In that case, $D_M(q)$ is known as the collective diffusion coefficient. In that limit, the form amplitude $f_\alpha(q)$ is proportional to a_α^3 and is independent of q. The z-average radius, a_H, i.e. the measured hydrodynamic size obtained from DLS measurements on small particles, can now be defined as[91]

$$D_M(q) \approx \frac{k_B T}{6\pi\eta} \frac{\sum_{\alpha=1}^{m} x_\alpha a_\alpha^5}{\sum_{\alpha=1}^{m} x_\alpha a_\alpha^6} = \frac{k_B T}{6\pi\eta\, a_H} \qquad [37]$$

This formula is valid for spheres at high dilution, where $S_M(q) \to 1$ and $qa << 1$. In most cases, $q\bar{a} < 0.1$ is considered small enough.

When experiments are not made under dilute conditions, which may be the case for nanoparticles that scatter weakly, the dilution-limiting value of the collective diffusion coefficient must be obtained by the extrapolation of data for $D_M(q)$ as a function of concentration. However, additional complications may arise. In particular, the presence of aggregates or large particles, even if they are in extreme minority, may lead to an angularly dependent dilute-diffusion coefficient. The reason for this is essentially that the product of q and the large particle radius may not be small, which means that the form amplitude of the large-sphere component is not independent of angle. In addition, extrapolation of data for $D_M(q)$may be difficult due to a non-linear concentration dependence, which may appear because of complex interaction effects.

5.1.2 Experiments on TiO_2: multi-angle light scattering

The experiments performed and discussed in Article 2 were built up from the DLS characterization presented in Article 1. The hydrodynamic particle size was derived from the simple linear extrapolation of D_M^0 from a three-point dilution curve, as presented earlier (Fig. 9 in Sec. 3.2.2.3). Assuming a linear dependence of D_M with respect to TiO_2 concentration, the calculated hydrodynamic diameters (d_H) of the particles obtained from synthesis under two different temperature regimes are around 8 and 20 nm. With the intention of comparing DLS information with size data from ES-SMPS, such that the sample analysis is done on similar particle concentrations, an extended dilution series was prepared for DLS measurement. The diffusion coefficients obtained from the extended analysis are presented in Figure 16 below. For comparison, a corresponding D_M was calculated using size distribution data from ES-SMPS measurements on the smaller sized particles.

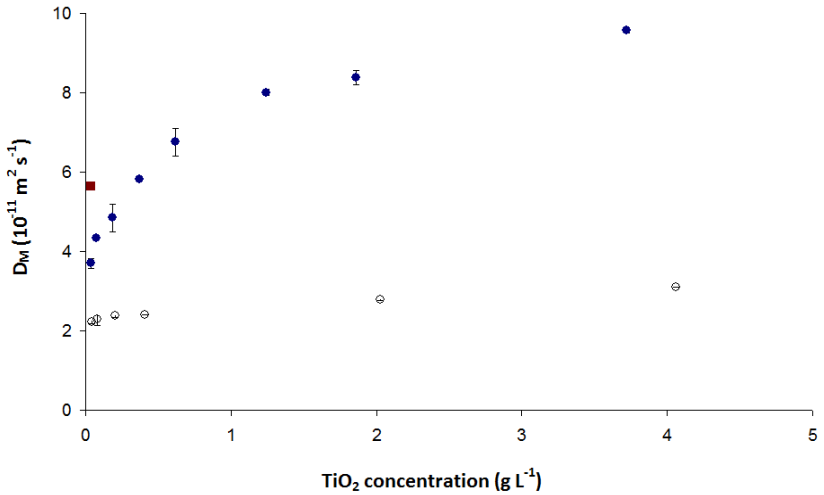

Figure 16. Collective diffusion coefficients obtained from DLS measurements on particles dialysed and aged at about 0°C and room temperature, shown as filled and open circles, respectively. The red square represents the calculated D_M from ES-SMPS size data for the smaller of the two particle suspensions (Perez Holmberg *et al.* 2011).

The results reveal a distinct difference in diffusion behaviour between the suspension containing the smaller particles and that which is comprised of larger sizes. The collective diffusion coefficient of the large particles follows a relatively linear dependence on the particle mass concentration. In contrast, the behaviour of the smaller particles deviates significantly from the expected Stokes-Einstein diffusion and the collective diffusion coefficient exhibits nonlinear concentration dependence. Considering only the higher concentrations in the measurement series, linear extrapolation of the diffusion coefficient yields a D_M^0 value that agrees more closely to the value corresponding to the ES-SMPS size. However, at the lowest concentrations, D_M decreases sharply and dips below the apparent dilute-limiting value. This difference in behaviour between the two particle systems prompted a more detailed investigation of the 8-nm particle system, considering the respective contributions of size distribution and particle interactions.

Depending on the instrumental configurations, DLS measurements are routinely made at either a 90° measurement angle or at 173°, if back scattering is employed. The analysis of the TiO_2 particles at different scattering angles is a very useful strategy because this can reveal the presence of aggregates. Large particles give the dominant contribution to the light scattering at lower angles, while the opposite is true at higher angles. The angular dependence of light scattering by TiO_2 nanoparticles is presented in Figure 17. The shift of the primary decay in the normalized intensity correlation function towards later times at lower angles, as well as the occurrence of a secondary decay, is indicative of the presence of aggregates. Centrifugation of the suspension significantly decreased the amount of suspended aggregates, removing much of the slower time component in the correlation functions at small angles.

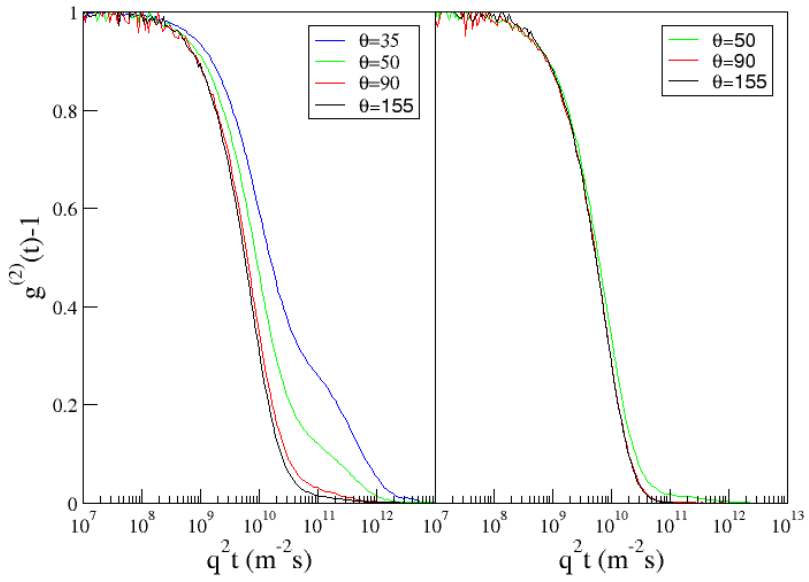

Figure 17. Angular dependence of the normalized intensity correlation function, $g^{(2)}(t)-1$ as a function of q^2t for TiO_2 nanoparticles in a 3 mM HCl solution and at a particle concentration of 1.86 g L^{-1}. The left panel shows correlation functions at various scattering angles; the right panel presents the results for the same sample, obtained after mild centrifugation, with relative centrifugal force = 2,000 x *g* (Perez Holmberg *et al.* 2011).

Recall that in Chapter 2, a simplification of the intensity correlation function for spherical particles[25, 30] was given, such that $g^{(2)}(t) \approx 1 + e^{-2q^2Dt}$. By presenting the intensity correlation functions in Figure 17 as a function of q^2t, it becomes apparent that the decay constant of the initial decay is the measured short-time diffusion coefficient, $D_M(q)$. The initial decays in the uncentrifuged sample vary with angle. Thus, it is shown that diffusion coefficients have an angular dependence, which might be caused by the polydispersity of the system.[91] In this case, the fact that mild centrifugation affects the results demonstrates that the polydispersity, in the form of larger aggregates coexisting with the nanoparticles, is indeed the reason for the diffusion coefficient acquiring an angular dependence.

The influence of particle interactions is then considered further. Suspensions of TiO_2 were prepared at different concentrations for measurement at a large angle of 173°. In order to reduce the effects of polydispersity, the suspensions were centrifuged to remove large aggregates. Consequently, the secondary, long-time decay is not evident in the intensity correlation functions presented in Figure 18. However, it is noteworthy that the decay of the correlation function is shifted to longer times as the suspension becomes more dilute. This shift is not linearly proportional to the particle concentration and reflects the nonlinear dependence of the collective diffusion coefficient, as seen earlier in Figure 16.

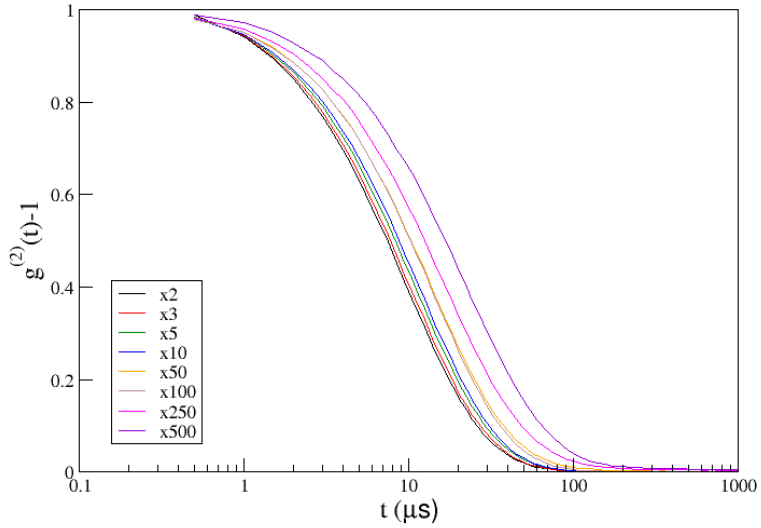

Figure 18. Normalised intensity correlation function as a function of time and TiO_2 concentration. The results are presented for suspensions diluted in 3 mM HCl (pH 2.5) from a stock sample of 18.6 g L^{-1} TiO_2. The legend shows the different dilution factors used in the measurements (Perez Holmberg *et al.* 2011).

5.2 The occurrence of nonlinear behaviour in colloidal systems

Transport coefficients of systems containing particles interacting with short-range interactions are found to exhibit a linear dependence on concentration at sufficiently low concentrations [112, 113]. For longer-range interactions, such as electrostatic interactions, this may not be the case. Low ionic strengths in the electrolyte environment provide for a Debye screening length ($1/\kappa$) that not only is large but increases upon lowering the particle concentration. This effect is caused by counterions, the concentration of which is directly

related to the particle concentration. Higher ionic strengths lead to stronger screening and short-range interactions. In those cases the concentration of added electrolyte is far greater than that of the counterions and a linear concentration dependence is expected at low particle concentrations.

Theoretical studies that take proper account of hydrodynamic interactions, as well as experimental investigations (DLS and sedimentation measurements), have shown how transport coefficients acquire a non-linear dependence on concentration at low volume fractions.[114, 115] Nägele et al. have theoretically demonstrated that the sedimentation velocity (U) in dilute, low-salinity suspensions of strongly charged colloids follow a non-linear volume fraction (ϕ) dependence of the form:[115]

$$\frac{U}{U_0} = 1 - p\phi^{1/3} \qquad [38]$$

where p is a charge-independent parameter and U_0 is the single-sphere sedimentation velocity. This nonlinearity persists even for the case of very weakly charged particles in dilute suspension, and assuming an ionic strength that is mainly due to counter ions. Sedimentation velocity follows a $\phi^{1/2}$-dependence in this type of system.[115-117] These relationships were obtained by using an approximate integral equation theory for the radial distribution function, $g(r)$. The same approach has been used to determine exponents in similar expressions for rotational and translational self-diffusion coefficients.[118, 119]

The deceleration of diffusion and sedimentation in charged systems, as a consequence of particle interactions, has been experimentally studied for various materials. Polystyrene and silica suspensions, as well as charged protein solutions have been examined by light scattering,[111, 120] small-angle x-ray scattering,[121] and sedimentation experiments.[114] The influence of particle interactions in these systems have been explained in terms of the effective pair potentials between two identical spheres,[114] representing charged monodisperse systems, as well as between spheres of different sizes, taking intrinsic polydispersity into account.[111]

A similar approach has been employed in the explanation of the collective diffusion behaviour of the synthesized TiO_2 nanoparticles, taking into account the specific aggregate structure in this system.

5.3 Binary Sphere model

Given the rather high ionic strength in the TiO_2 system under study, it seems unlikely that counter ions would dominate the screening. The non-linear concentration dependence of the collective diffusion coefficient observed in Figure 16 probably has another cause than a screening length dependent on particle concentration. By adopting a simple two-component system it can be shown that polydispersity in particle size can in some cases lead to non-linearities in the concentration dependence of the collective diffusion coefficient

A system comprised of two differently sized spheres is taken as a representation of the TiO_2 suspension and is illustrated in Figure 19. To keep matters as simple as possible, a number of assumptions were taken in the model. First, the porous structure of the aggregate brings about a weaker degree of hydrodynamic interaction compared to a compact, solid sphere of comparable size.[122] Second, the surface charge of the large spheres is set to zero because of the expectation that the penetrating counterions are strongly screening the surface charges in the aggregate.[123] Lastly, a further assumption is made that the two types of spheres are homogeneous.

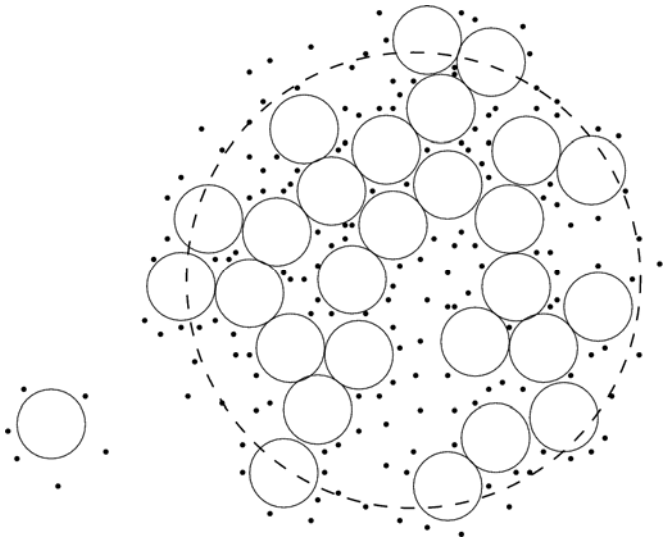

Figure 19. Binary sphere model representative of the suspension of synthesized TiO_2 nanoparticles, comprised of small, charged colloidal particles (left) and their aggregates (right). Counterions are presented as points. In the simplified model, the aggregates are treated as neutral hard spheres of the size delineated by the dashed outline (Perez Holmberg *et al.* 2011).

The spheres are assumed to be interacting through a screened Coulomb potential[124] as

$$\begin{aligned} u_{\alpha\beta}(r)/k_BT &= \infty && \text{when } r < a_\alpha + a_\beta \\ &= L_B Z_\alpha Z_\beta \left(\frac{e^{\kappa a_\alpha}}{1+\kappa a_\alpha}\right)\left(\frac{e^{\kappa a_\beta}}{1+\kappa a_\beta}\right)\frac{e^{-\kappa r}}{r} && \text{when } a_\alpha + a_\beta < r \end{aligned} \qquad [39]$$

which contains the Bjerrum length, $L_B = e_0^2/4\pi\varepsilon_0\varepsilon_r k_B T$, the separation distance at which the Coulombic energy is comparable to the thermal energy, $k_B T$.[114] The parameter Z_α is the number of surface charges on particles of radius a_α belonging to type α, and κ^{-1} is the Debye screening length given by

$$\kappa^2 = 4\pi L_B \sum_{\alpha=1}^{m} n_\alpha |Z_\alpha| + \kappa_{salt}^2 \qquad [40]$$

where n_α is the number concentration of type-α colloidal particles. The Debye length is a measure of the thickness of the electrical double layer and is dependent the concentration of

particles via the counterions. The second term in the equation accounts for the contribution from added monovalent salt, such that $\kappa_{salt}^2 = 8\pi L_B n_{salt}$, where n_{salt} is the bulk number density of the salt. For the TiO_2 suspensions in this study, the Cl^- environment is a consequence of the hydrolytic synthesis from $TiCl_4$ and the subsequent dialysis of the precursor solution to pH 2.5, which brings the Cl^- concentration to about 3 mM. In the DLS experiments, the particles are diluted in pH 2.5 HCl, thus maintaining the ionic strength while altering the particle concentration.

Recall Equation 36 in Section 5.1.1, wherein the measured diffusion coefficient $D_M(q)$ is expressed as a function of $S_M(q)$, while neglecting the contribution of hydrodynamic interactions:

$$D_M(q) = \frac{1}{S_M(q)\overline{f^2}(q)} \sum_{\alpha=1}^{m} x_\alpha f_\alpha^2(q) D_\alpha^0 \qquad [36]$$

The measured structure factor is composed of several contributing partial structure factors, integrated into the total $S_M(q)$ term, using the hypernetted chain (HNC) theory.[125, 126] The HNC theory provides exact structural predictions in dilute systems and is otherwise expected to give accurate predictions for systems of particles with long-range interactions. The form amplitude, $f_\alpha(q)$, was calculated in terms of homogeneous spheres and is described as

$$f_\alpha(q) = \frac{4\pi \Delta n_\alpha}{q^3} (\sin qa_\alpha - qa_\alpha \cos qa_\alpha) \qquad [41]$$

where Δn_α is the difference in the refractive index between type-α particles and the surrounding solvent.

Calculations on a colloidal system containing 10 nm particles with 25 charges, and 100-nm sized aggregates yielded $D_M(q)$ curves that qualitatively reflected the nonlinear behaviour observed in the DLS experiments. As with the experimental results, the deviation of $D_M(q)$ from the small-sphere Stokes-Einstein value occurred as the system became more dilute. The calculated $D_M(q)$ for three scattering angles, θ = 30, 90, and 173° are shown in Figure 20. For this specific case, the concentration ratio between the two differently-sized spherical components was set at 1 large particle per 1 million small particles, corresponding to the volume fractions $\phi_{large} = 10^{-3} \times \phi_{small}$. Take note that this particle concentration ratio is maintained in all subsequent analyses in this section. In the absence of aggregates, the diffusion coefficient exhibits an apparent linear relationship with particle concentration, the behaviour expected for suspensions of monodisperse particles interacting via short-range interactions.[99, 112, 113]

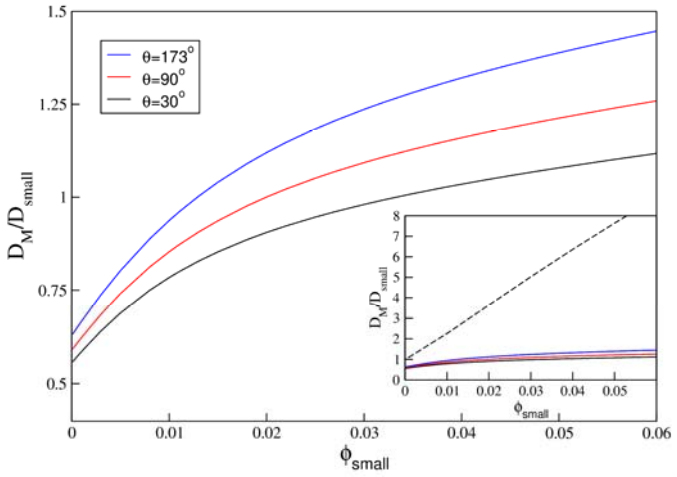

Figure 20. Normalised measured diffusion coefficient, as a function of the volume fraction of small particles, for three different scattering angles. The volume ratio of small to large particles is constant, such that $\phi_{large} = 10^{-3} \times \phi_{small}$. The inset shows the linear concentration dependence that arises from the removal of the large-sphere component from the colloidal system (Perez Holmberg *et al.* 2011).

Whereas the presence of the large sphere component, even though its concentration is very low, explains the reason for the collective diffusion coefficient tending to a value lower than the small-sphere Stokes-Einstein diffusion coefficient in the dilute limit, the non-linear concentration dependence originates from complex interactions. These interactions lead to correlations, which can be extracted from the model. Figure 21 shows the small-small (A), small-large (B) and large-large (C) radial distribution functions for a number of different concentrations as a function of center-center separation distance. These functions were obtained using the hypernetted chain approximation.[125, 126] Radial distribution functions describe the likelihood of finding particles at a distance r, given that the particle resides at $r = 0$.

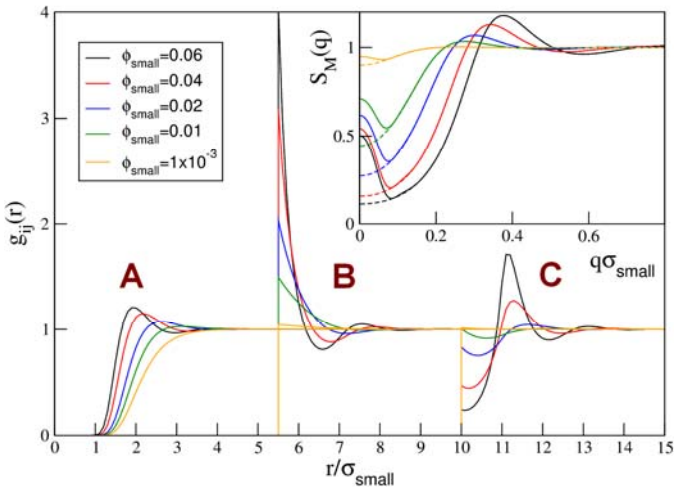

Figure 21. Radial distribution functions as a function of separation distance *r* and volume fraction of the small spheres: A) small-small $g_{ij}(r)$, B) small-large $g_{ij}(r)$, C) large-large $g_{ij}(r)$. *Inset*: corresponding measured structure factors in terms of wavevector *q* and the same volume fractions, with the dashed lines showing results in the absence of large spheres (Perez Holmberg *et al.* 2011).

The small-small $g(r)$ functions show that they are excluded from one another at short distances as expected for a screened-Coulomb interaction. From the sharply peaked form of the small-large radial distribution function one can conclude that the charged small spheres tend to cluster around neutral large spheres. In addition, a corresponding depletion of large spheres from the direct vicinity of other large spheres is seen from the large-large radial distribution functions being less than one near contact. As seen from the inset to Figure 21, the presence of large spheres, even at very low concentrations, has a marked effect on the measured structure factor at small *q*. The clustering behaviour observed here is similar to the halo formation seen experimentally by Lewis and co-workers[127-129] in mixtures of small charged spheres and weakly charged larger spheres. Those systems could serve as model systems for testing the binary sphere model in a more quantitative fashion.

5.4 Implications of the findings

Dynamic light scattering is a preferred method for particle sizing due to its non-invasiveness and rapid acquisition of measurement statistics. However, because the size obtained from DLS derives from the diffusion coefficient, one should be aware of the specific sample conditions that could influence transport behaviour. Particle concentration and the ionic strength of the medium are factors to consider, as these exert direct consequences on the Debye screening length. The effect of hydrodynamic interactions on diffusion cannot be disregarded at low concentrations. The particle structure is another determinant of transport behaviour. Collective diffusion is different for solid spheres compared to particles that consist of a solid core with a porous shell, as is the case with some surfactant-coated particles and particles contained within a gel structure.[39, 130] Finally, the practical aspects of sample preparation play a role. Changes in the ionic environment due to dilution in different media as well as treatments such as filtration or centrifugation, which may serve to induce or remove aggregates, affect the polydispersity of the system and hence its collective transport behaviour.

Chapter 6: Surface Charge and Interfacial Potential

In which we examine the charge properties of the oxide surface

As seen from the previous chapters, the electrostatically stabilized TiO_2 nanoparticles produced from hydrolytic synthesis are highly influenced by the electrolyte in which they are dispersed. The direct contact of the oxide surface with the dispersion medium implies that interfacial processes are central to the particles' stability and reactivity. The amount of reactive surface would depend on a number of factors, among these are particle size, as well as the number and type of active sites. Nanoparticle surfaces have a significant amount of curvature, which becomes more pronounced as the size decreases. The size dependence of surface charging thus becomes of interest in understanding the mechanisms of interfacial processes on TiO_2.

This chapter presents the theoretical and experimental investigations related to the surface charge and interfacial potential of TiO_2 nanoparticles,[131] Paper IV in the Appendices.

6.1 Surface charge on TiO_2

6.1.1 Surface complexation in aqueous medium

When TiO_2 particles are dispersed in an aqueous solution, a layer of water molecules is adsorbed on the oxide, leading to the inevitable formation of surface hydroxyl groups.[132] Depending on the pH and ionic environment of the suspension medium, the surface groups release or acquire protons. This gives rise to the acid-base properties of the oxide, as shown in Figure 22, and provides a charge on the surface.

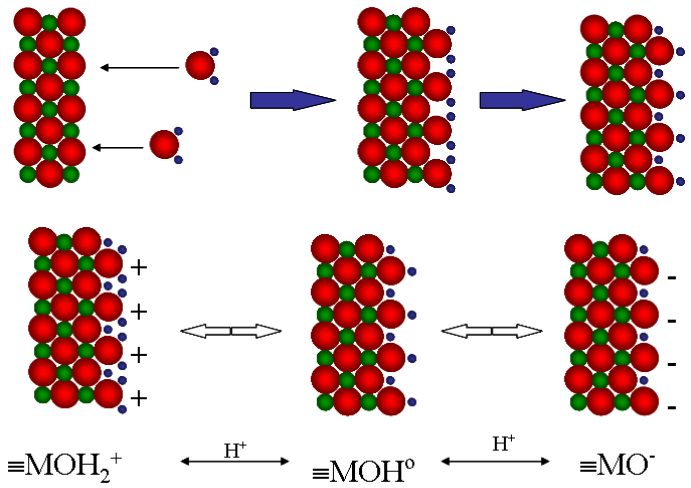

Figure 22. Charging of the metal oxide surface in water. Incoming water molecules hydroxylate the surface of the oxide. Protons associate and dissociate from the surface, depending on the pH of the dispersing medium, behaving correspondingly as an acid or base in aqueous solution (reprinted with permission from Petersson *et al.* 2009).[133]

Various system components contribute to surface charge on TiO_2. A coordinative surface charge, σ_c, arises due to proton adsorption and desorption and can also occur due to

coordination reactions of other ions with surface functional groups. To preserve electroneutrality, a diffuse layer of counterions accumulate near the particle surface and provides a dissociated charge, σ_d.[132] The oppositely charged counterions serve to screen the charge on the particle surface, the degree of which is dependent on the ionic strength of the electrolyte. A parameter which has relevance to the charge screening is the Debye length ($1/\kappa$), which describes the distance associated with the decay of the surface potential as one moves further from the particle surface and into the bulk solution.

6.1.2 Zeta potential

It is experimentally difficult to determine the potential at the particle surface with certainty. In practice, an indirect estimate of the surface potential can be obtained from the observation of the movement of a charge particle in an applied electric field. Electrophoretic mobility (μ) data from laser Doppler velocimetry (LDV), introduced in Section 2.1.2, are used to calculate zeta potential (ζ), the electrical potential at the surface of shear, located at some distance from the particle surface. This location corresponds to the electrolyte layer that moves with the particle at the same velocity.[27, 36, 134] Figure 23 illustrates the location of the zeta potential relative to the particle surface.

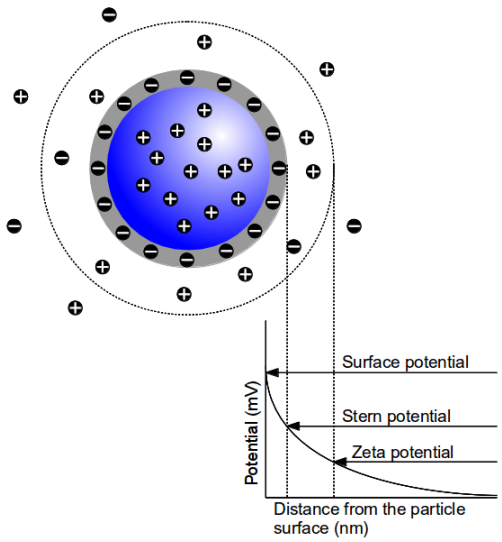

Figure 23. The relationship between the experimental zeta potential and the actual potential at the surface. The surface of shear, location at which zeta potential is determined, is shown by the dotted circle (*figure based on ref.* [135]).

The thickness of the surface of shear is dependent on the ionic strength of the electrolyte. Hence, different models for calculating zeta potential can be used, deriving from the generalized Henry's equation for electrophoretic mobility (Eqn. 9 in Sec. 2.1.2). The limiting cases for high and low ionic strengths are defined by the Hückel and Smulochowski equations, respectively.[27, 36]

$$\mu = \frac{2}{3}\frac{\varepsilon_r \varepsilon_0 \zeta}{\eta} \quad \text{when } \kappa a < 0.1 \qquad [42]$$

$$= \frac{\varepsilon_r \varepsilon_0 \zeta}{\eta} \quad \text{when } \kappa a > 100 \qquad [43]$$

where ε_r and ε_0 are the relative and vacuum permittivities, respectively, η is the viscosity of the dispersing medium, κ is the decay parameter (i.e. the reciprocal of Debye length, $1/\kappa$), and a is the particle radius. The zeta potentials in the experiments done for this study were calculated in terms of the high ionic strength Smulochowski model.

6.2 Corrected Debye-Hückel Theory of Surface Complexation

The Corrected Debye-Hückel theory of surface complexation (CDH-SC)[10] departs from the surface complexation approach based on the Gouy-Chapman double layer model.[136-138] Whereas previous analyses were pK_a-based, CDH-SC models the interaction of protons with hydroxyl surface groups by a three-dimensional harmonic oscillator model, having a specific binding energy and vibrational frequency. The CDH-SC model assumes that the TiO_2 nanoparticle is spherical and has a random distribution of a single type of reactive surface site. The hydration of the oxide surface is described by a layer of water molecules adjacent to the particle surface, denoted as the capacitor layer of width, w_c. The capacitance is related to the hydration layer by the equation[10]

$$C = \frac{\varepsilon_0 \varepsilon_s}{w_c + \frac{d}{2}} \qquad [44]$$

where ε_0 and ε_s are the vacuum and solvent permittivities, respectively. The counterion diameter, d, is a distinguishing feature of the model, as previous theoretical treatments assume counterions as dimensionless point charges.[139] The screening of a charged surface in an electrolyte solution is described by the formation of a diffuse double layer and at sufficiently high surface charge densities a condensed counter ion (IC) layer is also formed between the capacitor and diffuse layers. The components of the CDH-SC model are illustrated in Figure 24. In the IC layer counter ion size effects are included in the form of excluded volume and hole correction in the electrostatic energy. A consequence of the formation of IC-layer is that the apparent bare surface charge is reduced due to the screening by counter ions. The interaction of this effective charged surface with the bulk electrolyte is then obtained by linear response approximation. The CDH-SC theory is formulated in terms of free energy density functionals. The properties of charged particles immersed in an electrolyte solution such as the surface charge density, effective charge and thickness of the IC-layer are obtained by minimizing the free energy density functionals. A detailed description of the CDH-SC theory is given in Paper IV and key references.[131, 140, 141]

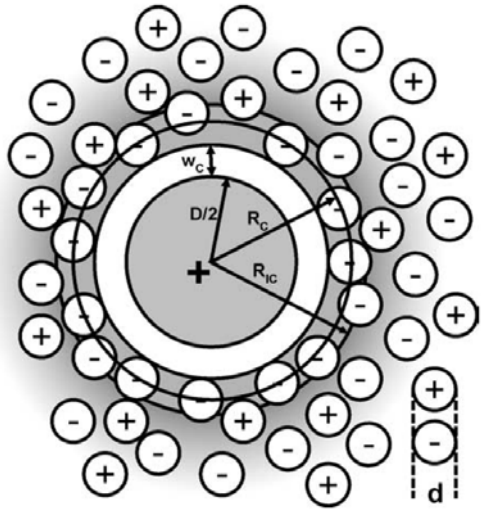

Figure 24. Schematic illustration of the CDH-SC model. The positively charged particle has a diameter, *D*, and the screening ions have a common diameter, *d*. Surface charging due to proton adsorption and desorption takes place at the particle surface ($r = D/2$). The ion-free capacitor layer is described by a thickness of w_c. The condensation of the counter ions occurs in the interval $R_c < r < R_{ic}$ (reprinted with permission from Gunnarsson *et al.* 2004).[141]

6.3 Surface charging on anatase nanoparticles based on theory

The surface charge densities calculated by the CDH-SC theory for particles of diameter 1 to 100 nm, in 0.01 M background electrolyte, are shown in Figure 25. As particle size decreases the surface charge increases, most evidently for particles with diameter < 10 nm.

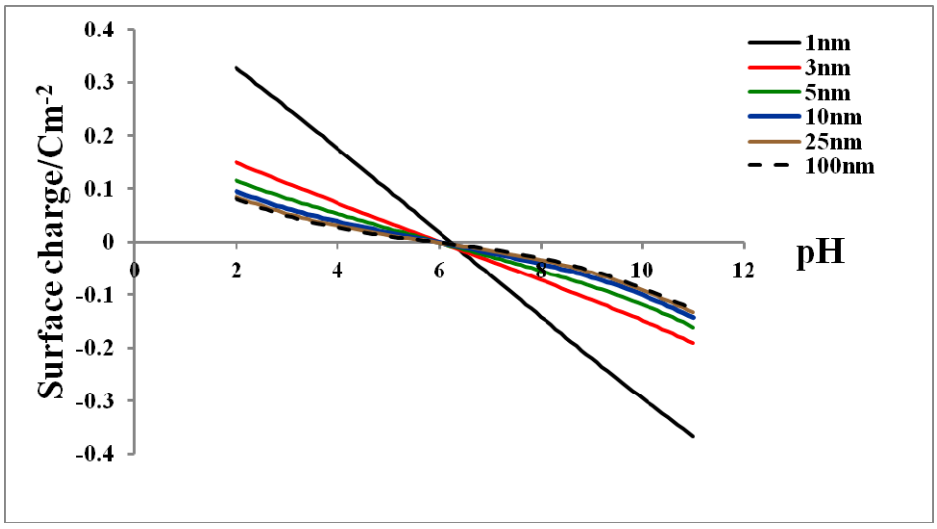

Figure 25. Size dependent surface charge densities of anatase particles as predicted by the CDH-SC theory. The electrolyte concentration is 0.01 M. The vibration frequency (*hv*) is 0.35 kJ/mol. A binding energy (μ_o) of -38 kJ/mol, and a site density of 6 sites /nm^2 were used in the theoretical calculations (Perez Holmberg *et al.* 2012).

It is noteworthy that the shapes of the surface charge versus pH curves change as the particle size decreases, i.e., the surface charge curves become straight as the particle size decreases. Straight surface charge curves indicate enhanced screening of particle surface by the counter ions. In the CDH-SC theory, this is mainly a geometrical effect where the screening atmosphere around a surface goes from a single half space to spherically surrounding form as the particle diameter goes from large to small. Enhanced screening of surface sites reduces the electrostatic repulsion among the sites, which facilitates the protonation of surface sites.

Size-dependent behaviour can be seen in terms of the pH_{pzc}, the pH at which the effective surface charge ≈ 0.[134] Shifts in the pH_{pzc} towards higher pH values for particles < 5 nm are seen for TiO_2 particles. An explanation for these results is that, as the curvature of the interface increases, the surface will desorb more protons. Consequently, the basicity will increase and the pH_{pzc} shifts to higher pH values. The CDH theory predicts the shift of only 0.5 pH units. Recall that in theory, the surface sites are assumed to have the same affinity. In reality, it is more probable that decreasing particle size brings about a change in crystal planes, which influences the reactivity of surface sites. Such heterogeneity of site reactivity will be the matter of future work.

6.4 Interfacial potential from light scattering experiments

The very small size of particles and bare surfaces make the nanoparticles aggregate more rapidly than the large particles, as a surface energy minimisation response.[86] This brings about practical limitations in the experimental analysis of size dependent surface charging. Once particles aggregate, their surface and interfacial properties are no longer of small sized particles, and instead exhibit the interfacial potential (experimentally, the zeta potential) similar to that of large, micrometer sized particles.[10] In order to determine the electrolyte concentration limits with respect to aggregation, salt titrations were performed at a fixed pH. Dispersions of surfactant-free TiO_2 nanoparticles of 10 and 22 nm diameters obtained from hydrolytic synthesis[70] were used for the experiments. At pH 2.5, the TiO_2 nanoparticles are positively charged and the counter ions are Cl^-. To maintain the same counter ions, NaCl was chosen as titrating salt. The zeta potential and hydrodynamic diameters of the particles were measured at increasing salt concentrations. Preliminary tests showed that the particle size increased rapidly after 0.2 M NaCl concentration in solution. Since the main goal of these studies was to investigate the size dependent zeta potential, the salt titrations were restricted to a maximum concentration of 0.2 M NaCl. The zeta potentials of 10 and 22 nm TiO_2 nanoparticles at various NaCl concentrations are shown in Figure 26. The zeta potential of 10 nanometer particles is lower than the 22 nm particles at all salt concentrations. These experimental results are in very good agreement with theoretical predictions. This decrease in the zeta potential was assigned to the enhanced screening of small charged particles by counter ions. In other words, a larger accumulation of counter ions was found around the smallest particles. This is perhaps the first time a clear trend in size dependent zeta potential is experimentally shown.

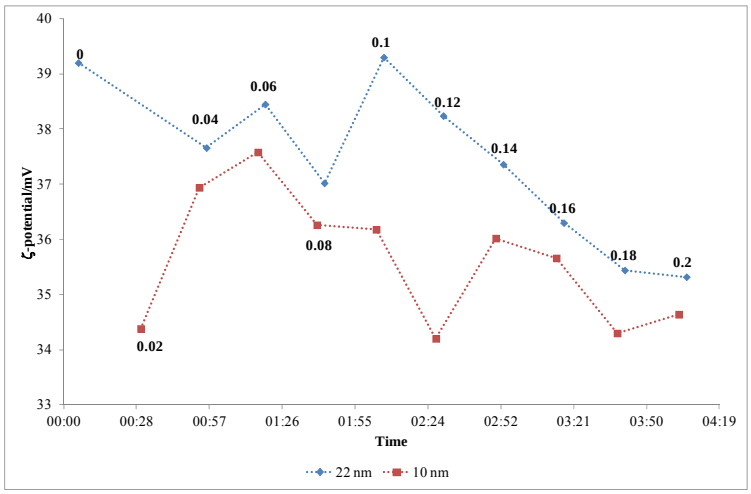

Figure 26. Zeta potentials of 10 and 22 nm TiO_2 nanoparticles at various salt concentrations. The NaCl concentration per data point is labelled accordingly (Perez Holmberg *et al.* 2012).

During the salt titrations, the pH changes as well as the hydrodynamic diameters of the particles were monitored. The results are shown in Figure 27. The pH values in colloidal dispersions of 22 nm particles were found to be higher than in dispersions of 10 nm particles. Furthermore, after an initial drift, the pH of the 10 nm particle dispersions remained fairly constant. This may be due to the enhanced screening of the charged surface by the counter ions. In the CDH-SC theory, the thickness of the condensed counter ion layer can be calculated. In 0.1 M electrolyte and at pH 2.5, the condensed ion layer around the 10 nm particle is 5.1 nm, whereas around the 22 nm particle it is 9.7 nm. Thus, the counter ions around the 10 nm particles will be tightly packed, resulting in fewer changes in the protonation state of the surface at various salt concentrations.

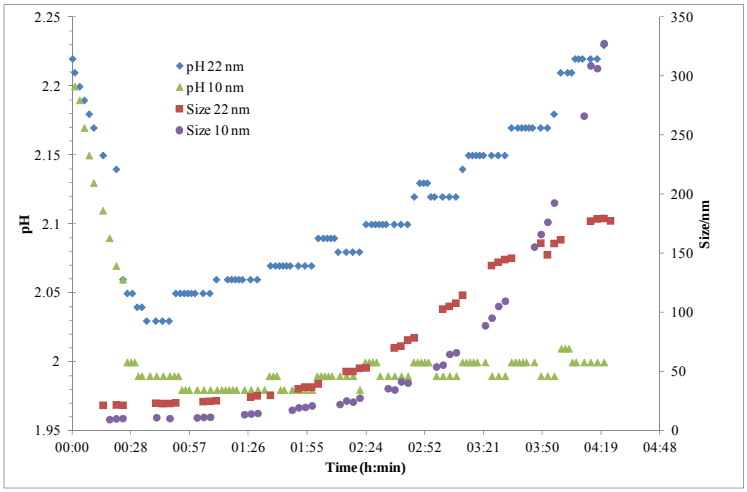

Figure 27. Variation of pH and hydrodynamic size of TiO_2 nanoparticles with time (Perez Holmberg *et al.* 2012).

The results from the NaCl experiments appear to be promising. The next step would be to optimise the electrolyte environment for the determination of surface charge at different pH, in order to validate the predictions set forth by CDH-SC theory.

Chapter 7: Applications and Implications

In which we discuss the TiO_2 nanoparticle properties that influence their application

The activity of TiO_2 nanoparticles at the oxide interface has made this material a popular choice for applications that require a catalytic semiconductor.[3] Titanium dioxide has been deposited on different substrates to create energy-generating,[6] photochromic,[142] and self-cleaning[143] surfaces. Researchers have even tested the deposition of TiO_2 on different fibres to be able to create clothes that protect us from the sun's rays[144-146] and chemical warfare agents.[147] The interaction of TiO_2 nanoparticles can differ in the context of being attached as a thin film on a substrate or as a free particle. With this in mind, two case studies are presented which have implications on the application of TiO_2 nanoparticles from a design (Paper V)[148] and biological risk (Paper VI)[149] perspective.

7.1 Surface interactions: electronic properties of TiO_2 nanoparticle films

The bioactivities of different TiO_2 films on Ti disks were tested in order to compare the suitability of each for dental implant applications. Well defined TiO_2 nanoparticles obtained from the earlier presented hydrolytic synthesis (8 and 22 nm) and commercial TiO_2 nanoparticles (Degussa P25, nominal size ~30 nm) were separately spin-coated on Ti discs with turned surface (TS, 1.1 cm diameter). The resulting TiO_2 surfaces were characterized, and then tested to determine their electrochemical properties and the consequential bioactivity by immersion in simulated body fluid (SBF).

The experimental protocol is presented in Paper V and shall not be discussed in detail here. Instead, the experimental methods are briefly presented in the context of the key findings in the study.

7.1.1 Surface characterization

X-ray diffraction measurements revealed a thin nanoparticle layer, with a weak signal in the 2θ region of the anatase (1 0 1) peak, which is the most predominant in the XRD profiles of the synthesized TiO_2. The deposited P25 film, on the other hand, has an anatase to rutile ratio of about 4:1. X-ray photoelectron spectroscopy results, obtained by analysis of the energy distribution of electrons emitted from the sample,[150] confirm that the deposited nanoparticle films are pure TiO_2 with traces of chloride. Neither signal for Ti metal nor the lower valent Ti (III) was observed.

Surface images of the different oxide surfaces are presented in Figure 28. High resolution scanning electron microscopy (SEM) shows a smooth and complete coverage, with similar morphology for the 8 and 22 nm nanoparticles (first row). Upon further investigation with atomic force microscopy (AFM), it is evident that the 22 nm particles form a surface with a greater degree of roughness, consistent with the layer being composed of larger-sized particles. The underlying substrate is not seen in the SEM and AFM images, indicating full coverage by the oxide layer.

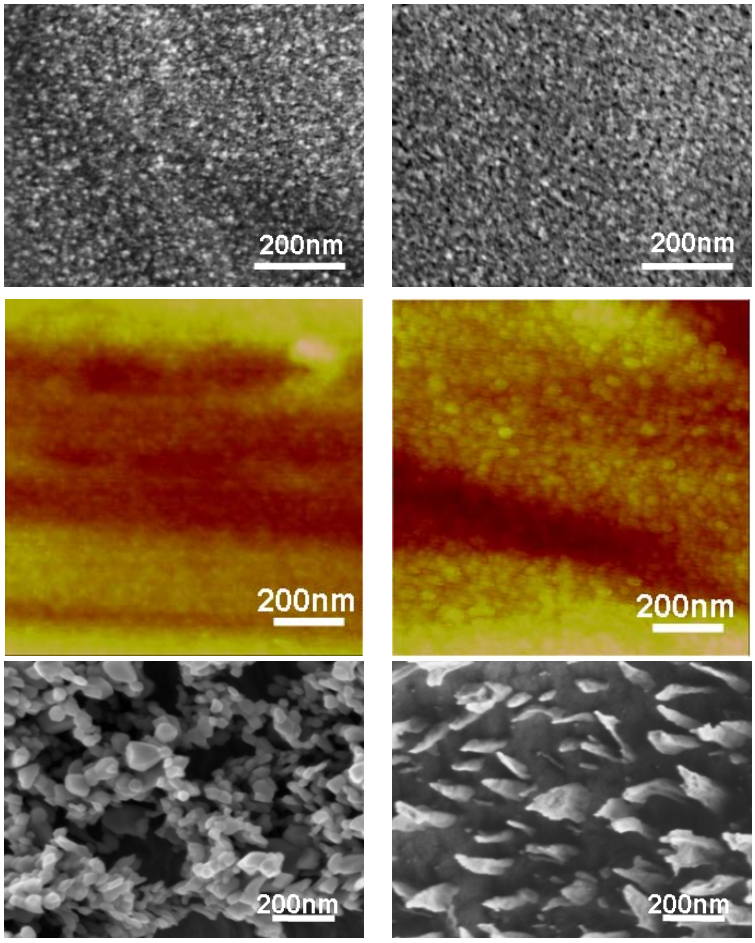

Figure 28. *From left to right*: SEM and AFM images of the TS+8nm and TS+22nm surfaces are in the top and middle rows, respectively. The lower row shows the SEM images for the TS+P25 and the surface of the acid-treated Ti disc (TS+AT1), from Löberg *et al.* 2011.

The spin-coating of P25 particles resulted in a very rough surface, due to the presence of large agglomerates in the commercial suspension. It was not possible, with available ultrasound instrumentation, to sonicate the powder suspension back to the original ~30 nm size. For comparison, the surface oxide structures formed by etching a Ti disc surface (TS+AT1) are also shown in Figure 25 (lowermost right image). In contrast to the spherical nanoparticles, these are rod-like structures that extend to a height of about 0.45 μm. In between the precipitated rods occurs a thin layer of the native oxide.

Information obtained from AFM measurements were used in the topographical analysis of the surfaces and different three-dimensional roughness parameters of biomechanical relevance were calculated.[151, 152] The average height of the oxide surface (S_a) is a height parameter commonly used to describe dental implant surfaces. The root-mean-square of the surface slope (S_{dq}) and the surface enlargement or developed interfacial area (S_{dr}) are parameters measured relative to a smooth surface.[153] The 3D roughness parameters of the different surfaces are compared to those from the native oxide on the uncoated surface (Ti) in Table 6.

Table 6. Three-dimensional surface roughness parameters from AFM analysis (Löberg *et al.* 2011)

Sample	S_a (nm)		S_{dq}		S_{dr} (%)	
	average	stdev	average	stdev	average	stdev
TS	11.6	0.67	0.26	0.09	3.51	2.06
TS+8 nm	8.34	-	0.14	-	1.05	-
TS+22 nm	10.6	1.4	0.16	0.01	1.32	0.20
TS+P25	63.3	9.2	1.73	0.26	109.3	24.5
TS+AT1	41.8	6.2	0.89	0.23	38.3	19.2

The large structures seen in the P25 and acid-etched surfaces are correspondingly reflected in the surface roughness parameters. Furthermore, it can be inferred that deposition of the synthesized TiO_2 on the Ti disc results in a smoother surface than the original, as the nanoparticles are small enough to fill the ridges on the turned surface. The S_{dq} parameter has been shown to be directly proportional to the interfacial shear strength, which is an important aspect to consider for the design of dental implants.[154, 155] The TS+P25 surface has the largest S_{dq}, giving it an advantage from the biomechanical point of view.

7.1.2 Electrochemical characterization

Semiconducting nanoparticles can have different electronic properties compared to conventional electrodes with the same chemical composition. The porous framework obtained from the deposition of oxide nanoparticles leads to a large internal surface with greater electrolyte penetration. For these systems, conduction is enhanced since the transport distance for charge carriers is small.[156]

Information on the electrochemical behaviour of a system, such as electronic properties and changes in oxidation state, can be experimentally obtained by linearly sweeping the potential over time and recording the resulting current (i) vs. potential (E) curve.[157] In cyclic voltammetry (CV), the potential is sweeped from a starting potential where no Faradaic processes occur, tracing the potential range of interest, and then reverting back to the starting potential. The magnitude and position of the peaks in a cyclic voltammogram are characteristic for a specific electrochemical reaction.

Another approach used to determine electronic properties involves the steady state perturbation of the system with an alternating signal of small magnitude. The response can be observed in terms of impedance over a range of ac frequencies. Impedance can be regarded as a complex resistance in a generalized version of Ohm's law: $\dot{E} = \dot{I}\,Z$, where $\dot{E}$ and $\dot{I}$ are phasors corresponding respectively to the voltage and current, and Z is the impedance. The impedance at an angular frequency ω is described as: $Z(\omega) = Z_{\mathrm{Re}} - jZ_{\mathrm{Im}}$, consisting of real and imaginary parts, with the factor $j = \sqrt{-1}$ being multiplied to the imaginary impedance.[157] When applied to electrochemical systems, this technique is called electrochemical impedance spectroscopy (EIS). Impedance is plotted with respect to

frequency in two ways, either as a Bode plot ($\log|Z|$ and phase angle ϕ vs. $\log\omega$) or as a Nyquist plot ($-Z_{\mathrm{Im}}$ vs. Z_{Re} for different ω).[157]

This section summarizes the results from CV and EIS experiments which demonstrate the electrochemical properties of the spin-coated TiO_2 nanoparticle films.

7.1.2.1 Cyclic voltammetry

Figure 29 presents the cyclic voltammograms obtained from measurements on surfaces with different TiO_2 nanoparticle coatings and compared with that from the uncoated substrate. The experiments were conducted using a custom-made three-electrode cell described elsewhere.[153] Measurements were done in alkaline solution (0.1 M KOH).

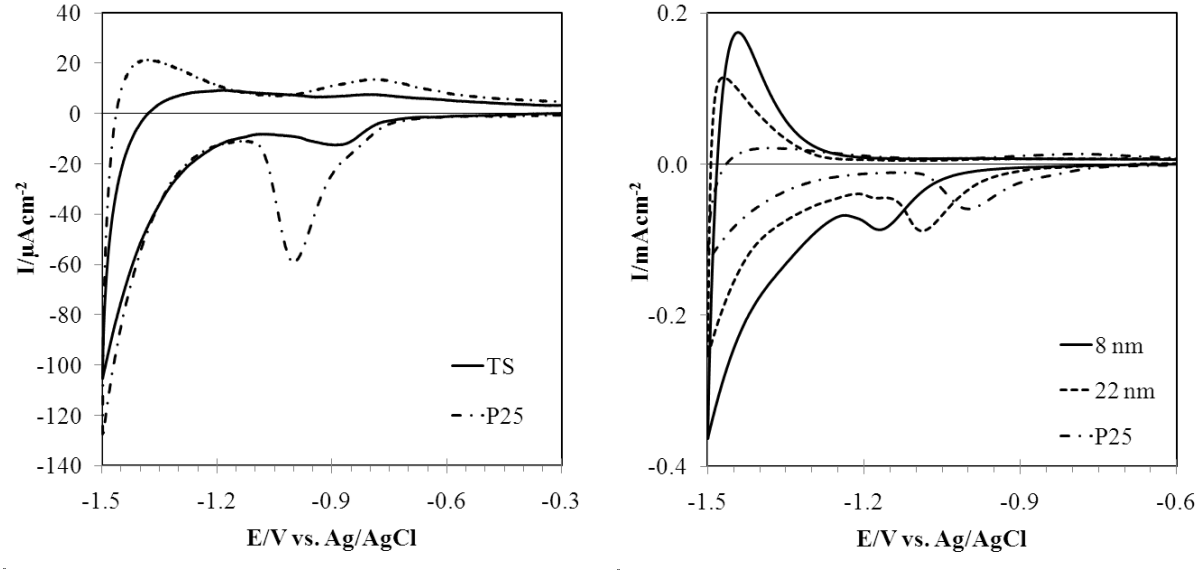

Figure 29. Cyclic voltammetry on different surfaces in deaerated 0.1 M KOH at sweep rate = 50 mVs^{-1}. *Left panel*: comparison between the uncoated turned surface and the P25-coated substrate. *Right panel*: Ti-substrate coated with synthesized 8 nm and 22 nm TiO_2 particles, and commercial P25 TiO_2 particles (Löberg *et al.* 2011).

The cyclic voltammograms obtained from the different types of surfaces indicate the occurrence of two key processes at the oxide interface:[158]

$$\overset{IV}{TiO_2} + e^- + H^+ \leftrightarrow \overset{IV}{TiO_2}\left(e^-_{CB}\right)\left(H^+\right) \qquad [45]$$

$$\overset{IV}{TiO_2} + e^- + H^+ \leftrightarrow \overset{III}{TiO_2}\left(H^+\right) \qquad [46]$$

Reaction 45 describes the charge accumulation in the conduction band, while Reaction 46 is ascribed to the charging of electronic traps located below the conduction band. A symmetrical process involving both types of charging accounts for the peaks observed at the most negative potentials. As for the signals midway through the potential range, it is primarily the reduction of Ti(IV) to Ti(III) and the associated filling of surface states below

the conduction band that are observed. The reactions presented above involve balancing of charges by proton-adsorption in acidic solution. In basic media, the adsorption of the electrolyte cation, in this case K^+, becomes equally-significant.

A native oxide layer spontaneously forms when the surface of Ti metal is exposed to air. In the cyclic voltammogram, this layer is evidenced by a reduction peak at -0.89 V and an oxidation peak at -0.81 V. In the left panel of Figure 29, the P25 reduction peak at -1.0 V shows a hint of a shoulder, and an oxidation peak corresponding to that of the native oxide. This is most likely due to the incomplete P25 layer coverage on the Ti disc. This reversibility is not observed for the surfaces completely covered by 8 nm and 22 nm particles. Lower current densities are observed for the native TiO_2 layer ($\leq 20\,\mu A\,cm^{-2}$), relative to the TiO_2 nanoparticle coatings. This can be interpreted in terms of a lesser degree of reactivity due to a lower amount of active sites. The porosity and curvature of the nanoparticle films synergistically contribute to the active surface area of the oxide layer. A shift in the peak potential is observed, depending on the fine structure of the TiO_2 coating (right panel, Figure 29), with the most negative potential observed for the 8 nm particles. This indicates that the active surface area increases with decreasing particle size. Furthermore, there is a corresponding increase in current densities for the processes observed at the most negative potentials as the particle size decreases. Based on the voltammetric response and assuming that no Faradaic processes occur, the density of states (DOS) in the band gap, as well as the electron density, can be determined. Furthermore, the peak potential (E_p) can be used to compare the active interfacial area among the different nanoparticle films. Since the exact thickness of the nanoparticle layer is not known, interfacial area of the films was normalised against the calculated interfacial area of the uncoated surface. The details of this calculation can be found in Paper V. The relative active area for each TiO_2 coated film is presented in Table 7, and compared with the surface enlargement or developed interfacial area (S_{dr}).

Table 7. Peak potentials and interfacial area of the uncoated Ti and the TiO_2 films (Löberg *et al.* 2011).

Sample	E_p	Rel. active area (A_{aa})	S_{dr} (%)
TS	- 0.89	1	3.51
TS+8 nm	- 1.16	2.65	1.05
TS+22 nm	- 1.09	1.77	1.32
TS+P25	- 1.00	1.30	109.3

The important aspect to note in this comparison is that S_{dr} represents the physical (passive) area obtained from the nanoparticle deposition and the A_{aa} is chemically active interfacial area that is created in contact with the electrolyte. While the P25 film has larger structures that contribute to the S_{dr}, its active interfacial area is only slightly larger than that of the turned Ti surface. The TS+8 nm and TS+22 nm surfaces may be smoother in appearance, but they actually yield a higher active interfacial area, the largest being that with the smallest particles. The active surface area determined from cyclic voltammetry is related to the donor density in the oxide film, which can be calculated from impedance measurements.

7.1.2.2 Electrochemical Impedance Spectroscopy

Impedance data were measured as a function of potential in the frequency range of 100 kHz to 10 mHz with an amplitude of 10 mV rms, and fitted using the equivalent circuit shown below (Figure 30).

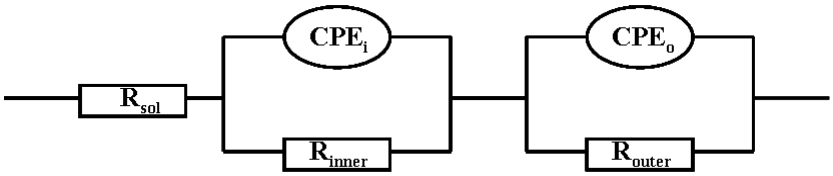

Figure 30. Equivalent circuit consisting of two time constants in series with the solution resistance, R_{sol}. Each time constant consists of a constant phase element (CPE) in parallel with a resistance related to the oxide.

In the case of a porous oxide, where the electrolyte can penetrate most of the layer, the distribution of time constants occurs laterally due to the porosity of the surface and the solution resistance is incorporated in the calculations.[159, 160] The effective capacitance (C), which is used to estimate the electric properties of the TiO_2 layer, and the space charge capacitance (C_{sc}), an important parameter for semiconductors, are calculated respectively by the following equations:

$$C = \left[Q \left(\frac{1}{R_{sol}} + \frac{1}{R_{film}} \right)^{\alpha - 1} \right]^{\frac{1}{\alpha}} \qquad [47]$$

$$\frac{1}{C_{sc}^2} = \left(\frac{2}{\varepsilon_r \varepsilon_0 e N_d} \right) \left(E - E_{fb} - \frac{kT}{e} \right) \qquad [48]$$

In Equation 47, R_{film} is related to the oxide film resistance and α is the dispersion factor for the CPE.[161] Equation 48, also known as the Mott-Schottky relation, incorporates the number of charge carriers (N_d), the applied potential (E), and the flat band potential (E_{fb}). The parameters ε_r, ε_0, and e are the relative and vacuum permittivities, and the charge of the electron, respectively. The flat band potential is the potential at which the Fermi energy corresponds to that of the redox potential; there is no charge transfer and hence, no band bending.[162] The double layer capacitance is assumed to be larger than the space charge capacitance, and the latter is therefore dominating.

The Mott-Schottky plots for the different nanoparticle surfaces are shown in the left panel of Figure 31. The behaviour of the TS+8 nm and TS+22 nm layers is the same and a single plot representing the two surfaces is presented. All the surfaces exhibit linear behaviour, except in the region of the flat band potential, where non-linearity occurs. A change in the slope (containing N_d) is observed at the most positive potentials for the TS+P25 surface. The number of charge carriers is plotted with respect to potential in the right panel of Figure 31.

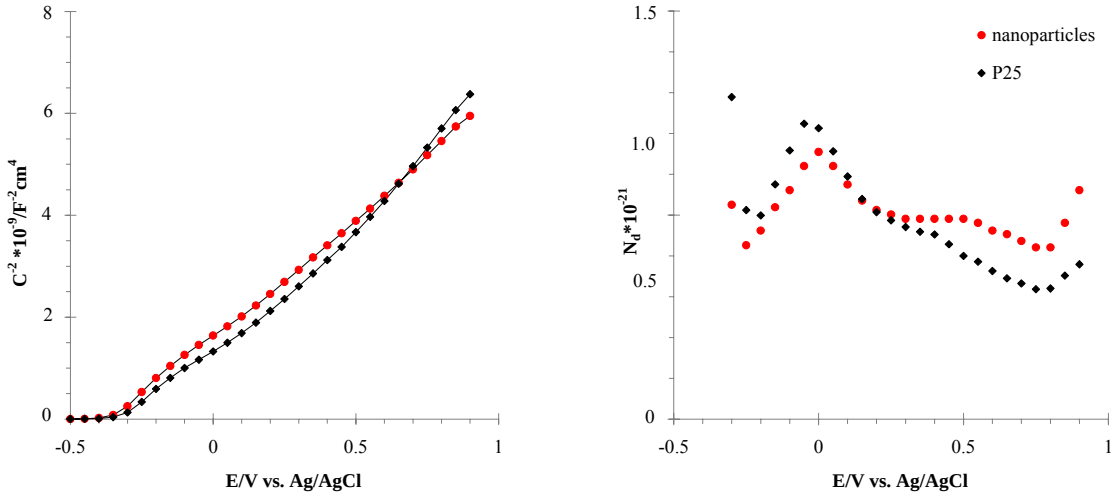

Figure 31. Mott-Schottky analysis of the TiO_2 nanoparticle films. *Left panel*: Mott-Schottky plots for the TS+8 nm and TS+22 nm surfaces (red circles) and the P25 surface (black diamonds). *Right panel*: the number of charge carriers calculated from the slope of the Mott-Schottky plot (Löberg, *et al.* 2011).

The flat band potentials were similar for the surfaces, -0.30 V and -0.35 V for the synthesized TiO_2 and P25 respectively, and are in good agreement with previously reported values.[163] For the surface with 8 nm particles, the maximum in the density of states occurs at higher energies than E_{fb}. For the other surfaces, the maximum is close to the E_{fb} (TS+22 nm) or at positive potentials relative to the E_{fb} (TS and Ti+P25). The location of these energy bands is relevant for the adsorption of bioactive compounds and the ability of the surface to function *in-vivo*.

7.1.3 Simulated body fluid (SBF) tests

An important aspect to consider in the design of TiO_2 surfaces for dental implant applications is its biocompatibility which relates, for example, to the induced cellular response, the adsorption of proteins, and the ability of the material to strongly bond with the receiving matrix.[153] The formation of apatite ($Ca_5(PO_4)_3(F,Cl,OH)$), a major component in tooth enamel and bone, is thus an important process to investigate on the different nanoparticle-coated surfaces. This was done by the immersion of the samples in simulated body fluid (SBF), which is of similar composition as human blood plasma.[164] An earlier apatite nucleation was observed by energy-dispersive x-ray spectroscopy (EDX) on the nanoparticle coated surfaces, at least three times greater coverage than the uncoated turned surface after the first 12 hours. Early nucleation of apatite crystals has been reported for surfaces with anatase structure compared to those having amorphous or rutile structure.[165-167] The more rapid nucleation of the predominantly anatase particles[70, 168] is not surprising in this case.

Images of the different surfaces after 1-week immersion in SBF are shown in Figure 32. Fractured apatite layers were observed for all surfaces, except for TS+P25. These fractures have been suggested to be caused by drying shrinkage[165, 169] or alternatively, due to stresses on the apatite layer brought about by interaction between different nuclei during three-dimensional growth.[166, 170]

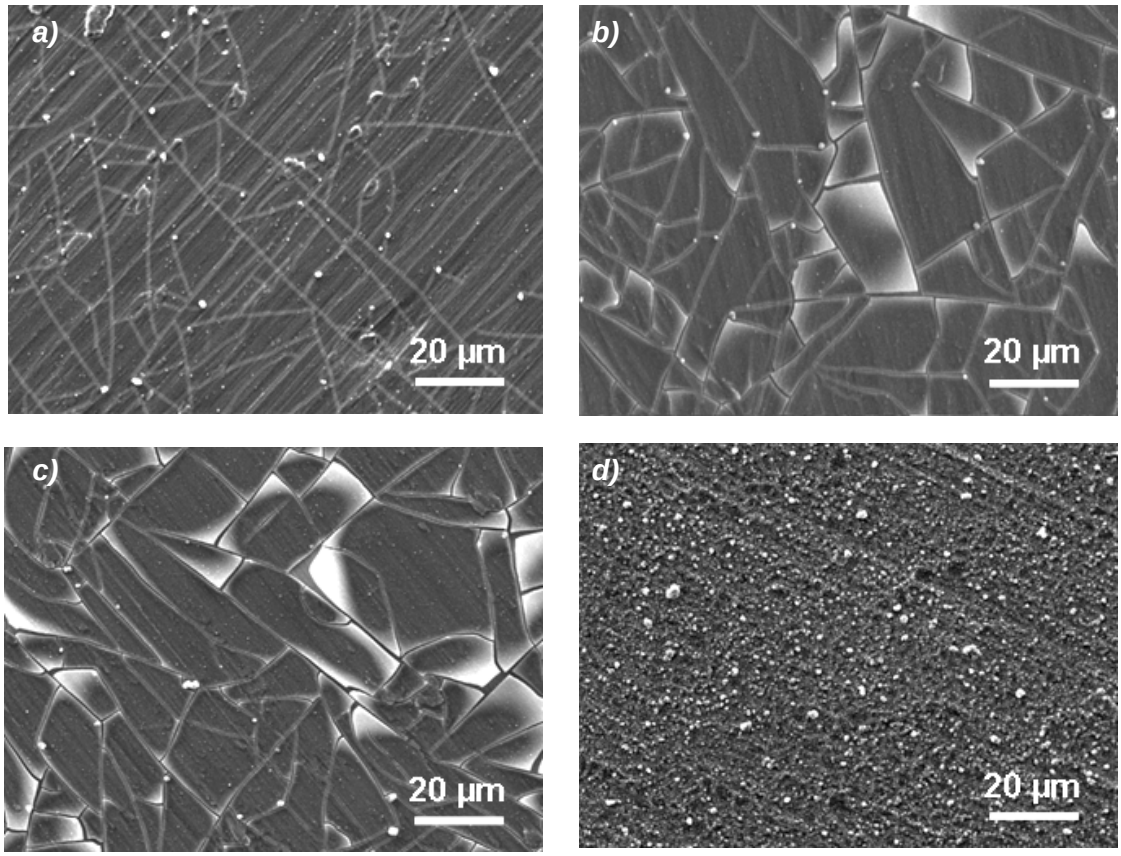

Figure 32. SEM images of the samples after 1-week immersion in SBF: a) uncoated turned surface (TS), b) TS+8 nm, c) TS+22 nm, d) TS+P25 (Löberg *et al.* 2011).

The apatite layers on the TS+8 nm and TS+22 nm surfaces appear to be detaching from the underlying surface. Results from energy-dispersive x-ray spectroscopy (EDX) within the cracks show Ca and P to be present in only trace amounts. Previous studies have reported this detachment as a result of weak interactions with the underlying substrate and the absence of surface roughness.[171, 172] Analysis of results from EDX and grazing incidence x-ray diffraction (GI-XRD) reveal that for all four surfaces, there is a high coverage of amorphous apatite after 1 week of immersion. Homogeneous growth from SBF solution has been said to start with the formation of an amorphous phase with subsequent formation of small apatite crystals.[173]

7.1.3 Commentary on nanoparticle film structure and dental implant applications

The design of an ideal oxide surface for Ti dental implants is not a straightforward process and there are trade-offs when deciding to either focus on the development of a rough surface, or a smoother porous layer. Rougher surfaces tend to have greater shear strength and facilitate the growth of thick apatite layers. On the other hand, porous layers with larger active interfacial areas could prove to be beneficial for the adsorption of redox-active proteins, which also contributes to biocompatibility. With regards to the types of surfaces presented in this study, the development of TiO_2 nanoparticle deposition methods that maximize the active surface area while allowing for high structures that introduce roughness might be the best, albeit challenging, approach.

7.2. Free particle effects: TiO_2 nanoparticles and lipid membranes

As more properties of TiO_2 nanoparticles become understood, greater possibilities for designing the material towards a wide range of applications emerge. An increase in the use of TiO_2 nanoparticles in consumer products, cosmetics[174, 175] and clothing[144-146] for example, means increased exposure, possibly on a daily basis. It thus makes sense to investigate the fundamental aspects of TiO_2 nanoparticle interaction on biological systems. The bioactivity of nanostructured TiO_2 films was explored in the previous section. This section examines the interfacial interaction between TiO_2 nanoparticles and lipid membranes, which finds relevance in understanding its biocompatibility and potential toxicity.

The experimental analysis of TiO_2-lipid interactions was conducted with the use of two complementary techniques: quartz crystal microbalance with dissipation (QCM-D) and atomic force microscopy. The QCM-D technique makes use of frequency changes on a piezoelectric quartz crystal resonator[176] to measure changes in mass per unit area. The dissipation monitoring function of QCM-D instrumentation makes it possible to record the energy-dissipation of the lipid film, which is related to its viscoelastic properties.[177] The dissipation factor (D) is related to the resonant frequency (f) by the following:[178]

$$D = \frac{1}{\pi f \tau} \qquad [49]$$

where τ is the decay time constant of the crystal resonator voltage after the power has been switched off. Measurements of f and D are made by periodically disconnecting the oscillating crystal from a driving circuit. The decay of the oscillation is recorded by an oscilloscope and transferred to a computer which ultimately calculates f and D from fitted data.[178]

The interaction experiments were done on supported lipid bilayers (SLB), which are widely accepted model systems that mimic the natural cell membrane. Natural lipids self-assemble into an amphiphilic bilayer that regulates the substances that spontaneously enter and exit the cell.[177, 179] As described in Paper VI,[149] supported lipid membranes of different compositions were formed on SiO_2 supports, via the adsorption – spontaneous rupture – fusion process of adsorbed liposomes.[180] Different compositions of negatively charged (POPG)[a] and positively charged (POPC/POEPC)[b] liposomes (diameter ≈ 80 nm) were used. To reduce the electrostatic repulsion between the negatively charged surface and negatively charged liposomes, Ca^{2+} ions were added during the film formation process. The presence of Ca^{2+} in the system would later prove to be a vital factor in the TiO_2-induced effects on the integrity of the lipid membrane.

The positively charged TiO_2 nanoparticles obtained from hydrolytic synthesis were rapidly treated with NaOH in order to reverse the particle charge before dispersion in 10 mM tris(hydroxymethyl)aminomethane (TRIS), a commonly used buffer in biochemical experiments. This resulted in the aggregation of small particles to an average diameter close

[a] POPG = 1-palmitoyl-2-oleoyl-sn-glycero-3-phospho-(1'-rac-glycerol)
[b] POPC = 1-palmitoyl-2-oleoyl-sn-glycero-3-phosphocholine
POEPC = 1-palmitoyl-2-oleoyl-sn-glycero-3-ethylphosphocholine

to 60 nm at pH 8. The size and zeta potential of TiO_2 and liposomes used in the experiments are shown in Table 8.

Table 8. Size and zeta potential of TiO_2 and liposomes from light scattering measurements (Zhao et al. 2012).

Sample (dispersion in 10 mM TRIS)	Diameter (nm)	Polydispersity index	Zeta potential (mV)
TiO_2 nanoparticles	57±1	0.2	-27±2
POPC	84±3	0.1	-2±1
POPC/POEPC 1:1	94±1		+59±1
POPC/POPG 1:1	82±1		-47±1
POPC/POPG 1:1 (Tris-$CaCl_2$ buffer, 1 mM $CaCl_2$)	79±1		-27±2
POPC/POPG 1:1 (Tris-$CaCl_2$ buffer, 2 mM $CaCl_2$)	77±2		-22±1
POPC/POPG 1:1 (Tris-$CaCl_2$ buffer, 4 mM $CaCl_2$)	80±1		-19±1
POPC/POPG 1:1 (Tris-$CaCl_2$ buffer, 8 mM $CaCl_2$)	185±10	0.5	-14±1

Experimental QCM-D data for the interaction of TiO_2 with different types of lipid membranes are presented in Figure 33. When negative TiO_2 nanoparticles were introduced to the positively charged bilayer (POPC/POEPC), the frequency shift (Δf) decreased, corresponding to a mass uptake, while the dissipation shift (ΔD) increased, which meant the formation of a more dissipative layer. These shifts occurred rapidly and stayed constant after removal of excess TiO_2/TRIS suspension by rinsing through with clean TRIS buffer, indicating that the particle adsorption is irreversible on the time scale of the experiments. The amount of adsorbed TiO_2 is expected to scale with the net charge of the lipid bilayer. Further tests on the positive bilayers with larger particles (~200 nm, -34 mV) showed higher dissipation shifts than those obtained from smaller-sized particles, owing in part to the higher negative charge on TiO_2.

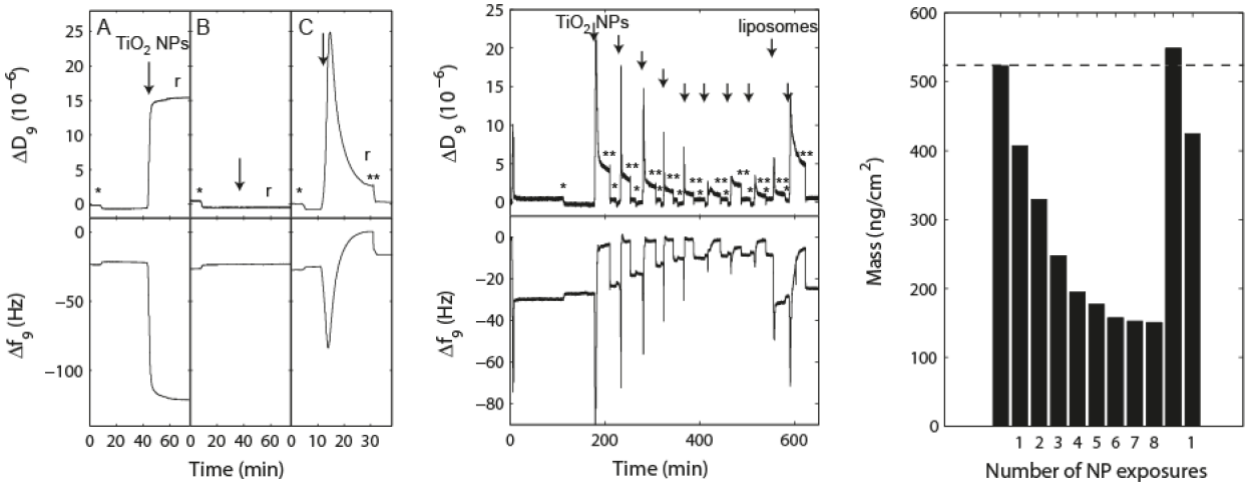

Figure 33. QCM-D frequency (Δf) and dissipation shifts (ΔD) obtained upon addition of TiO_2 nanoparticles (arrows) to supported lipid bilayers of different composition and charge. *Left panel*: (A)

POPC/POEPC 1:1 (positive), (B) POPC (neutral), (C) POPC/POPG 1:1 (negative). Rinsing (r) with TRIS buffer was done after every addition. *Centre panel*: system behaviour upon repeated addition of TiO_2 to POPC/POPG 1:1 and buffer changes from TRIS (*) to TRIS-NaCl-$CaCl_2$ (**). *Right panel*: Lipid mass on the QCM-D sensor surface, with respect to the number of TiO_2 nanoparticle exposures. The unnumbered bars represent the starting lipid mass before TiO_2 addition (reprinted with permission from Zhao *et al.* 2012).

No adsorption of TiO_2 was observed in the case of the weakly negatively charged lipid membranes. However, TiO_2 nanoparticles interact in a different way to the strongly negative POPG-containing membranes, shown in Figure 33 (C). The frequency shift first decreased (mass uptake due to adsorption), increased (mass loss), then gradually reached zero. The dissipation shift showed a correspondingly opposite behaviour. The (**) marks in Figure 33 denote the rinsing of the membrane with TRIS-NaCl-$CaCl_2$ buffer, which is standard protocol to compensate for large dissipation shifts in POPG membranes.[181] Taking the buffer effect into consideration, the net result of the TiO_2-POPC/POPG interaction is a small decrease in mass. Changes in mass can be calculated from the measured shifts in frequency using the Sauerbrey equation.[177]

$$\Delta m = -C_{QCM}\frac{\Delta f_n}{n} \qquad [50]$$

In the equation, Δf_n is the change in the resonance frequency at the *n*th harmonic, and the mass sensitivity constant, C_{QCM} = 17.7 ng cm^{-2} Hz^{-1} at f = 5 MHz.

Strangely enough, this mass loss is reproducible and cumulative with repeated TiO_2 additions and Ca^{2+}-buffer rinses, as seen in the right panel of Figure 33. The lipid mass is recovered by the introduction of new POPC/POPG liposomes to repair the membrane, which is promptly disrupted again when TiO_2 is added.

The loss of mass resulting from TiO_2-induced membrane rupture is confirmed by AFM, and an image of a hole in the POPC/POPG membrane is shown in Figure 34. A mechanism for the Ca^{2+}-mediated lipid detachment by TiO_2 nanoparticles is proposed. During the bilayer formation process, which occurs in the Ca^{2+}-rich buffer, the Ca^{2+} ions are attracted to the negatively charged SiO_2 surface and accumulate in the region between the substrate and negatively-charged POPG lipids. However, when TiO_2 nanoparticles are introduced, the Ca^{2+} migrates away from the substrate, as the ions have a higher affinity for TiO_2 compared to SiO_2. This hypothesis is made on the basis of the higher Ca^{2+} complexation constants for TiO_2: pKa 0.58-1.58 for TiO_2 [182] compared to pKa 6.9 for SiO_2.[183] At the same time, the divalent Ca^{2+} ions might still strongly bind to the POPG lipid head.[184] In this scenario, TiO_2 nanoparticles act as Ca^{2+} scavengers, pulling away the Ca^{2+} still bound to the phospholipid head, resulting in the rupture of the bilayer structure. Similar behaviour was observed for the membrane when EDTA (which strongly complexes with Ca^{2+}) is added instead of TiO_2, supporting this scenario. The QCM-D data for the EDTA tests are presented in the supporting information of Paper VI.

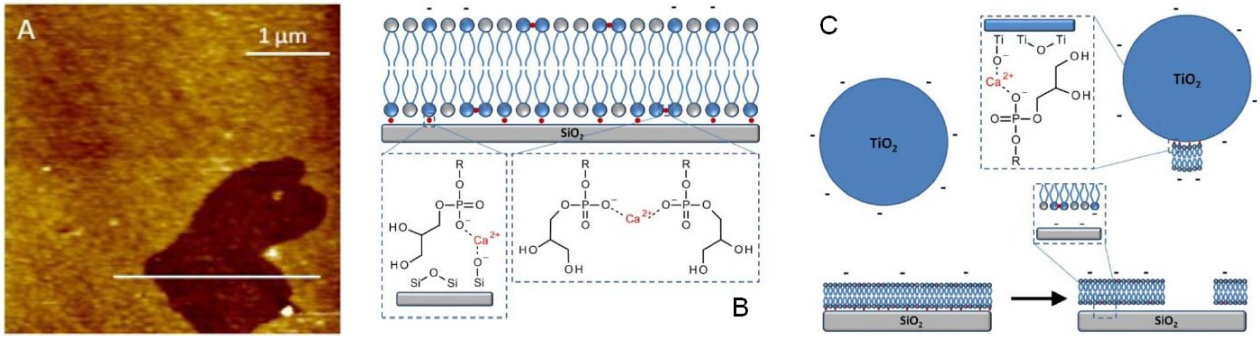

Figure 34. A: AFM image of a µm-sized hole in the POPC/POPG lipid bilayer. **B**: a plausible structure where POPG lipids in the membrane are preferentially oriented towards the substrate, with Ca^{2+} ions bound to the interface between the membrane and the SiO_2 substrate. **C**: in the presence of TiO_2 nanoparticles, Ca^{2+} accumulate at the lipid-TiO_2 interface, leading to the removal of Ca^{2+} ions, as well as whole membrane patches, from the substrate (reprinted with permission from Zhao et al. 2012).

The synergistic effect of Ca^{2+} and TiO_2 on lipid bilayers is indeed an aspect of concern, as calcium is an element that is ubiquitous in the natural environment[1] and Ca^{2+} ions play a role in several metabolic processes.[185] The TiO_2-lipid interactions in this study are, of course, based on a model system where the oxide surface is directly accessible to lipids and Ca^{2+} ions; functionalized TiO_2 with features that dampen surface charge may interact differently with the lipid bilayer. Nevertheless, the possibility of physical damage to cell membranes by TiO_2 nanoparticles is worth considering, as this facilitates the entry of TiO_2 into the cell. Even in noncytotoxic concentrations, polydisperse mixtures of TiO_2 with micron sized aggregates have been shown to trigger the release of reactive oxygen species in mouse brain cells, with cellular expressions of free radical formation.[186] The photocatalytic properties of nanosized TiO_2 under UV irradiation causes photo-oxidative stress that can induce the decrease of skin cell stiffness.[187] This implies that, while the oxide itself is not directly toxic, the physical and chemical effects on other cellular components warrants consideration. It brings to mind some concerns on the wear-and-tear of nanostructured surfaces, especially if the release of highly charged free particles is possible. This is a realization that, while beneficial for numerous reasons, the design and use of TiO_2 nanoparticles for various applications necessitates a cautious and skillful approach.

Chapter 8: Conclusions and Outlook

In which we summarize the key findings of this research and look forward to further study

8.1 Conclusions

The synthesis of TiO_2 nanoparticles with clean oxide surfaces and well-defined sizes was successfully achieved through the development of a protocol based on the hydrolysis of $TiCl_4$. Narrow particle size distributions and stable dispersions can be achieved by careful control of dialysis and storage time, as well as temperature. X-ray diffraction analysis revealed that the synthesis product is primarily anatase, brookite as the minority by-product (<10%). The TiO_2 crystallite size, representative of primary particles, was found to be about 4 nm. Results from DLS and ES-SMPS measurements show average sizes that are in good agreement. Data from the charactarization suggest that the different particle sizes obtained from synthesis are formed by slow aggregation.

The growth mechanism of TiO_2 from the hydrolysis of $TiCl_4$ involves an initial dissolution/precipitation process at low pH values where the solubility of the "active" titanium dioxide is still high. The growth of nanoparticles takes place by incorporation of mono-nuclear complexes to already existing solid material. This is supported by oscillations in the scattered intensity in DLS, reflecting the counteracting slow dissolution and precipitation reactions, where the rate is dependent on the local pH. At higher pH values during dialysis, where the solid fraction is >99%, particle formation is mainly determined by the surface charge. Dialysis also decreases the chloride concentration, consequently diminishing the screening of the particles. At this stage in the synthesis procedure stable agglomerates of nanoparticles are formed. The applicability of the ES-SMPS method for in-situ detection of nanoparticle size during growth was demonstrated. This technique is particularly valuable since it provides a direct measure of size.

The study of diffusion by DLS demonstrated nonlinear concentration dependence of the collective diffusion coefficient in dilute dispersions of TiO_2 nanoparticles. The effect is observed only for dispersions of small particles with diameters <10 nm. Calculations based on a simple binary sphere model, taking into account suspension polydispersity, were shown to qualitatively reproduce the observed experimental trends. Analysis of the model predictions suggest that the nonlinear concentration dependence derives from complex electrostatic interactions in the system, whereby small nanoparticles accumulate near the surfaces of larger particles, leading to measured diffusion coefficients which do not reflect those of the nanoparticles.

Experimental investigations at low pH values are afflicted with severe difficulties, due to large liquid junction potentials. Thus, theoretical calculations can be used to predict the surface charge density. The CDH-SC theory has been shown to effectively describe the surface charging behaviour in similar oxide nanoparticle systems and can be used to model the surface charging of TiO_2 nanoparticles. The theory predicts that particles of diameter <10 nm acquire high surface charge density, especially at low pH values. Titrations of 10 and 22 nm anatase particles with NaCl show that the zeta potential of smaller sized particles is smaller than for larger particles. The size-dependent trend is explained by the enhanced screening on

smaller particles by the counter ions. This observation is in very good agreement with the theoretical predictions.

The nanoparticles synthesized during the course of this work were used in two application studies. The electronic properties of TiO_2 nanoparticle films on titanium were investigated using electrochemical techniques. Compared to bulk titanium oxide, the nanoparticles show a higher conductivity and a clear presence of easily reducible surface states. These give rise to bands in the bandgap of the oxide and influence the adsorption properties. The latter was shown by fast nucleation of hydroxyapatite when immersed in simulated body fluid solution. The fast nucleation and high charge carrier concentration can be beneficial for osseointegration and studies are currently on-going to explore the applicability of nanoparticle covered titanium surfaces for dental implant applications.

Titanium nanoparticles were found to induce holes in supported lipid membranes via a Ca^{2+}-dependent mechanism. Experimental results from AFM and QCM-D suggest that the process is driven by the strong affinity between Ca^{2+} ions and TiO_2. Patches of the lipid membrane are ripped off as Ca^{2+} moves from the interface between the lipid membrane and the substrate towards the TiO_2 nanoparticle. This TiO_2-induced damage has clear implications on the potential toxicity of TiO_2 nanoparticles due to the possibility of penetration into cells.

8.2 Outlook

Based on the knowledge gained from this research work, further insight into the fascinating area of TiO_2 nanoparticles could be obtained by:

- More closely relating the sizing methods used in the thesis with transmission electron microscopy (TEM) studies. For example, the aggregation behaviour, morphology and crystallinity of the solid material could be followed during dialysis. This would enable evidence for specific growth mechanisms such as oriented attachment.

- Periodically and systematically monitoring the aging of the suspensions, by measuring the changes in size and crystalline structure, would give valuable information on the long-term thermodynamics of the nanoparticle system.

- In the surface charging of nanoparticles, the surface area and site density are key parameters. Preliminary potentiometric titrations have been performed on the synthesized TiO_2 nanoparticles and the results indicate a higher surface charge than expected from theoretical calculations using the CDH-SC model. A more detailed study of the surface area, using BET adsorption as well as other methods, together with an improved understanding of site density as a function size is necessary to fully understand the surface charging of the small oxide nanoparticles.

- The validity of the binary sphere model should be tested on other strongly charged, electrostatically stabilized particles and related to the theory of surface charging.

- Based on the fundamental understanding of the nanoparticle-solution interface it is highly valuable to explore the use of these particles in different applications. Two different applications are included in the thesis, both related to biological processes.

The interaction between the clean nanoparticle surfaces and proteins is one suggestion for future studies of importance for both osseointegration and uptake in the body.

- One important aspect which was not explored in this thesis is the fate of nanoparticles in the natural environment. The possible toxicity of small nanoparticles can be studied in terms of size-dependence, and processes such as interfacial reactivity of the oxide with organic material can yield information that can be used as the basis for larger-scale models and, eventually, nanomaterial-relevant regulations.

Acknowledgements

In which we give credit where it's due

They say it takes a village…

This fulfilling accomplishment would not have been possible without the kindness and support of everyone who played a part in this journey.

I thank the following institutions. The Department of Chemistry (and Molecular Biology) of the University of Gothenburg: for admitting me as a PhD student. The Swedish Research Council and the University of Gothenburg Strategic Research Platform "Nanoparticles in Interactive Environments": for providing the funding for experiments, as well as memorable conferences and summer schools.

My supervisor team: **Martin Hassellöv, Zareen Abbas, Johan Bergenholtz, Magnus Hagström, and Elisabet Ahlberg**.

Martin: thank you for recognizing my potential and recruiting me to apply for the PhD position. I am grateful for your kindness, career advice, and all your support.

Zareen: thank you for your generosity, your patience, and for showing me that theory need not be intimidating.

Johan: don't be fooled by the glazed expression, I did learn a lot about light scattering and colloidal systems. Thank you for your patience, practical lab guidance, and frank advice.

Magnus: thank you for your guidance during the start-up of the ES-SMPS work. Your practical tips came in quite handy.

Elisabet: what more can I say? You have plunged into the trenches with me and pulled me back in when the waters seemed so deep. Thank you for being a very dedicated mentor and for giving me a kick when I needed it.

Heartfelt thanks also go out to my examiners: **Sture Nordholm**, for the kind guidance during the "formative" years of my PhD education, and **Lennart Sjölin**, for graciously stepping in during the latter part, making sure that I kept on track, and also for mentorship during my years as a teaching assistant.

I would also like to thank my collaborators on the applications-related part of the TiO_2 research: **Ingela Mattison, Johanna Löberg**, and co-workers at Astra Tech for the dental implant study; **Fang Zhao**, **Rickard Frost**, **Bengt Kasemo**, and **Sofia Svedhem** of the Biological Physics Division (Chalmers) for the QCM-D/lipid bilayer study. Kudos also goes to **Stefan Gustafsson** of the Microscopy and Microanalysis Division (Chalmers) for help with my TEM measurements.

I must acknowledge my mentors who have, in one way or another, helped me nurture my interest and skills in science over the years: **Mrs. Rufina Perido, Dr. Amelia P. Guevara, Dr. Emilyn Espiritu, Dr. Teresita Perez, and Dr. Ann-Margret Strömvall**. You have been such inspiring role models.

A shout-out to the members of the Ahlberg Electrochemistry Group, past and present: **Adriano, Alex, Anders, Andrea, Angelica, Annika J., Gert, Jakub, Johanna, Kristoffer, Michael, Patrick, Tobias**. A vigorous wave to the former and current members of the Hassellöv

Environmental Nanochemistry Group: **Angela, Caroline, Eike, Geert, Jani, Julia H., Julián, Kajsa, Karin, Tobias P**. I have shared laughter and stress with you, those moments are fondly remembered. ☺

Special thanks to my fellow "lab brats" who have made my long hours around La Malvérne and ALV (the DLS gizmos) enjoyable and tolerable. **Anki**: thank you for a fruitful and fun collaboration, and for sharing your ES-SMPS expertise. I have enjoyed working with you, as well as the science fiction discussions and ice cream days. **Jeanette**: it was not always misery, but we do love the company…especially on Saturdays. **Mark & Ronja**: nice to have shared some laughs and good luck for your future research. **Moheb** in the bat-cave: we are the champions, my friend, and we'll keep on fighting 'till the end…

To my sisters in Chemistry who never stop rockin': **Annika E.-A., Carina B., Hallgerd, Iréne, Karinh, Petra, Susanne O.**, thanks for the good times and the cheer. Thanks to my suppliers, **Michael** and **Kübra**; the former for the Pour Bon luncheons, and the latter for shared meditation out in the fresh air. Cheers to my peers in the gruesome foursome foreign PhD dinner society: **Patrick, Fabio,** and **Inês**, I hope our friendship lasts beyond our years as researchers.

To my roommates, **Kajsa and Karin**: thank you for your understanding, support, ice-breakers, the "*arbetssocker*", and the periodic "Earth-to-Jenny" signals that kept my sanity intact during the surreal writing period. Thanks to my lovely friend **Caroline**, whose laser-proofreading eyes, cheery smile, and keen insight on *all* things have brought sunshine even during the hard winter. And to my former roommate but eternal buddy, Mama **Johanna Löberg**: *du är så grym! Kick-ass for the win, liksom*. Thank you for being a dear friend, for sharing this experience with me, for everything…if I list it here, I will run out of space and time (*typical Jenny*).

A loud holler out to my international cheerleaders! The beautiful **Sheila Paul, Richie, Vic, Bien, Atty. Maria, Chalor** and my friends from **UP Chemistry**, thank you for your encouragement. To my best friends **Ben** and **Jema**: *this is eeet*!

Family is everything. I give my deep thanks to the **Holmbergs**, for making Sweden home. To the **Duma-Perez** clan, I take your love wherever I go. To my late grandmother **Mama Sophie**, from whom I surely inherited this fiery blood, I give my eternal gratitude. **To my loving parents**, for instilling me with discipline, perseverance and fighting spirit which have helped me survive throughout these years. Thank you for making me take those language classes every summer, they have really paid off. **Dad**, from you I have learned logic, critical thinking and (trying to have) calmness under pressure. **Mom**, you patiently helped me learn to write essays, you gave me my first lesson in symmetry, and you have shared your impeccable organizational skills. **Blossom**, you will always be my favourite little sister who just can't stop impressing me. **Paolo** and **Mark**, you'll always be my sweet mischievous boys who bring happiness even to the toughest of days. Without you, I would not be where I am today. Love knows no distance.

Last but not the least, to my wonderful husband, **Björn**: thank you for showing me the world, for holding my hand as we plunge into the scary unknown, for always having my back, for being the ultimate wingman, and for loving me just the way I pesky am. *Jag älskar dig terramycket!*

Now as for the Village People that have kept me company on those late nights in the lab and in front of the computer…well, that's another story for another day. ☺

References

1. Greenwood, N. N.; Earnshaw, A., *Chemistry of the Elements*. 2nd ed.; Elsevier: Amsterdam, 1997.
2. Gussman, N., Titanium Dioxide: From Black Sand to White Pigment. *Chemical Engineering Progress* **2005,** 101, (6), 64.
3. Fujishima, A.; Hashimoto, K.; Watanabe, T., *TiO_2 Photocatalysis: Fundamentals and Applications*. 1st (English translation) ed.; BKC, Inc.: Tokyo, 1999.
4. Tryk, D. A.; Fujishima, A.; Honda, K., Recent topics in photoelectrochemistry: achievements and future prospects. *Electrochimica Acta* **2000,** 45, (15-16), 2363-2376.
5. Obare, S. O.; Meyer, G. J., Nanostructured Materials for Environmental Remediation of Organic Contaminants in Water. *Journal of Evnironmental Science and Health* **2004,** A39, (10), 2549-2582.
6. O'Regan, B.; Grätzel, M., A low-cost, high efficiency solar cell based on dye-sensitized colloidal TiO_2 films. *Nature* **1991,** 353, (6346), 737-740.
7. Viticoli, M.; Curulli, A.; Cusma, A.; Kaciulis, S.; Nunziante, S.; Pandolfi, L.; Valentini, F.; Padeletti, G., Third-generation biosensors based on TiO2 nanostructured films. *Materials Science and Engineering C* **2006,** 26, 947-951.
8. Mills, A.; Le Hunte, S., An overview of semiconductor photocatalysis. *Journal of Photochemistry and Photobiology A: Chemistry* **1997,** 108, (1), 1-35.
9. Jang, H. D.; Kim, S.-K.; King, S.-J., Effect of particle size and phase composition of titanium dioxide nanoparticles on the photocatalytic properties. *Journal of Nanoparticle Research* **2001,** 3, 141-147.
10. Abbas, Z.; Labbez, C.; Ahlberg, E.; Nordholm, S., Size-Dependent Surface Charging of Nanoparticles. *Journal of Physical Chemistry C* **2008,** 112, 5715-5723.
11. Alivisatos, A. P., Semiconductor Clusters, Nanocrystals, and Quantum Dots. *Science* **1996,** 271, 933-937.
12. Zhang, H.; Penn, R. L.; Hamers, R. J.; Banfield, J. F., Enhanced Adsorption of Molecules on Surfaces of Nanocrystalline Particles. *Journal of Physical Chemistry B* **1999,** 103, (22), 4656-4662.
13. Zhang, Q.-L.; Du, L.-C.; Weng, Y.-X.; Wang, L.; Chen, H.-Y.; Li, J.-Q., Particle-Size-Dependent Distribution of Carboxylate Adsorption Sites on TiO_2 Nanoparticle Surfaces: Insights into the Surface Modification of Nanostructured TiO_2 Electrodes. *Journal of Physical Chemistry B* **2004,** 108, 15077-15083.
14. Rajh, T.; Nedeljkovic, J. M.; Chen, L. X.; Poluektov, O.; Thurnauer, M. C., Improving Optical and Charge Separation Properties of Nanocrystalline TiO_2 by Surface Modification with Vitamin C. *Journal of Physical Chemistry B* **1999,** 103, 3515-3519.
15. Nowotny, J.; Bak, T.; Nowotny, M. K.; Sheppard, L. R., Defect Chemistry and Electrical Properties of Titanium Dioxide. 1. Defect Diagrams. *Journal of Physical Chemistry C* **2008,** 112, 590-601.
16. Kambe, S.; Nakade, S.; Wada, Y.; Kitamura, T.; Yanagida, S., Effects of crystal structure, size, shape and surface structural differences on photo-induced electron transport in TiO_2 mesoporous electrodes. *Journal of Materials Chemistry* **2002,** 12, 723-728.
17. Chou, T. P.; Zhang, Q.; Russo, B.; Fryxell, G. E.; Cao, G., Titania Particle Size Effect on the Overall Performance of Dye-Sensitized Solar Cells. *J. Phys. Chem. C* **2007,** 111, 6296-6302.
18. Addamo, M.; Augugliaro, V.; Di Paola, A.; García-López, E.; Loddo, V.; Marci, G.; Molinari, R.; Palmisano, L.; Schiavello, M., Preparation, Characterization and Photoactivity of Polycrystalline Nanostructured TiO_2 Catalysts. *Journal of Physical Chemistry B* **2004,** 108, (10), 3303-3310.
19. Ribeiro, C.; Vila, C.; Stroppa, D. B.; Mastelaro, V. R.; Bettini, J.; Longo, E.; Leite, E. R., Anisotropic Growth of Oxide Nanocrystals: Insights into the Rutile TiO_2 Phase. *Journal of Physical Chemistry C* **2007,** 111, (16), 5871-5875.

20. Tian, B.; Chen, F.; Zhang, J.; Anpo, M., Influences of acids and salts on the crystalline phase and morphology of TiO2 prepared under ultrasound irradiation. *Journal of Colloid and Interface Science* **2006,** 303, 142-148.
21. Li, G.; Li, L.; Boerio-Goates, J.; Woodfield, B. F., High Purity Anatase TiO2 Nanocrystals: Near Room-Temperature Synthesis, Grain Growth Kinetics, and Surface Hydration Chemistry. *Journal of the American Chemical Society* **2005,** 127, 8659-8666.
22. Mori, Y.; Okastu, Y.; Tsujimoto, Y., Titanium dioxide nanoparticles produced in water-in-oil emulsion. *Journal of Nanoparticle Research* **2001,** 3, (2-3), 219-225.
23. Liang, C. H.; Shimizu, Y.; Sasaki, T.; Koshizaki, N., Preparation of ultrafine TiO_2 nanocrystals via pulsed-laser ablation of titanium metal in surfactant solution. *Applied Physics A* **2005,** 80, (4), 819-822.
24. Saxe, J. G., *The Poems of John Godfrey Saxe*. Ticknor and Fields: Boston, 1868.
25. Finsy, R., Particle Sizing by Quasi-elastic Light Scattering. *Advances in Colloid and Interface Science* **1994,** 52, 79-143.
26. Malvern "Dynamic Light Scattering Instrumentation for classical 90 degree scattering measurements". http://www.malvern.com/labeng/technology/dynamic_light_scattering/classical_90_degree_scattering.htm
27. Hiemenz, P. C.; Rajagopalan, R., *Principles of Colloid and Surface Chemistry*. 3rd ed.; CRC Taylor & Francis: Boca Raton, Florida, 1997.
28. Dhont, J. K. G., *An introduction to dynamics of colloids*. Elsevier: Amsterdam; New York, 1996; Vol. 2.
29. Koppel, D. E., Analysis of Macromolecular Polydispersity in Intensity Correlation Spectroscopy: The Method of Cumulants. *Journal of Chemical Physics* **1972,** 57, (1), 4814-4820.
30. Brown, J.; Pusey, P. N.; Dietz, R., Photon correlation study of polydisperse samples of polystyrene in cyclohexane. *Journal of Chemical Physics* **1975,** 62, (3), 1136-1144.
31. Provencher, S. W., CONTIN: A General Purpose Constrained Regularization Program for Inverting Noisy Linear Algebraic and Integral Equations. *Computer Physics Communications* **1982,** 27, 229-242.
32. Ware, B. R., Electrophoretic Light Scattering. *Advances in Colloid and Interface Science* **1974,** 4, 1-44.
33. Mohan, R.; Steiner, R.; Kaufmann, R., Laser Doppler Spectroscopy as Applied to Electrophoresis in Protein Solutions. *Analytical Biochemistry* **1976,** 70, 506-525.
34. Bennett, A. J.; Uzgiris, E. E., Laser Doppler Spectroscopy in an Oscillating Electric Field. *Physical Review A* **1973,** 8, (5), 2662-2669.
35. Ware, B. R.; Flygare, W. H., The simultaneous measurement of the electrophoretic mobility and diffusion coefficient in bovine serum albumin solutions by light scattering. *Chemical Physics Letters* **1971,** 12, (1), 81-85.
36. Ohshima, H., Interfacial Electrokinetic Phenomena. In *Electrical Phenomena at Interfaces: Fundamentals, Measurements, and Applications*, 2nd ed.; Ohshima, H.; Furusawa, K., Eds. Marcel Dekker, Inc.: New York, 1998; Vol. 76, pp 19-55.
37. Uzgiris, E. E., Laser Doppler Methods in Electrophoresis. *Progress in Surface Science* **1981,** 10, 53-164.
38. Agarwal, J. K.; Sem, G. J., Continuous flow, single particle-counting condensation nucleus counter. *J. Aerosol. Sci* **1980,** 11, 343-357.
39. Johnsson, A.-C. On the Electrolyte Induced Aggregation of Concentrated Silica Dispersions. University of Gothenburg, Gothenburg, Sweden, 2011.
40. Pease, L. F. I.; Tsai, D.-H.; Hertz, J. L.; Zangmeister, R. A.; Zachariah, M. R.; Tarlov, M. J., Packing and Size Determination of Colloidal Nanoclusters. *Langmuir* **2010,** 26, (13), 11384-11390.
41. Lenggoro, I. W.; Xia, B.; Okuyama, K.; de la Mora, J. F., Sizing of Colloidal Nanoparticles by Electrospray and Differential Mobility Analyzer Methods. *Langmuir* **2002,** 18, 4584-4591.
42. Taylor, G., Disintegration of Water Drops in an Electric Field. *Proceedings of the Royal Society fo London. Series A, Mathematical and Physical Sciences* **1964,** 280, (1382), 383-397.

43. Cloupeau, M.; Prunet-Foch, B., Electrohydrodynamic spraying functioning modes: A critical review. *J. Aerosol. Sci* **1994,** 25, (6), 1021-1036.
44. Rosell-Llompart, J.; De la Mora, J. F., Generation of monodisperse droplets 0.3 to 4 μm in diameter from electrified cone-jets of highly conducting and viscous liquids. *J. Aerosol. Sci* **1994,** 25, (6), 1093-1119.
45. Ku, B. K.; Kim, S. S.; Kim, Y. D.; Lee, S. Y., Direct measurement of electrospray droplets in submicron diameter using a freezing method and a TEM image processing technique. *J. Aerosol. Sci* **2001,** 32, 1459-1477.
46. Cloupeau, M., Recipes for use of EHD spraying in cone-jet mode and notes on corona discharge effects. *J. Aerosol. Sci* **1994,** 25, (6), 1143-1157.
47. Taflin, D. C.; Ward, T. L.; Davis, E. J., Electrified droplet fission and the Rayleigh limit. *Langmuir* **1989,** 5, 376-384.
48. DeCarlo, P. F.; Slowik, J. G.; Worsnop, D. R.; Davidovits, P.; Jimenez, J. L., Particle Morphology and Density Characterization by Combined Mobility and Aerodynamic Diameter Measurements. Part 1: Theory. *Aerosol Science and Technology* **2004,** 38, 1185-1205.
49. De la Mora, J. F.; de Juan, L.; Eichler, T.; Rosell, J., Differential mobility analysis of molecular ions and nanometer particles. *Trends in analytical chemistry* **1998,** 17, (6), 328-339.
50. Knutson, E. O.; Whitby, K. T., Aerosol Classification by Electric Mobility: Apparatus, Theory, and Applications. *Aerosol Sci.* **1975,** 6, 443-451.
51. Chen, D.-R.; Pui, D. Y. H.; Hummes, D.; Fissan, H.; Quant, F. R.; Sem, G. J., Design and Evaluation of a Nanometer Aerosol Differential Mobility Analyzer (Nano-DMA). *J. Aerosol. Sci* **1998,** 29, (5/6), 497-509.
52. Endo, Y.; Fukushima, N.; Tashiro, S.; Kousaka, Y., Performance of a Scanning Differential Mobility Analyzer. *Aerosol Science and Technology* **1997,** 26, (1), 43-50.
53. Stolzenburg, M. R. An ultrafine aerosol size distribution measuring system. University of Minnesota, Minneapolis, 1988.
54. Stratmann, F.; Kauffeldt, T.; Hummes, D.; Fissan, H., Differential Electrical Mobility Analysis: A Theoretical Study. *Aerosol Science and Technology* **1997,** 26, (4), 368-383.
55. Birmili, W.; Stratmann, F.; Wiedensohler, A.; Covert, D. S.; Russell, L. M.; Berg, O., Determination of Differential Mobility Analyzer Transfer Functions Using Identical Instruments in Series. *Aerosol Science and Technology* **1997,** 27, (2), 215-223.
56. Fissan, H.; Hummes, D.; Stratmann, F.; Büscher, P.; Neumann, S.; Pui, D. Y. H.; Chen, D., Experimental Comparison of Four Differential Mobility Analyzers for Nanometer Aerosol Measurements. *Aerosol Science and Technology* **1996,** 24, (1), 1-13.
57. Wiedensohler, A.; Orsini, D.; Covert, D. S.; Coffmann, D.; Cantrell, W.; Havlicek, M.; Brechtel, F. J.; Russell, L. M.; Weber, R. J.; Gras, J.; Hudson, J. G.; Litchy, M., Intercomparison Study of the Size-Dependent Counting Efficiency of 26 Condensation Particle Counters. *Aerosol Science and Technology* **1997,** 27, 224-242.
58. Stolzenburg, M. R.; McMurry, P. H., An Ultrafine Aerosol Condensation Nucleus Counter. *Aerosol Science and Technology* **1991,** 14, (1), 48-65.
59. Mertes, S.; Schröder, F.; Wiedensohler, A., The Particle Detection Efficiency Curve of the TSI-3010 CPC as a Function of the Temperature Difference between Saturator and Condenser. *Aerosol Science and Technology* **1995,** 23, 257-261.
60. Poole, C. P.; Owens, F. J., *Introduction to Nanotechnology*. John Wiley & Sons, Inc.: New Jersey, 2003.
61. West, A. R., *Basic Solid State Chemistry*. 2nd ed.; John Wiley & Sons, Ltd.: Chichester, 2006.
62. Smart, L. E.; Moore, E. A., *Solid State Chemistry: An Introduction*. 3rd ed.; Taylor & Francis: Boca Raton, 2005.
63. Langford, J. I.; Wilson, A. J. C., Scherrer after Sixty Years: A Survey and Some New Results in the Determination of Crystallite Size. *J. Appl. Cryst.* **1978,** 11, 102-113.
64. Scherrer, P., Bestimmung der Grösse und der inneren Struktur von Kolloidteilchen mittels Röntgenstrahlen. *Nachr. Ges. Wiss. Göttingen* **1918,** 26, 98-100.
65. Patterson, A. L., The Scherrer Formula for X-ray Particle Size Determination. *Physical Review* **1939,** 56, 978-982.

66. Williams, D. B.; Carter, C. B., *Transmission Electron Microscopy - Part 1: Basics*. 2nd ed.; Springer Science+Business Media, LLC: New York, 2009; Vol. 1.
67. Albright, R. D., *Cleanup of Chemical and Explosive Munitions: Locating, Identifying Contaminants, and Planning for Environmental Remediation of Land and Sea Military Ranges and Ordnance Dumpsites*. William Andrew Publishing: Norwich, NY, U.S.A, 2008.
68. Stwertka, A., *A Guide to the Elements*. 2nd ed.; Oxford University Press: Oxford, 1996.
69. Sandler, S., *World War II in the Pacific: an encyclopedia*. Garland Publishing Inc.: New York, 2001.
70. Abbas, Z.; Perez Holmberg, J.; Hellström, A. K.; Hagström, M.; Bergenholtz, J.; Hassellöv, M.; Ahlberg, E., Synthesis, characterization and particle size distribution of TiO_2 colloidal nanoparticles. *Colloids and Surfaces A: Physicochem. Eng. Aspects* **2011,** 384, 254-261.
71. Wang, T.-H.; Navarrete-López, A. M.; Li, S.; Dixon, D. A.; Gole, J. L., Hydrolysis of $TiCl_4$: Initial Steps in the Production of TiO_2. *J. Phys. Chem. A* **2010,** 114, (28), 7561-7570.
72. Xia, B.; Huang, H.; Xie, Y., Heat treatment on TiO_2 nanoparticles prepared by vapor-phase hydrolysis. *Materials Science and Engineering B* **1999,** 57, (2), 150-154.
73. Kotsokechagia, T.; Cellesi, F.; Thomas, A.; Niederberger, M.; Tirelli, N., Preparation of Ligand-Free TiO2 (Anatase) Nanoparticles through a Nonaqueous Process and Their Surface Functionalization. *Langmuir* **2008,** 24, 6988-6997.
74. Addamo, M.; Augugliaro, V.; Di Paola, A.; García-López, E.; Loddo, V.; Marcì, G.; Palmisano, L., Preparation and photoactivity of nanostructured TiO_2 particles obtained by hydrolysis of $TiCl_4$. *Colloids and Surfaces A: Physicochem. Eng. Aspects* **2005,** 265, (1), 23-31.
75. Kolen'ko, Y. V.; Burukhin, A. A.; Churagulov, B. R.; Oleynikov, N. N., Synthesis of nanocrystalline TiO_2 powders from aqueous $TiOSO_4$ solutions under hydrothermal conditions. *Materials Letters* **2003,** 57, (5-6), 1124-1129.
76. Hald, P.; Becker, J.; Bremholm, M.; Pedersen, J. S.; Chevallier, J.; Iversen, S. B.; Iversen, B. B., Supercritical Propanol-Water Synthesis and Comprehensive Size Characterisation of Highly Crystalline Anatase TiO_2 Nanoparticles. *Journal of Solid State Chemistry* **2006,** 179, (8), 2674-2680.
77. O'Regan, B.; Moser, J.; Anderson, M.; Grätzel, M., Vectorial Electron Injection into Transparent Semiconductor Membranes and Electric Field Effects on the Dynamics of Light-Induced Charge Separation. *J. Phys. Chem.* **1990,** 94, (24), 8720-8726.
78. Kormann, C.; Bahnemann, D. W.; Hoffmann, M. R., Preparation and Characterization of Quantum-Size Titanium Dioxide. *Journal of Physical Chemistry* **1988,** 92, 5196-5201.
79. Serpone, N.; Lawless, D.; Khairutdinov, R., Size Effects on the Photophysical Properties of Colloidal Anatase TiO_2 Particles: Size Quantization or Direct Transitions in This Indirect Semiconductor? *Journal of Physical Chemistry* **1995,** 99, 16646-16654.
80. Zhang, H.; Banfield, J. F., Thermodynamic analysis of phase stability of nanocrystalline titania. *Journal of Materials Chemistry* **1998,** 8, (9), 2073-2076.
81. Zhang, H.; Banfield, J. F., Understanding Polymorphic Phase Transformation Behavior during Growth of Nanocrystalline Aggregates: Insights from TiO_2. *Journal of Physical Chemistry B* **2000,** 104, (15), 3481-3487.
82. Ohsaka, T.; Izumi, F.; Fujiki, Y., Raman Spectrum of Anatase, TiO_2. *Journal of Raman Spectroscopy* **1978,** 7, (6), 321-324.
83. Balachandran, U.; Eror, N. G., Raman Spectra of Titanium Dioxide. *Journal of Solid State Chemistry* **1982,** 42, 276-282.
84. Mo, S.-D.; Ching, W. Y., Electronic and optical properties of three phases of titanium dioxide: Rutile, anatase, and brookite. *Physical Review B* **1995,** 51, (19), 13023-13032.
85. Pottier, A.; Cassaignon, S.; Chanéac, C.; Villain, F.; Tronc, E.; Jolivet, J.-P., Size tailoring of TiO_2 anatase nanoparticles in aqueous medium and synthesis of nanocomposites. Characterization by Raman spectroscopy. *Journal of Materials Chemistry* **2003,** 13, 877-882.
86. Jolivet, J.-P.; Cassaignon, S.; Chanéac, C.; Chiche, D.; Durupthy, O.; Portehault, D., Design of metal oxide nanoparticles: Control of size, shape, crystalline structure and functionalization by aqueous chemistry. *C.R. Chimie* **2010,** 13, 40-51.
87. Zhang, H.; Chen, B.; Banfield, J. F.; Waychunas, G. A., Atomic structure of nanometer-sized amorphous TiO_2. *Physical Review B* **2008,** 78, 214106-1-12.

88. Pottier, A.; Chanéac, C.; Tronc, E.; Mazerolles, L.; Jolivet, J.-P., Synthesis of brookite TiO_2 nanoparticles by thermolysis of $TiCl_4$ in strongly acidic aqueous media. *Journal of Materials Chemistry* **2001,** 11, 1116-1121.
89. Lee, J. H.; Yang, Y. S., Effect of hydrolysis conditions on morphology and phase content in the crystalline TiO_2 nanoparticles synthesized from aqueous $TiCl_4$ solution by precipitation. *Material Chemistry and Physics* **2005,** 93, 237-242.
90. Jolivet, J.-P.; Cassaignon, S.; Chanéac, C.; Chiche, D.; Tronc, E., Design of oxide nanoparticles by aqueous chemistry. *J. Sol-Gel Sci. Technol.* **2008,** 46, 299-305.
91. Pusey, P. N.; van Megen, W., Detection of small polydispersities by photon correlation spectroscopy. *Journal of Chemical Physics* **1984,** 80, (8), 3513-3520.
92. Flagan, R. C., Electrical Techniques. In *Aerosol Measurement: Principles, Techniques, and Applications*, Baron, P. A.; Willeke, K., Eds. John Wiley: New York, 2001; pp 537-568.
93. Perez Holmberg, J.; Johnsson, A.-C.; Bergenholtz, J.; Abbas, Z.; Ahlberg, E., Near room temperature synthesis of monodisperse TiO_2 nanoparticles - Growth mechanism. *(submitted to PCCP)* **2012**.
94. Liberti, A.; Chiantella, V.; Corigliano, F., Mononuclear Hydrolysis of Titanium (IV) from Partition Equilibria. *Journal of Inorganic Nuclear Chemistry* **1963,** 25, 415-427.
95. Baes, C. F.; Mesmer, R. E., *The Hydrolysis of Cations*. John Wiley & Sons: New York, 1976.
96. Nabivanets, B. I.; Kudritskaya, L. N., Determination of the Composition and Dissociation Constants of Titanyl Chloro-complexes. *Russian Journal of Inorganic Chemistry* **1967,** 12, (6), 789-792.
97. Eriksson, G., An Algorithm for the Computation of Aqueous Multi-component, Multiphase Equilibria. *Analytica Chimica Acta* **1979,** 112, (4), 375-383.
98. Chen, D.-R.; Pui, D. Y. H.; Kaufman, S. L., Electrospraying of Conducting Liquids for Monodisperse Aerosol Generation in the 4 nm to 1.8 μm Diameter Range. *J. Aerosol Sci.* **1995,** 26, (6), 963-977.
99. Van den Broeck, C.; Lostak, F.; Lekkerkerker, H. N. W., The effect of direct interactions on Brownian diffusion. *Journal of Chemical Physics* **1981,** 74, (3), 2006-2010.
100. Epstein, I. R.; Showalter, K., Nonlinear Chemical Dynamics: Oscillations, Patterns and Chaos. *Journal of Physical Chemistry* **1996,** 100, (31), 13132-13147.
101. Rábai, G.; Orbán, M.; Epstein, I. R., Design of pH-Regulated Oscillators. *Accounts of Chemical Research* **1990,** 23, (8), 258-263.
102. Volford, A.; Izsák, F.; Ripszám, M.; Lagzi, I., Pattern Formation and Self-Organization in a Simple Precipitation System. *Langmuir* **2007,** 23, (3), 961-964.
103. Müller, S. C.; Ross, J., Spatial Structure Formation in Precipitation Reactions. *Journal of Physical Chemistry A* **2003,** 107, (39), 7997-8008.
104. John, A. K.; Savithri, S.; Vijayalakshmi, K. P.; Suresh, C. H., Density Functional Theory Study of Gas Phase Hydrolysis of Titanium Tetrachloride. *Bull. Chem. Soc. Jpn.* **2010,** 83, (9), 1030-1036.
105. Matijevic, E.; Budnik, M.; Meites, L., Preparation and Mechanism of Formation of Titanium Dioxide Hydrolsols of Narrow Size Distribution. *Journal of Colloid and Interface Science* **1977,** 61, (2), 302-311.
106. Perez Holmberg, J.; Abbas, Z.; Ahlberg, E.; Hassellöv, M.; Bergenholtz, J., Nonlinear Concentration Dependence of the Collective Diffusion Coefficient of TiO_2 Nanoparticle Dispersions. *Journal of Physical Chemistry C* **2011,** 115, 13609-13616.
107. Siegert, A. J. F., MIT Radiation Laboratory Report. In Cambridge, Massachusetts, 1943.
108. Borsali, R., Scattering properties of ternary polymer solutions. In *Light Scattering: Principles and Development*, Brown, W., Ed. Oxford University Press: Oxford, 1996; pp 255-289.
109. Pusey, P. N.; Fijnaut, H. M.; Vrij, A., Mode amplitudes in dynamic light scattering by concentrated liquid suspensions of polydisperse hard spheres. *Journal of Chemical Physics* **1982,** 77, (9), 4270-4281.
110. van Beurten, P.; Vrij, A., Polydispersity effects in the small-angle scattering of concentrated solutions of colloidal spheres. *Journal of Chemical Physics* **1981,** 74, (5), 2744-2748.
111. Nägele, G.; Kellerbauer, O.; Krause, R.; Klein, R., Hydrodynamic effects in polydisperse charged colloidal suspensions at short times. *Physical Review E* **1993,** 47, (4), 2562-2574.

112. Batchelor, G. K., Sedimentation in a dilute dispersion of spheres. *Journal of Fluid Mechanics* **1972,** 52, 245-268.
113. Chichocki, B.; Felderhof, B. U., Short-time diffusion coefficients and high frequency viscosity of dilute suspensions of spherical Brownian particles. *Journal of Chemical Physics* **1988,** 89, (2), 1049-1054.
114. Thies-Weesie, D.; Philipse, A. P.; Nägele, G.; Mandl, B.; Klein, R., Nonanalytical Concentration Dependence of Sedimentation of Charged Silica Spheres in an Organic Solvent: Experiments. *Journal of Colloid and Interface Science* **1995,** 176, 43-54.
115. Watzlawek, M.; Nägele, G., Sedimentation of Strongly and Weakly Charged Colloidal Particles: Prediction of Fractional Density Dependence. *Journal of Colloid and Interface Science* **1999,** 214, 170-179.
116. Denkov, N. D.; Petsev, D. N., Light scattering and diffusion in suspensions of strongly charged particles at low volume fractions. *Physica A* **1992,** 183, 462-489.
117. Petsev, D. N.; Denkov, N. D., Diffusion of Charged Colloidal Particles at Low Volume Fraction: Theoretical Model and Light Scattering Experiments. *Journal of Colloid and Interface Science* **1992,** 149, (2), 329-344.
118. Watzlawek, M.; Nägele, G., Self-diffusion coefficients of charged particles: Prediction of nonlinear volume fraction dependence. *Physical Review E* **1997,** 56, (1), 1258-1261.
119. Watzlawek, M.; Nägele, G., Short-time rotational diffusion in monodisperse charge-stabilized colloidal suspensions. *Physica A* **1997,** 235, 56-74.
120. Finsy, R.; Moreels, E.; Bottger, A.; Lekkerkerker, H., Study of the relation between diffusion and sedimentation of charged silica sols by dynamic light scattering, ultracentrifugation, and turbidimetry. *Journal of Chemical Physics* **1985,** 82, (8), 3812-3816.
121. Gapinski, J.; Wilk, A.; Patrowski, A.; Häussler, W.; Banchio, A. J.; Pecora, R.; Nägele, G., Diffusion and microstructural properties of solutions of charged nanosized proteins: Experiment versus theory. *Journal of Chemical Physics* **2005,** 123, 054708-1-13.
122. Abade, G. C.; Cichocki, B.; Ekiel-Jezewska, M. L.; Nägele, G.; Wajnryb, E., Short-time dynamics of permeable particles in concentrated suspensions. *J. Chem. Phys.* **2010,** 132, (1), 014503.
123. Denton, A. R., Counterion penetration and effective electrostatic interactions in solutions of polyelectrolyte stars and microgels. *Physical Review E* **2003,** 67, 011804.
124. Ruiz-Estrada, H.; Medina-Noyola, M.; Nägele, G., Rescaled mean spherical approximation for colloidal mixtures. *Physica A* **1990,** 168, 919-941.
125. Klein, R.; D'Aguanno, B., Static scattering properties of colloidal suspensions. In *Light Scattering: Principles and Development*, Brown, W., Ed. Oxford University Press: Oxford, 1996; pp 30-99.
126. Hansen, J.-P.; McDonald, I. R., *Theory of Simple Liquids*. 3rd ed.; Elsevier: Amsterdam, 2006; p 416.
127. Chan, A. T.; Lewis, J. A., Electrostatically Tuned Interactions in Silica Microsphere - Polystyrene Nanoparticle Mixtures. *Langmuir* **2005,** 21, 8576-8579.
128. Tohver, V.; Chan, A. T.; Sakurada, O.; Lewis, J. A., Nanoparticle Engineering of Complex Fluid Behavior. *Langmuir* **2001,** 17, 8414-8421.
129. Tohver, V.; Smay, J. E.; Braem, A.; Braun, P. V.; Lewis, J. A., Nanoparticle halos: A new colloid stabilization mechanism. *Proceedings of the National Academy of Sciences of the United States of America* **2001,** 98, (16), 8950-8954.
130. Coutinho, C. A.; Harrinauth, R. K.; Gupta, V. K., Settling characteristics of composites of PNIPAM microgels and TiO_2 nanoparticles. *Colloids and Surfaces A: Physicochem. Eng. Aspects* **2008,** 318, 111-121.
131. Perez Holmberg, J.; Ahlberg, E.; Bergenholtz, J.; Hassellöv, M.; Abbas, Z., Surface Charge and Interfacial Potential of TiO_2 Nanoparticles: Theoretical and Experimental Investigations. *(manuscript)* **2012**.
132. Davis, J. A.; Kent, D. B., Surface Complexation Modeling in Aqueous Geochemistry. *Reviews in Mineralogy* **1990,** 23, 177-260.
133. Petersson, I. U.; Löberg, J.; Fredriksson, A. S.; Ahlberg, E., Semi-conducting properties of titanium dioxide surfaces on titanium implants. *Biomaterials* **2009,** 30, 4471-4479.

134. Hunter, R. J., *Foundations of Colloid Science*. 2nd ed.; Oxford University Press: Oxford, 2001.
135. Malvern "Electrophoretic Light Scattering - Overview". http://www.malvern.com/labeng/technology/electrophoretic-light-scattering.htm
136. Bourikas, K.; Hiemstra, T.; Van Riemsdijk, W. H., Ion Pair Formation and Primary Charging Behavior of Titanium Oxide (Anatase and Rutile). *Langmuir* **2001,** 17, 749-756.
137. Hiemstra, T.; De Wit, J. C. M.; Van Riemsdijk, W. H., Multisite Proton Adsorption Modeling at the Solid/Solution Interface of (Hydr)oxides: A New Approach. I. Model Description and Evaluation of Intrinsic Reaction Constants. *Journal of Colloid and Interface Science* **1989,** 133, (91-104).
138. Hiemstra, T.; De Wit, J. C. M.; Van Riemsdijk, W. H., Multisite Proton Adsorption Modeling at the Solid/Solution Interface of (Hydr)oxides: A New Approach. II. Application to Various Important (Hydr)oxides. *Journal of Colloid and Interface Science* **1989,** 133, (105-117).
139. Lyklema, J., *Fundamentals of Interface and Colloid Science*. Academic Press: London, 1995; Vol. II Solid-Liquid Interfaces.
140. Hellström, A. K. Surface charging and fluoride ion adsorption on TiO_2 (P25). University of Gothenburg, Gothenburg, Sweden, 2005.
141. Gunnarsson, M.; Abbas, Z.; Ahlberg, E.; Nordholm, S., Corrected Debye-Hückel analysis of surface complexation: III. Spherical particle charging including ion condensation. *Journal of Colloid and Interface Science* **2004,** 274, (2), 563-578.
142. Ohko, Y.; Tatsuma, T.; Fujii, T.; Naoi, K.; Niwa, C.; Kubota, Y.; Fujishima, A., Multicolour photochromism of TiO_2 films loaded with silver nanoparticles. *Nature Materials* **2003,** 2, 29-31.
143. Parkin, I. P.; Palgrave, R. G., Self-cleaning coatings. *Journal of Materials Chemistry* **2005,** 15, 1689-1695.
144. Daoud, W. A.; Leung, S. K.; Tung, W. S.; Xin, J. H.; Cheuk, K.; Qi, K., Self-Cleaning Keratins. *Chem. Mater.* **2008,** 20, 1242-1244.
145. Daoud, W. A.; Xin, J. H., Nucleation and Growth of Anatase Crystallites on Cotton Fabrics at Low Temperatures. *Journal of the American Ceramic Society* **2004,** 87, (5), 953-955.
146. Qi, K.; Daoud, W. A.; Xin, J. H.; Mak, C. L.; Tang, W.; Cheung, W. P., Self-cleaning cotton. *Journal of Materials Chemistry* **2006,** 16, 4567-4574.
147. Grandcolas, M.; Louvet, A.; Keller, N.; Keller, V., Layer-by-Layer Deposited Titanate-Based Nanotubes for Solar Photocatalytic Removal of Chemical Warfare Agents from Textiles. *Angew. Chem. Int. Ed.* **2009,** 48, 161-164.
148. Löberg, J.; Perez Holmberg, J.; Mattisson, I.; Arvidsson, A.; Ahlberg, E., Electronic properties of TiO_2 nanoparticle films and the effect on bioactivity. *(manuscript)* **2011**.
149. Zhao, F.; Perez Holmberg, J.; Frost, R.; Abbas, Z.; Kasemo, B.; Hassellöv, M.; Svedhem, S., TiO_2 nanoparticle induced damage in lipid membranes. *(submitted)* **2012**.
150. Hollander, J. M.; Jolly, W. L., X-ray Photoelectron Spectroscopy. *Acc. Chem. Res.* **1970,** 3, (6), 193-200.
151. Löberg, J.; Mattisson, I.; Hansson, S.; Ahlberg, E., Characterisation of Titanium Dental Implants I: Critical Assessment of Surface Roughness Parameters. *The Open Biomaterials Journal* **2010,** 2, 18-35.
152. MeX 5.0; Graz, Austria 2007.
153. Löberg, J. Integrated Biomechanical, Electronic and Topographic Characterization of Titanium Dental Implants. University of Gothenburg, Gothenburg, Sweden, 2011.
154. Hansson, S.; Löberg, J.; Mattisson, I.; Ahlberg, E., Characterisation of Titanium Dental Implants II: Local Biomechanical Model. *The Open Biomaterials Journal* **2010,** 2, 36-52.
155. Hansson, S.; Löberg, J.; Mattisson, I.; Ahlberg, E., Global biomechanical model for dental implants. *J. Biomech.* **2011,** 44, 1059-1065.
156. Hagfeldt, A.; Grätzel, M., Light-Induced Redox Reactions in Nanocrystalline Systems. *Chem. Rev.* **1995,** 95, (1), 49-68.
157. Bard, A. J.; Faulkner, L. R., *Electrochemical Methods: Fundamentals and Applications*. John Wiley & Sons, Inc.: Hoboken, NJ, 2001.
158. Berger, T.; Lana-Villarreal, T.; Monllor-Satoca, D.; Gómez, R., An Electrochemical Study on the Nature of Trap States in Nanocrystalline Rutile Thin Films. *J. Phys. Chem. C* **2007,** 111, 9936-9942.

159. Hirschorn, B.; Orazem, M. E.; Tribollet, B.; Vivier, V.; Frateur, I.; Musiani, M., Determination of effective capacitance and film thickness from constant-phase-element parameters. *Electrochim. Acta* **2010,** 55, 6218-6227.
160. Brug, G. J.; van den Eeden, A. L. G.; Sluyters-Rehbach, M.; Sluyters, J. H., The analysis of electrode impedance comlicated by the presence of a constant phase element. *J. Electroanal. Chem.* **1984,** 176, 275-295.
161. Barsoukov, E.; Macdonald, J. R., *Impedance Spectroscopy Theory, Experiment and Applications*. 2nd ed.; Wiley: Hoboken, NJ, 2005.
162. Bott, A. W., Electrochemistry of Semiconductors. *Current Separations* **1998,** 17, (3), 87-91.
163. Boschloo, G.; Fitzmaurice, D., Electron accumulation in nanostructure TiO_2 (Anatase) electrodes. *J. Phys. Chem. B* **1999,** 103, 7860-7868.
164. Oyane, A.; Kim, H. M.; Furuya, T.; Kokubo, T.; Miyazaki, T.; Nakamura, T., Preparation and assessment of revised body fluids. *J. Biomech. Mater. Res. A* **2003,** 65, (2), 188-195.
165. Chen, X.; Nouri, A.; Li, Y.; Lin, J.; Hodgson, P. D.; Wen, C., Effect of surface roughness of Ti, Zr and TiZr on apatite precipitation from simulated body fluid. *Biotechnol. Bioeng.* **2008,** 101, (2), 378-387.
166. Uchida, M.; Kim, H. M.; Kokubo, T.; Fujibayashi, S.; Nakamura, T., Effect of water treatment on the apatite-forming ability of NaOH-treated titanium metal. *J. Biomed. Mater. Res.* **2002,** 63, 522-530.
167. Uchida, M.; Kim, H. M.; Kokubo, T.; Fujibayashi, S.; Nakamura, T., Structural dependence of apatite formation on titania gels in a simulated body fluid. *J. Biomed. Mater. Res.* **2003,** 64A, 164-170.
168. Ohno, T.; Sarukawa, K.; Tokieda, K.; Matsumura, M., Morphology of a TiO_2 Photocatalyst (Degussa, P-25) Consisting of Anatase and Rutile Crystalline Phases. *J. Catal.* **2001,** 203, 82-86.
169. Ning, C. Q.; Zhou, Y., In vitro bioactivity of a biocomposite fabricated from HA and Ti powders by powder metallurgy method. *Biomaterials* **2009,** 23, 2909-2915.
170. Reis, R. L.; Cunha, A. M., Treatments to induce the nucleation and growth of apatite-like layers on polymeric surfaces and foams. *J. Mater. Sci. Mater Med.* **1997,** 8, 897-905.
171. Barrere, F.; Snel, M. M.; van Blitterswijk, C. A.; de Groot, K.; Layrolle, P., Nano-scale study of the nucleation and growth of calcium phosphate coating on titanium implants. *Biomaterials* **2004,** 25, 2901-2910.
172. Sohmura, T.; Tamasaki, H.; Ohara, T.; Takahashi, J., Calcium-phosphate surface coating by casting to improve bioactivity of titanium. *J. Biomed. Mater. Res.* **2001,** 58, 478-485.
173. Zyman, Z. Z.; Rokhmistrov, D. V.; Glushko, V. I., Structural and compositional features of amorphous calcium phosphate at the early stage of precipitation. *J. Mater. Sci., Mater. Med.* **2010,** 21, 123-130.
174. Australian Government, A review of the scientific literature on the safety of nanoparticulate titanium dioxide or zinc oxide in sunscreens. In Administration, T. G., Ed. Department of Health and Aging: 2012.
175. Serpone, N.; Salinaro, A.; Emeline, A., Deleterious Effects of Sunscreen Titanium Dioxide Nanoparticles on DNA: Efforts to Limit DNA Damage by Particle Surface Modification. *Proceedings of SPIE* **2001,** 4258, 86-98.
176. King, W. H., Piezoelectric Sorption Detector. *Analytical Chemistry* **1964,** 36, (9), 1735-1739.
177. Cho, N.-J.; Frank, C. W.; Kasemo, B.; Höök, F., Quartz crystal microbalance with dissipation monitoring of supported lipid bilayers on various substrates. *Nature Protocols* **2010,** 5, (6), 1096-1106.
178. Rodahl, M.; Kasemo, B., A simple setup to simultaneously measure the resonant frequency and the absolute dissipation factor of a quartz crystal microbalance. *Rev. Sci. Instrum.* **1996,** 67, (9), 3238-3241.
179. Sackmann, E., Supported membranes: scientific and practical applications. *Science* **1996,** 271, 43-48.
180. Richter, R. P.; Bérat, R.; Brisson, A. R., Formation of Solid-Supported Lipid Bilayers: An Integrated View. *Langmuir* **2006,** 22, 3497-3505.

181. Kunze, A.; Zhao, F.; Marel, A. K.; Svedhem, S.; Kasemo, B., Ion-mediated changes of supported lipid bilayers and their coupling to the substrate: a case of bilayer slip? *Soft Matter* **2011,** 7, 8582-8591.
182. Ridley, M. K.; Hiemstra, T.; van Riemsdijk, W. H.; Machesky, M. L., Inner-sphere complexation of cations at the rutile-water interface: a concise surface structural interpretation with the CD and MUSIC model. *Geochim. Cosmochim. Acta* **2009,** 73, 1841-1856.
183. Berka, M.; Banyai, I., Surface complexation modeling of K^+, NO_3^-, SO_4^{2-}, Ca^{2+}, F^-, Co^{2+}, and Cr^{3+} ion adsorption on silica gel. *Journal of Colloid and Interface Science* **2001,** 233, 131-135.
184. MacDonald, P. M.; Seelig, J., Calcium binding to mixed phospatidylglycerol-phospatidylcholine bilayers as studied by deuterium nuclear magnetic resonance. *Biochemistry* **1987,** 26, 1231-1240.
185. Zubay, G., *Biochemistry*. 3rd ed.; Wm. C. Brown: Dubuque, Iowa, 1993.
186. Long, T. C.; Saleh, N.; Tilton, R. D.; Lowry, G. V.; Veronesi, B., Titanium Dioxide (P25) Produces Reactive Oxygen Species in Immortalized Brain Microglia (BV2): Implications for Nanoparticle Neurotoxicity. *Environmental Science and Technology* **2006,** 40, (14), 4346-4352.
187. Vileno, B.; Lekka, M.; Sienkiewicz, A.; Jeney, S.; Stoessel, G.; Lekki, J.; Forró, L.; Stachura, Z., Stiffness Alterations of Single Cells Induced by UV in the Presence of NanoTiO_2. *Environmental Science and Technology* **2007,** 41, (14), 5149-5153.